DEVELOPMENT AND SIMULATION OF A WIDE-FIELD TOMOGRAPHIC WAVEFRONT SENSOR FOR USE WITH AN EXTENDED SCENE

by

R. Phillip Scott

A Dissertation Submitted to the Faculty of the

COLLEGE OF OPTICAL SCIENCES

In Partial Fulfillment of the Requirements

For the Degree of

DOCTOR OF PHILOSOPHY

In the Graduate College

THE UNIVERSITY OF ARIZONA

2021

THE UNIVERSITY OF ARIZONA
GRADUATE COLLEGE

As members of the Dissertation Committee, we certify that we have read the dissertation prepared by **Randy Phillip Scott**, titled ***Development and Simulation of a Wide-Field Tomographic Wavefront Sensor for Use with an Extended Scene*** and recommend that it be accepted as fulfilling the dissertation requirement for the Degree of Doctor of Philosophy.

Professor Michael Hart Date: 4/13/2021

Professor Daewook Kim Date: 4/13/2021

Professor Jared R. Males Date: 2021-04-13

Final approval and acceptance of this dissertation is contingent upon the candidate's submission of the final copies of the dissertation to the Graduate College.

I hereby certify that I have read this dissertation prepared under my direction and recommend that it be accepted as fulfilling the dissertation requirement.

Professor Michael Hart Date: 4/25/2021
Dissertation Committee Chair
Wyant College of Optical Sciences

STATEMENT BY AUTHOR

This dissertation has been submitted in partial fulfillment of the requirements for an advanced degree at the University of Arizona and is deposited in the University Library to be made available to borrowers under rules of the Library.

Brief quotations from this dissertation are allowable without special permission, provided that an accurate acknowledgement of the source is made. Requests for permission for extended quotation from or reproduction of this manuscript in whole or in part may be granted by the head of the major department or the Dean of the Graduate College when in his or her judgment the proposed use of the material is in the interests of scholarship. In all other instances, however, permission must be obtained from the author.

SIGNED: R. Phillip Scott

ACKNOWLEDGMENTS

This dissertation would not have been possible without the aid of several key individuals who have influenced both my personal and academic life. A special thanks to my parents who have always encouraged me to expand my horizons and pursue greater accomplishments than I could have imagined. Thank you to Professor Todd Lines at Brigham Young University – Idaho who taught me to love the optical sciences with his own passion. Thank you to the many classmates who helped pull me through the challenging curriculum. A special thanks to Kelsey Miller who introduced me to my advisor, provided continued guidance through the path to graduation, and always had the time to be a great friend. Thank you to Justin Knight and Jeff Davis who studied for countless hours to prepare for the comprehensive exam. Thank you, Matt Dubin, for showing me the fun and joy that can be had in system design, development, and testing and for helping me to develop the tools necessary to see projects through. Additional thanks for the advice that you were able to give on the several visits to your office.

I will be forever grateful to my wife, Danielle Scott, for her patience and her motivation to accomplish this great work. While my ambitions of a doctoral degree began before we met, you have been one of the pillars that has allowed me to accomplish this amazing dream. Thank you for supporting me through thick and thin, for doing so while helping me raise three wonderful children, and for being willing to make personal sacrifices to see this fulfilled. You are amazing and I will always be indebted to you for the role you’ve played in getting me to this point.

Additional thanks to Michael Hart, my advisor. Thank you for pushing me and for your open door as I struggled through many problems related to this and other research. Thank you for your patience as I split my attention between my academic, personal, and professional life. Thank you for your mentorship and your kindness.

Thank you to the Space Dynamics Laboratory who have allowed me to work part time while completing this dissertation. It has taken more time and patience than I initially imagined, but I appreciate the many coworkers who have supported and encouraged me through this process.

Table of Contents

LIST OF FIGURES

LIST OF TABLES

ABSTRACT

While initially developed to improve the resolution of astronomical observations, adaptive optics (AO) is a field that is expanding to new applications. Astronomical telescopes continue to push the field in new and interesting ways with concentrated efforts to increase the correction quality and the field of view over which the correction applies. Advances such as Multi-object AO, Multi-conjugate AO, and Ground Layer AO have allowed breakthroughs in the image quality of ground-based telescopes with field of view wider than the isoplanatic patch. As the technology continues to mature, new areas of application continue to be discovered. This work aims to apply common techniques which have been developed for astronomy to applications which image an extended scene through a turbulent medium.

In this dissertation, I have developed the theory and methodology for a new wide-field wavefront sensor focused on measuring and correcting extended scenes. This wavefront sensor utilizes a software-based correction which can be customized to the atmosphere at hand by locating, measuring, and reconstructing a variable number of significant turbulence layers. The methodology is implemented in a simulation to assess the theoretical performance of a benchtop hardware implementation. Quality metrics are investigated and the improvement over correction along a single line of sight is given. This wavefront sensor allows the methodology developed for astronomical applications to be applied to imaging of extended objects and offers a level of flexibility not found in similar adaptive optics systems.

Chapter 1: Introduction

Imaging through a turbulent atmosphere has been a challenge that astronomers have faced for centuries. In the recent past, the field of Adaptive Optics (AO) has emerged to provide solutions which allow for real-time measurement and correction of atmospheric effects. This has enabled a new age of universal exploration as objects which could not previously be resolved from ground-based telescopes are brought into focus. With the development of telescopes several meters in diameter, AO is now the baseline for modern astronomical equipment. AO continues to be developed for several novel applications including high energy laser propagation (Yahel 1990), free-space laser communication (Tyson 2002), and medical imaging (Liang & Williams 1997).

To support the growing diversity of applications, new technology is continually being developed in the form of both hardware and software. The need to measure and correct images taken through a turbulent medium will only increase as instruments emerge with higher demands on image resolution and object range. This chapter will provide a brief introduction to imaging through a turbulent medium and the current environment for wide-field adaptive optics. Section 1.1 introduces atmospheric turbulence and its effects on imagery. Section 1.2 discusses correction methods both classical and modern. Finally, the scope of this work is outlined in Section 1.3 along with a brief summary of the layout for this dissertation.

1.1 Introduction to Atmospheric Turbulence

An initial understanding of atmospheric turbulence helps to gain an appreciation for the complications of imaging through a turbulent medium and gives a better understanding of the resulting solutions. The atmosphere can be imagined as a collection of small pockets of air. Each pocket differs from its neighbors through small temperature variations. These small changes in temperature create differences in the density of air in each pocket. The density of the air pocket is directly related to its refractive index and the change in the refractive index from pocket to pocket is the source of optical aberration in the atmosphere. This aberration changes both spatially and temporally as the pockets move according to the prevailing wind patterns. Each localized region produces differences in the optical path length of adjacent rays which propagate from a given light source. This variation in adjacent rays defines the distortion to the wavefront of light emitted from an object and the resulting aberration is often described as wavefront error (WFE) (Greivenkamp 2004).

To characterize the turbulence strength along a given path through the atmosphere, the refractive index structure coefficient, C_n^2, is defined to measure the level of localized inhomogeneity. This coefficient varies by location, time of day, altitude, and season. Numerical models such as the Hufnagel-Valley (H-V), AMOS, CLEAR 1, and Strategic Laser Communication (SLC)-Day and -Night models have been proposed to estimate a typical profile based on specific criteria. Examples of the H-V 5/7 model and the SLC-Night model are plotted in Figure 1.1. Since the function is so dependent on local conditions, measurements at the observation sight are typically needed to understand the local atmosphere. Since the function gives the turbulence strength distributed through the atmosphere, integration of this function allows computation of the overall turbulence strength along a given line of sight. The most common parameter used to quantify the strength of the turbulence is the Fried parameter, or Fried coherence length defined for a plane wave by the equation

$$r_o = \left(0.423k^2\, sec(\beta) \int_0^L C_n^2(h)dh\right)^{-3/5} \qquad 1.1$$

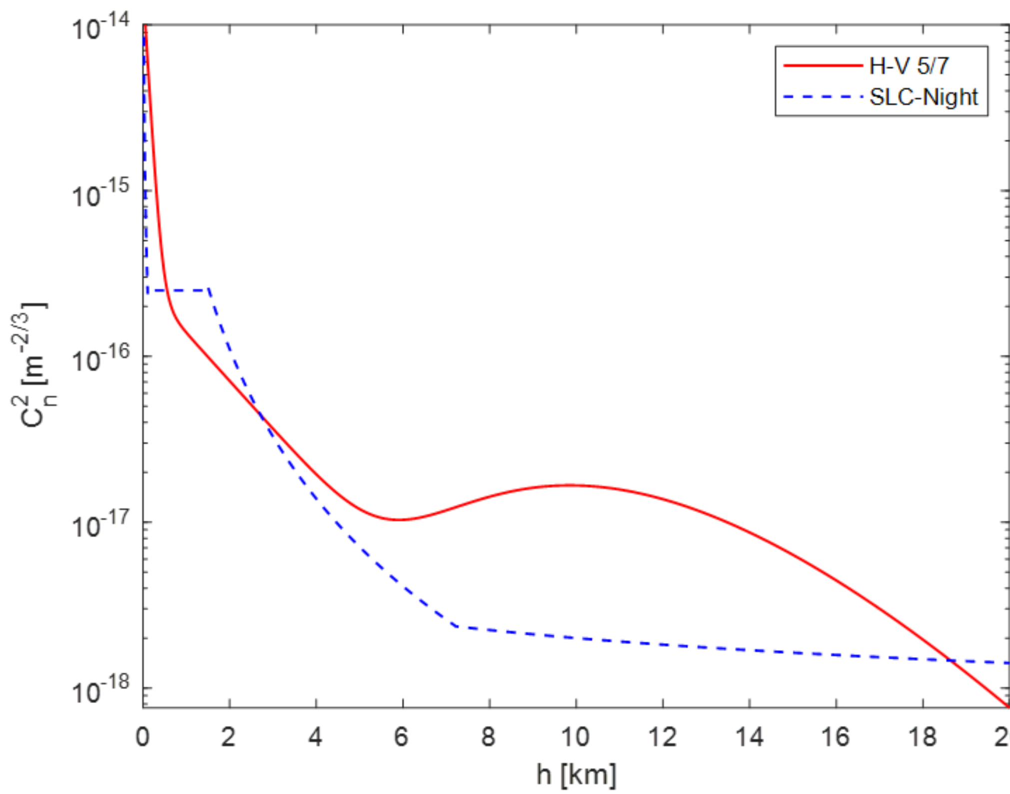

Figure 1.1: Example of two atmospheric profile models.

where r_0 is the Fried length, k is the wavenumber, β is the angle from zenith, and L is the distance to the target (Fried 1965). The Fried parameter characterizes the diameter over which the phase variation is approximately 1 radian (Noll 1976). In applications where the entrance pupil is larger than r_0, the atmosphere will be the limiting factor on image resolution (Fried 1966). This means that imaging systems with an entrance pupil diameter smaller than r_0 will see very little image degradation due to the atmosphere when using short exposures.

The small index variations throughout the atmospheric volume affect the propagation of light over large distances. These perturbations cause degradation in the ability of a given optical system to interpret the observed light. This loss of information occurs because of the induced wavefront variation along different optical paths and degrades both imaging and communication systems. The effects from aberration introduced by the atmosphere can be broken into three categories.

1. Intensity variations which degrade the point spread function (PSF)
2. The image wanders due to variation in the line of sight (LOS)
3. The aberration causes beam spreading due to a loss of coherence

Each of these effects are described in more detail below.

Spatial intensity variation at the detector plane is caused by interference effects as the light traverses different paths through the atmosphere. This effect can be observed in the intensity variation which causes the twinkling of stars. A graphical representation of the PSF from a diffraction limited telescope is shown in Figure 1.2. Phase screens representative of atmospheric turbulence with varying strengths are also generated and applied to the telescope with the corresponding PSFs also shown in Figure 1.2. Three interesting effects shown in this figure are the increase in the number of speckles (proportional to $\left(\frac{D}{r_0}\right)^2$), the increase in area over which the light is spread (approximately $\frac{D}{r_0}$ times larger than the diffraction limited PSF), and the reduction in peak intensity (proportional to $e^{-.134(D/r_0)^{5/3}}$ while a central core remains intact) (Tyson & Frazier 2012). Since the refractive index is defined as the ratio of the speed of light in a vacuum to the speed of light through the medium $\left(n = \frac{c}{v}\right)$ the index variations of the atmosphere cause regions of the wavefront traveling through low refractive indices to travel more quickly while portions of the wavefront traveling through regions of higher refractive index travel more slowly. This warping of the wavefront propagated to the telescope's focus produces interference effects

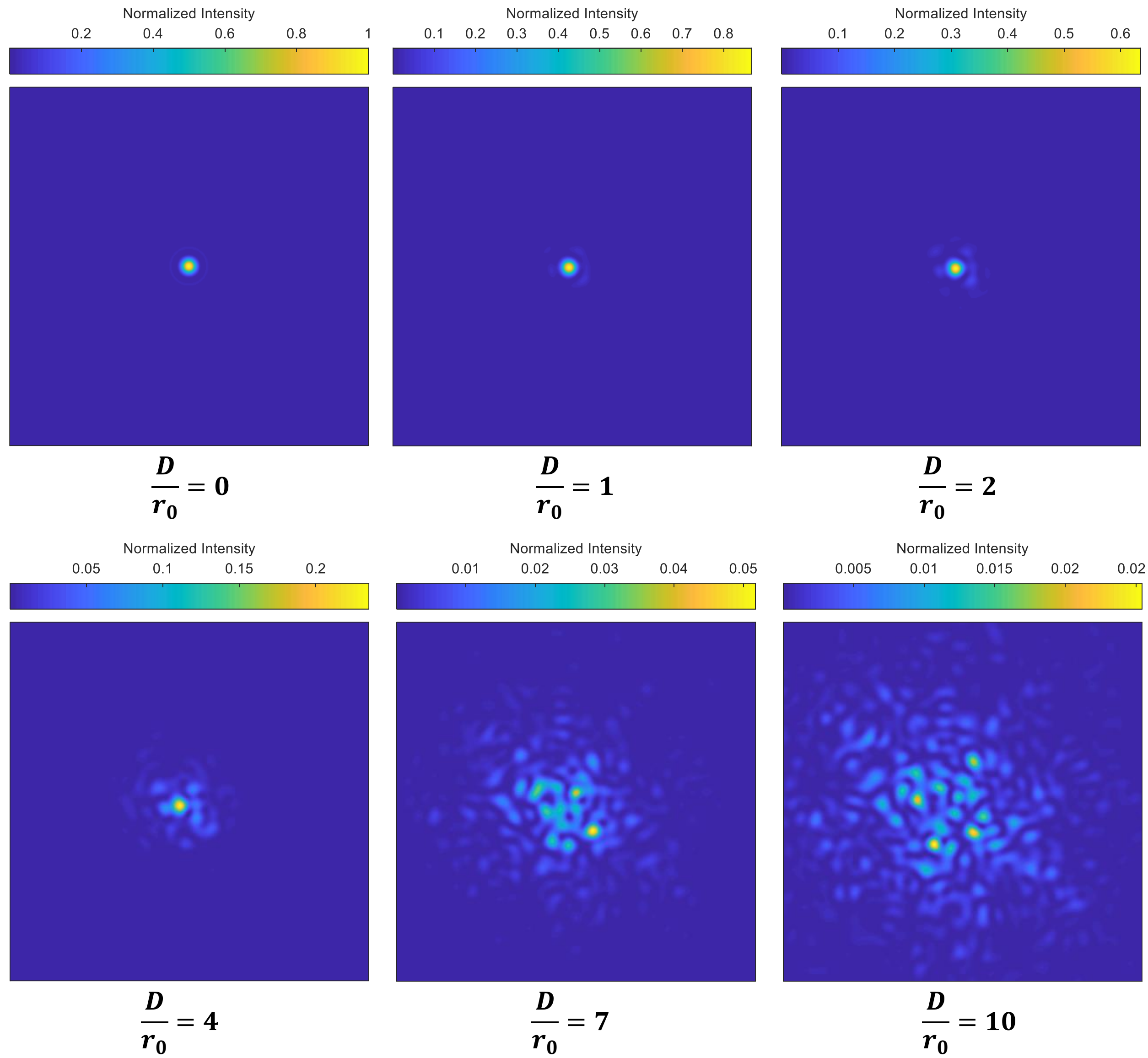

Figure 1.2: PSF from a diffraction limited telescope through turbulence with strength of (a) $\frac{D}{r_0} = 0$ *(b)* $\frac{D}{r_0} = 1$ *(c)* $\frac{D}{r_0} = 2$ *(d)* $\frac{D}{r_0} = 4$ *(e)* $\frac{D}{r_0} = 7$ *(f)* $\frac{D}{r_0} = 10$.

which cause regions of constructive and destructive interference. Correcting this warping of the wavefront is the primary goal of most AO systems as outlined in Section 1.2.

The LOS variation, or beam wander, from turbulence is caused by index variation on spatial scales larger than the beam size. This effectively creates local tips and tilts throughout the atmospheric volume that combine such that the object being imaged appears to move about randomly. If the light collection is slow relative to this changing atmosphere, then the object will appear to blur due to its apparent motion throughout the sensor's integration time. If the light collection occurs quickly, then an evolving PSF will move around the sensor, but not incur additional degradation due to the object's apparent motion. In general, if the exposure time is less than the Greenwood time delay or the atmospheric time constant, then the PSF will evolve through speckle changes and wander around the focal plane. For plane waves, this time constant can be written as

$$\tau_0 = 0.314 \frac{r_0}{\bar{v}} \tag{1.2}$$

where $\bar{v}$ is the spatially averaged wind speed weighted by the layer strengths (Hardy 1998) and τ_0 is the time it takes for the atmosphere to change by 1 radian of mean squared phase error (Fried 1990). This effect is typically corrected through the inclusion of a fast steering mirror (FSM) which responds by rotating in tip and tilt to negate the tilt induced by the atmosphere.

Beam spreading is an effect where parallel paths through the atmosphere have different optical path lengths. This causes a spatially coherent beam to lose coherence due to turbulent eddies smaller than the beam size. Because laser propagation is not within this scope of this work, it is sufficient to note this effect without further discussion.

Even though the atmosphere is a continuous medium that is changing throughout its entire volume, most of the optical aberration can be characterized by treating the atmosphere as a few discrete turbulent layers where all the aberration is present (McKechnie 1991). An example of this simplification using the H-V 5/7 turbulence model as shown in Figure 1.1 would be to assume that there are two significant turbulence layers. One layer would be located near the ground and the second layer would be located roughly 10 km off the ground. Simplifying the atmosphere to these two layers captures the majority of the phase aberration imparted by the atmosphere. The phase disturbance for each layer can be described statistically by a phase structure function of the form

$$D_\phi(\Delta\boldsymbol{r}) = \langle\left(\phi(\boldsymbol{r}+\Delta\boldsymbol{r}) - \phi(\boldsymbol{r})\right)^2\rangle \qquad 1.3$$

where $\phi(\boldsymbol{r})$ is the phase aberration of the layer at some position $\boldsymbol{r}$. The most ubiquitous statistical model for turbulence is generated from observations by Andrey Kolmogorov (1941a, 1941b). For turbulence following Kolmogorov statistics, the structure function for plane wave propagation follows the form

$$D_\phi(\Delta\boldsymbol{r}) = 6.88\left(\frac{\Delta\boldsymbol{r}}{r_0}\right)^{5/3} \qquad 1.4$$

where $\Delta\boldsymbol{r}$ is a radial distance normal to the direction of light propagation and r_0 is the Fried parameter for the given layer. This allows the relation of the structure function to the turbulence strength of the layer and simplifies its description to the single parameter r_0. Using Taylor's frozen flow hypothesis (Taylor 1938), these discrete layers can be treated as a phase variation that is spatially frozen and moved about by the wind present at that layer creating dynamic turbulence. These properties are important for modeling of the atmosphere and for understanding atmospheric correction through techniques such as Ground Layer Adaptive Optics (Section 1.2.2.1), Multi-conjugate Adaptive Optics (Section 1.2.2.3), and the methods proposed throughout this dissertation.

1.2 Atmospheric Characterization and Correction

The aberrations described in Section 1.1 degrade any wavefront propagation through a large volume of dynamic atmosphere. With modern optical measurement techniques and recent advances in computing power, the ability to measure and correct atmospheric effects in real time has become possible. A simple diagram of a system that performs this measurement and correction

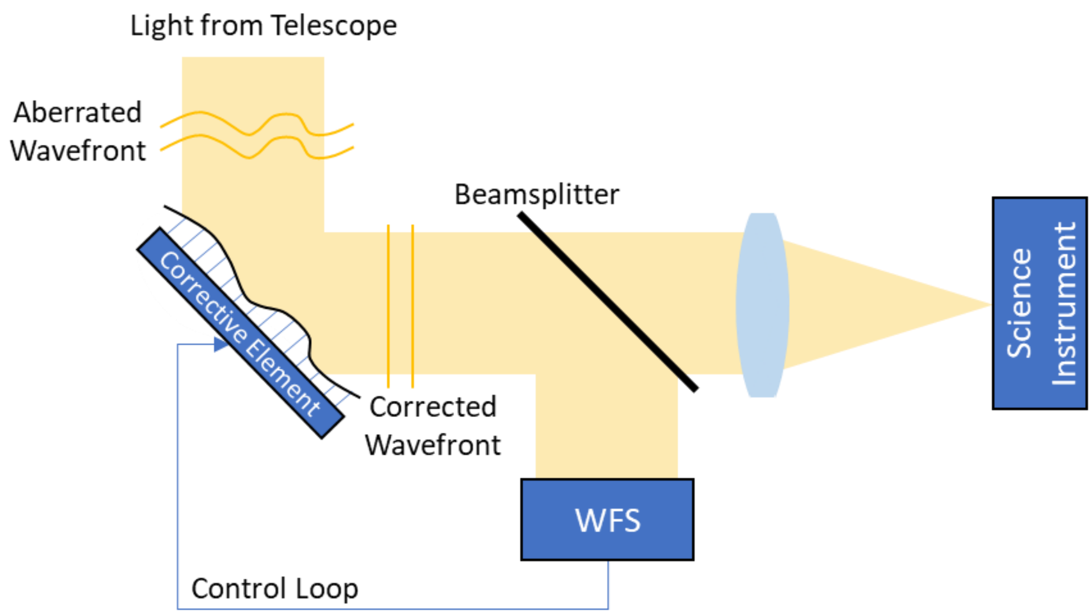

Figure 1.3: Diagram of a system designed for atmospheric correction showing a WFS providing closed-loop control of a deformable mirror to correct the incoming wavefront aberration.

is shown in Figure 1.3. Generally, such a system is comprised of an imaging system to collect the incoming light and a science instrument which captures the data for processing. There is typically a method to sample a portion of the beam for measurement using a wavefront sensor (WFS). The WFS provides real time measurements of the incoming wavefront aberration which are used to determine a correction to be applied via a corrective element. This corrective element can be hardware-based, such as a deformable mirror (DM), or software-based, such as image deconvolution. Where possible, the corrective element is often driven in closed-loop such that the WFS measures residual wavefront error and provides relatively small changes to the corrective element from frame to frame.

1.2.1 Classical Adaptive Optics

With initial applications of adaptive optics focusing on astronomy, systems were developed that allowed correction of a narrow field of view around an object. Standard stars, referred to as natural guide stars, can be used as beacons to determine the effects of the atmosphere. The further away from the guide star the observer looks, the less the correction is valid. The limit to the angle over which the correction applies is termed the isoplanatic angle (θ_0). For turbulence following Kolmogorov statistics, this can be expressed as

$$\theta_0 = 0.314\frac{r_0}{\bar{h}} \qquad 1.5$$

where $\bar{h}$ is the average distance to the turbulent layers weighted by the layer strengths. This is reminiscent of the atmospheric time constant in Equation 1.2 and similarly, θ_0 represents the angle at which the wavefront error has statistically increased by 1 radian and is typically a few arcseconds in diameter (Fried 1982; Welsh & Gardner 1991). Looking along angular separations (θ) greater than θ_0 induces wavefront variance according to the equation

$$\sigma^2(\theta) = \left(\frac{\theta}{\theta_0}\right)^{5/3} \qquad 1.6$$

The limitation in the number of standard stars bright enough for use in a typical AO system along with the correction being limited to the isoplanatic patch means that the region of sky on which corrections can be made is on the order of a few percent. The invention of laser guide stars, first proposed by Foy and Labeyrie (1985), increases the sky coverage significantly, but a natural reference star is still needed to compensate for tip and tilt since the backscattered laser light traverses the same atmosphere through which the outgoing beam propagated (Rigaut & Gendron 1992). These artificial guide stars drastically increase sky coverage as the natural star companion can be much dimmer than when using a natural guide star alone. There is an additional complication to using laser guide stars since the beacon comes from the atmosphere itself. Light from astronomical sources will intersect a cylindrical region of atmosphere while light from the guide star originates at a finite distance and thus intersects a conical volume of the atmosphere. An exaggerated example of this is shown in Figure 1.4. This cone effect means that the guide star does not fully sample the aberration seen by the celestial object but does provide a reasonable

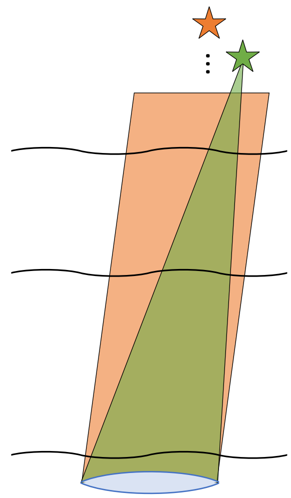

Figure 1.4: Cartoon showing the difference in atmospheric sampling between celestial objects and laser guide stars.

estimate of the total aberration. The limitation of correction only within the isoplanatic patch still limits observations to objects near the guide star and has limited use on large extended objects or scenes.

1.2.2 Wide-field Adaptive Optics

The primary concern of wide-field adaptive optics is to correct regions of the image that are outside of the isoplanatic patch surrounding a single guide star. As seen in Figure 1.5, the more angular separation that exists between two objects, the less atmospheric volume they have in common. As an example, layer A in Figure 1.5 is common between the two objects and the induced aberration in the resulting PSF will be fully correlated. Layer B is only partially correlated since both objects share only a portion of the turbulent layer and aberration induced by layer C is fully uncorrelated due to a lack of overlap between the objects at the turbulent layer. From this description, layer A is isoplanatic since all fields of view will see the same region of this layer. Layers B and C will have some anisoplanatism since the view from the telescope does not fully intersect the same portion of the layer.

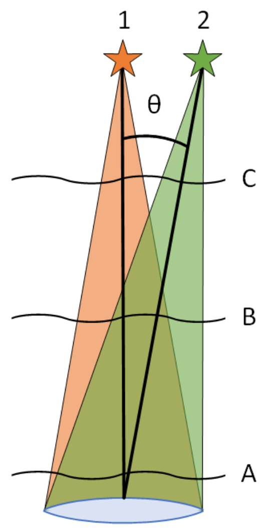

Figure 1.5: Cartoon of a telescope viewing two objects separated by some angle θ. Both objects are viewed through three layers of turbulence at various ranges from the telescope.

Imaging through a turbulent medium over a field of view larger than the isoplanatic patch poses many challenges that cannot be solved using solutions from classical adaptive optics. To overcome these isoplanatic limitations, a variety of techniques have been developed and successfully demonstrated to correct larger portions of the image in astronomical telescopes which have a wide field of view. A brief overview of the most common techniques is given below.

1.2.2.1 Ground Layer Adaptive Optics

Ground Layer Adaptive Optics (GLAO) is the process of removing aberration common to all lines of sight (Rigaut et.al. 2002). This method typically utilizes multiple guide stars across the field of view each measured using a corresponding wavefront sensor, although a single low altitude Rayleigh laser guide star can be used as well (Tokovinin 2004). The average aberration between all lines of sight is corrected with a mirror at or near the telescope pupil. Referencing Figure 1.5, this is equivalent to removing the effects of Layer A across the entire field of view. Studies for the Gemini telescope on Mauna Kea have shown that the ground layer turbulence is localized to within the first 30 meters and that the strength of the ground layer turbulence is roughly equivalent to the strength found in the remainder of the atmosphere (Chun et al. 2008). The same study showed that a telescope utilizing GLAO could provide correction for fields of view out to 1 degree or more. GLAO also allows nearly complete sky coverage and can be used with other methods of adaptive optics to improve the number of nights on which adaptive systems can be utilized (Anderson 2006).

A key limitation of GLAO is that this technique focuses on correction of a single layer rather than correction along a single line of sight. Because of this, all anisoplanatic aberration remains and there is no line of sight where diffraction limited imaging is expected. Instead of pristine correction around a single object, GLAO achieves a modest correction across the entire field of view. This is particularly well suited to locations with strong layers of isoplanatic turbulence and relatively weak turbulence remaining in the free atmosphere.

1.2.2.2 Multi-Object Adaptive Optics

Multi-Object Adaptive Optics (MOAO) follows a similar design to that of GLAO in that multiple guide stars are used across the telescope field of view with each line of sight being characterized by a separate WFS (Hammer 2002). By measuring the off-axis wavefront of several sources, the on-axis wavefront can be estimated through atmospheric tomography (Assemat et. al. 2004; Ragazzoni et. al. 1999). The atmospheric estimate is corrected using a DM conjugate to the telescope pupil. One alternate method is to independently correct multiple lines of sight around the object of interest and thereby apply some level of correction to regions much larger than the isoplanatic patch. This second method requires the addition of several deformable mirrors to the MOAO system increasing the cost, complexity, and size of such a system (Becker 1988). The tomographic method allows correction of any desired object within a field of view of 5-10 arcminutes (Hammer 2002). This is a narrower field of view than GLAO, but MOAO offers higher fidelity correction of the object of interest. The inclusion of multiple wavefront sensors, each of which images a guide star in the scene, also adds significant cost and complexity to MOAO systems compared to classical AO or GLAO.

One weakness of MOAO is that the correction is typically applied for a single line of sight and so is only valid over a single isoplanatic patch. The benefit is that the object can be located anywhere in the FOV and can be adjusted as desired. Applications with multiple DMs can correct over the entire field, but the correction degrades away from each of the guide stars. MOAO also requires multiple guide stars near the object of interest with a preference for natural guide stars (Assemat et. al. 2004). Systems with a combination of natural and laser guide stars have also been developed to reduce the number of required natural guide stars and to increase sky coverage (Andersen et. al. 2012). MOAO has been proven in the lab and implemented for astronomical corrections, but relatively few MOAO systems exist on large telescopes.

1.2.2.3 Multi-Conjugate Adaptive Optics

Multi-Conjugate Adaptive Optics (MCAO) also utilizes multiple wavefront sensors and deformable mirrors, but instead of correcting along several lines of sight, the system aims to correct specific layers of the atmosphere (Dicke 1975; Fried 1977; Beckers 1988). The atmospheric profile can be measured using Slope Detection and Ranging (SLODAR), Scintillation Detection and Ranging (SCIDAR), Multi-aperture Scintillation Sensor (MASS), and balloon-based measurements among other techniques (Wilson 2002; Vernon and Roddier 1973; Kornilov 2003). Of particular interest to this work is the SLODAR technique which utilizes overlapping lines of sight between a lenslet array and multiple objects to determine ranges to key layers of turbulence. The SLODAR method is expounded on in detail in Section 2.3.1. Characterization of the profile at the observation sight is critical to understand the location of the strongest turbulence layers and how the profile changes over time. Once the turbulence profile is well characterized and strong layers of turbulence are identified, then a wavefront sensor and deformable mirror are placed conjugate to the identified layers. This allows measurement and correction of the phase disturbance local to set ranges and improves seeing across a field of view an arcminute or two in diameter (Rigaut 2000).

While MCAO provides the best correction over the entire FOV, it has several limitations that prevent it from working across fields of view as large as either GLAO or MOAO. One such limitation of MCAO is that it requires prior knowledge of the atmosphere and well-conjugated deformable mirrors and wavefront sensors to successfully correct across the image. Conjugation errors do provide graceful degradation rather than an ultimate failure of the system (Rigaut 2000), but layers of strong turbulence can change with local weather patterns and the cycling of the seasons. Another limitation is the number of deformable mirrors that is required as the field of view increases. Three mirrors make the correction over one arcminute possible (Rigaut 2000), but a wider field of view would require more guide stars, more wavefront sensors, and more DMs.

1.3 Scope of Work

To further the breadth of applications for adaptive optics, I propose a novel Wide-field Imaging Shack-Hartmann (WISH) wavefront sensor that utilizes information from a diverse scene to estimate and numerically correct for the volume of atmosphere viewed through the telescope. A simplified layout of the WFS is given in Figure 1.6. This WFS uses a standard Shack-Hartmann lenslet array to produce many images of the scene which can be compared against a reference image to determine local warping. With the warping information, a modified SLODAR technique is employed to measure the atmospheric profile. This implementation allows atmospheric characterization to occur in real-time as the science data is collected. The use of an extended scene allows for a more object-rich dataset than relying on natural or artificial guide stars. Potential

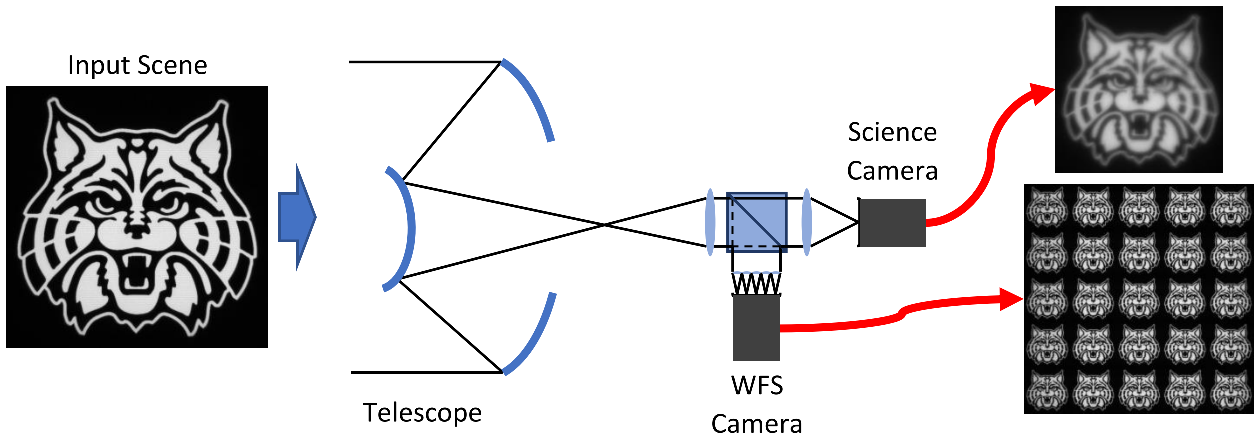

Figure 1.6: Simplified diagram of the WFS along with an example of an input scene and output images from the science and WFS cameras.

applications of this instrument could include planetary imaging, solar imaging, imaging of low Earth orbit satellites, and ground-to-ground or air-to-ground imaging. This method can also be applied to regions of the sky with dense star coverage which makes it analogous to an MOAO system that can also provide atmospheric profiling capabilities.

Because the correction is applied numerically, the wavefront sensor can adjust for a varying number of layers and their dynamic ranges to provide a dynamic reconstruction and correction of the atmosphere. The fully numerical correction allows flexibility in the wavefront sensor for dynamic seeing conditions and for motion of the AO system to regions with different atmospheric characteristics. The addition of a single DM can also enable incorporation of a hardware based GLAO or MOAO implementation to increase the fidelity of the software correction. While this wavefront sensor incorporates aspects of MCAO and MOAO systems, it is the flexibility to atmospheric conditions combined with the low size, weight, power, and cost (SWaP-C) that creates a truly novel device. Performance of the WFS is predicted using simulations of multiple static atmospheres to determine the feasibility of atmospheric measurement and reconstruction.

This work will present the theory and methodology of this new wavefront sensor along with a description of the numerical simulation culminating in a proof of concept. Chapter 2: of this work focuses on the theory and methodology behind the wavefront sensor. While the simulation and proof of concept are limited to a static atmosphere, an overview of operation in a dynamic atmosphere is also included. The description of the simulation efforts and relevant parameters are given in Chapter 3:. Chapter 4: provides a discussion of the simulation results and Chapter 5: summarizes future work related to the wavefront sensor development.

Chapter 2: Theory and Methodology

As described in Section 1.2, AO systems are generally characterized as having an imaging system, a wavefront sensor, and a corrective element. For this application, the imaging system starts with a telescope which relays science light to a beamsplitter as seen in the cartoon layout presented in Figure 2.1. The beamsplitter allows the light from the scene to be imaged simultaneously onto the wavefront sensor and onto the science camera. The wavefront sensor allows computation of the significant turbulence layers along with estimates of their range, wind velocity, and relative strength. The proposed correction in this system isn't accomplished via hardware such as a DM but is instead accomplished numerically via deconvolution of computed field-dependent PSFs. Performing the wavefront sensor measurement, atmospheric characterization, layer reconstruction, and image correction is software intensive, but offers a way to apply correction in a small, efficient package.

The flow diagram shown in Figure 2.2 shows how data is collected and processed by the WFS. This diagram has been broken into three parts:

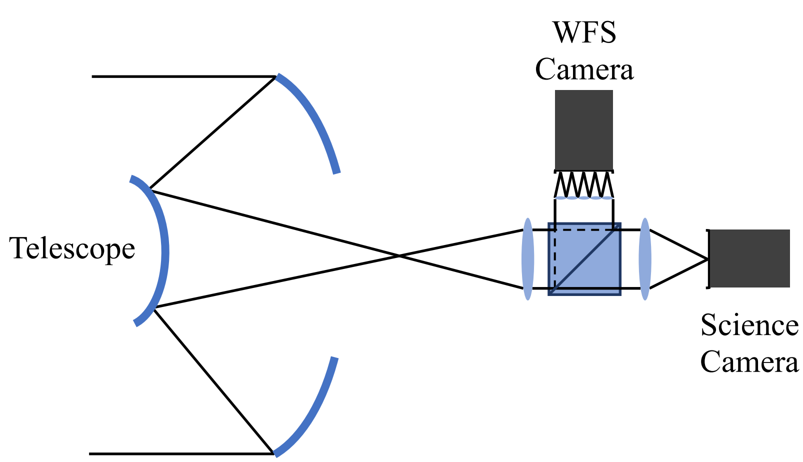

Figure 2.1: Cartoon layout of the system hardware including a telescope and the wavefront sensor.

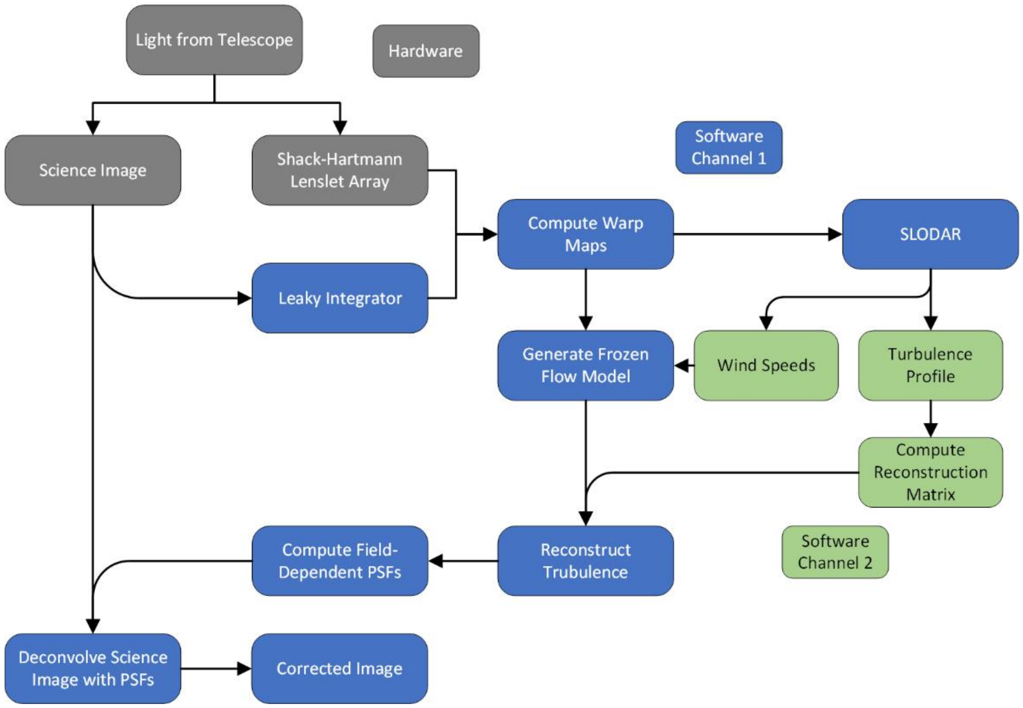

Figure 2.2: Block diagram showing the flow of data and the analyses performed. Gray blocks represent the system hardware while blue and green blocks represent software functionality. The blue set of functions act in real time while the green set represent time averaged turbulence properties.

1. System hardware: The hardware needs to be suited for the given application. The telescope will determine the FOV and image resolution. The cameras will determine image fidelity and the framerate of the WFS. The lenslet array determines the sampling of the atmosphere and the ranges of turbulent layers which can be detected and reconstructed.

2. Software channel 1: The first software channel responds in real-time to each image that is read out of the WFS. Each image taken by the WFS will see a different atmosphere which is analyzed and reconstructed through correlations between the WFS sub-images. Allowing this channel to operate independent of software channel 2 enables high speed correction to take place while channel 2 averages over multiple frames for a robust characterization of the atmosphere.

3. Software channel 2: The second software channel computes local atmospheric conditions based on time averaged data from the WFS. This channel uses the past several frames of

data to determine atmospheric conditions in real time including the distance to each significant layer along with its relative strength and wind velocity. The information from channel 2 will be used periodically to update the atmospheric reconstruction that takes place in channel 1. This allows the reconstruction to compensate for dynamic atmospheric conditions including changes in layer properties and even changes in the number of layers reconstructed.

The flow diagram provides a graphical overview of how the WFS operates. The telescope defines key system parameters and relays light from the scene along the two imaging arms as described in Section 2.1. The data from both arms is manipulated and combined to produce warp maps as described in Section 2.2. Section 2.3 describes how atmospheric parameters are determined from these warp maps. These details are used to update the reconstruction matrix which in turn provides estimates of the phase disturbances of each layer per Section 2.4. This allows computation and deconvolution of the field-dependent PSFs resulting in a corrected final image described in Section 2.5.

2.1 Hardware Considerations

The proposed system hardware is minimally composed of a light-gathering telescope, relay optics, a beam splitter, a lenslet array conjugate to the pupil, an imaging lens, and two cameras placed in the focal planes of the two system arms as shown in Figure 2.1. Computing hardware is also necessary for storing and analyzing the recorded images. Inside the WFS, the light from the scene is imaged onto the two detectors using the beamsplitter. One channel directly images the scene onto a detector and records the science image. This is the image that will eventually be corrected using the field-dependent PSFs generated by the tomography algorithm. The exposure time for this detector is set by atmospheric conditions. In general, the exposure time needs to be less than the atmospheric time constant, τ_0, as discussed in Section 1.1. τ_0 can be estimated if atmospheric conditions are known by using Equation 1.2. This requires knowledge of the range, wind speed, and strength of each significant turbulence layer. Since the proposed WFS reconstructs key layers after measuring the wind speed and the turbulence profile of the atmosphere, τ_0 may be continually monitored and used as a check on the framerate of the system.

The second channel of light from the beam splitter is imaged through the lenslet array onto a second detector. This lenslet array is placed conjugate to the telescope pupil so that the highly turbulent atmosphere near the pupil can be easily measured using relative image displacements. The scene is imaged through each lenslet along a different line of sight through the atmosphere which induces warping unique to that sub-image. These small differences in lines of sight are what enables the tomography of the WFS and thus the reconstruction of the atmosphere. The framerate of the WFS camera is matched to that of the science camera.

The details of the hardware design need to be adjusted for a given application, but there are two key parameters to consider when doing so. The parameters of greatest interest to this method of wavefront sensing are the number of isoplanatic patches across the field of view $\left({FOV}/{\theta_0}\right)$ and the number of lenslets across the telescope pupil $\left({D}/{w}\right)$. Here θ_0 is the isoplanatic angle as described in Section 1.2.1, D is the telescope pupil diameter, and w is the width of the lenslets in the pupil. Both of these parameters will be driven by the seeing conditions for the given application, but the advantage that the Wide-field Imaging Shack Hartmann (WISH) WFS has is that the correction can be adjusted to accommodate dynamic changes in an atmospheric profile.

While a wider field of view is often desirable in imaging systems, there are some important limitations to consider related to the parameter ${FOV}/{\theta_0}$. To compute the warp maps, each scene is broken up into patches sized on the order of θ_0. For the proof-of-concept simulations, values of $FOV/_{\theta_0} = 10 - 15$ were used with each image of the scene split into a 15×15 grid of patches. If $FOV/\theta_0 \approx 1$ or less, then the benefits of wide-field AO are negligible, and correction can be performed using classical AO. Conversely a large value for this parameter means that each patch has fewer pixels for the use in comparisons between sub-images and the atmospheric reconstruction and correction will suffer due to the reduced spatial frequency content within each isoplanatic patch. Additionally, larger values for this parameter will increase computation time as the number of cross-correlations rapidly grows. In spite of these problems, one of the benefits of a high $FOV/_{\theta_0}$ is the increase the number of baseline pairs in object space which will allow for a greater sampling of the atmosphere as described in Sections 2.2.2 and 2.3.1. The final consideration is the limitation imposed by using a layer-dependent reconstruction and correction similar to MCAO. For a continuous atmosphere, $\frac{1}{2}(FOV/\theta_0)$ layers need to be corrected to ensure successful correction over the entire FOV (Beckers 1988). In general, the system needs to be designed with a FOV that strikes a balance between allowing good atmospheric sampling, reasonable computation times, and a high enough spatial variation across a patch for low error in the cross-correlations between sub-images.

The parameter $D/_{W}$ is similarly important and affects image formation and atmospheric sampling. This parameter describes the number of lenslets across the pupil which can cause challenges in the extremes of either dense or sparse sampling. The number of lenslets determines the number and quality of sub-images which are formed. The primary considerations when determining the appropriate number of lenslets across the telescope pupil are:

1. Image resolution: The $f/\#$ of the lenslets must be small enough that the cutoff frequency, $f_c = \frac{1}{\lambda(f/\#)}$, for each sub-image contains scales meaningful to the scene and the application.

2. Radiometric transfer: The amount of light per lenslet must be enough to maintain a short exposure time on the order of τ_0 while maintaining a high SNR for imaging.

3. Atmospheric sampling: While the Slope Detection and Ranging (SLODAR) technique that this WFS utilizes typically requires twenty or more lenslets across the pupil for a pair of stars (Wilson 2002), the increase in baseline pairs due to the number of isoplanatic patches across the FOV allows this parameter to be significantly reduced.

Each of these items are important for atmospheric measurement and reconstruction and must be taken into account during the system design for the application at hand.

2.2 Image Analysis

The first task of the WISH wavefront sensor is the image processing that takes place. The WFS captures the science image through the science camera and several sub-images through the lenslet array. An example of the output datasets for a 5×5 lenslet array in a benchtop environment are shown in Figure 2.3. The sub-images are compared against a reference image to determine warping of features on the scale of the isoplanatic patch. Since each sub-image is captured along a different line of sight, these comparisons allow tomographic information about the atmospheric aberration to be retrieved. Generating these warp maps is critical for WFS operation as these are the primary data product used by the other analysis tools. A leaky integration of the science image provides a reliable reference. Breaking this reference and the sub-images into patches of the scene on the order of the isoplanatic patch allows the use of cross-correlations to determine the localized

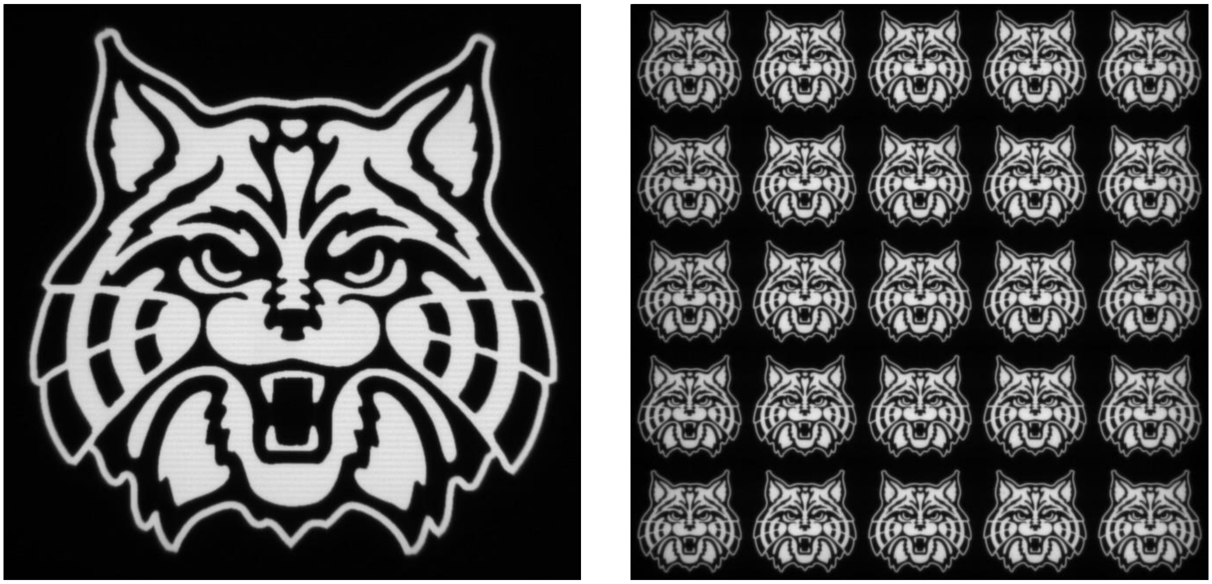

Figure 2.3: Benchtop example of data captured through the WISH WFS with no turbulence present. The science image (left) is a high-resolution reproduction of the image. The sub-images (right) are formed through a 5×5 lenslet array forming 25 sub-images to analyze for atmospheric disturbances. Both datasets are captured simultaneously using 1500×1500 pixel CMOS detectors

warping in each sub-image. Similar methods of sub-image comparison have been demonstrated for MCAO systems built for solar observations (Berkefeld et. al. 2003; Kellerer 2012).

2.2.1 The Leaky Integrator

Determination of local warping in a given sub-image requires a reference image against which it can be compared. Ideally this would be a pristine image of the scene, but for most applications such an image is not available. One option could be to use the corresponding frame of the science image as this reference, but each frame from the science camera sees turbulence across several isoplanatic patches which causes anisoplanatic warping to occur. This is manifest as localized image distortions as shown in the simulated image presented in Figure 2.4. Because the atmospheric refractive index fluctuations can be treated as a zero-mean process (Noll 1976), the true geometry of the scene can be recovered by averaging several tilt-corrected frames of the science image. Averaging the warping of individual frames causes some degradation to high spatial frequencies, but the resulting image retains much of the spatial frequency on scales smaller

Figure 2.4: Example of local distortions due to imaging through anisoplanatic turbulence. This is most evident in the light pole on the right side of the picture as well as in the curb lines in the central and upper right portions of the image. Image courtesy of Michael Hart.

than $\frac{\lambda}{r_0}$ (Tyson & Frazier 2012) and can be used as a reference to determine local warping in each of the sub-images.

To keep the reference image current with the changing atmosphere, a leaky integration variant which weighs the most recent image most heavily is imposed. Past frames are added to the scene with diminishing returns until frames older than some pre-determined integration time are ignored. If the framerate of the camera is n frames per second and the integration time is t, then the total number of frames in the leaky integration is defined as $N = n \cdot t$. The leaky integration is thus performed according to the equation

$$F_{ref} = \sum_{i=0}^{N-1} F_i \left(\frac{N-i}{N}\right) \qquad 2.1$$

where F_r is the reference image, F_i is the ith frame with $i = 0$ being the current frame, and $i = N$ the oldest included frame. While this is the general form of the integrator, additional weighting factors for each frame can be included as the application requires.

Local conditions and application details will determine the ideal integration time scale, t. Atmospheric parameters will dictate the shortest recommended timescales while relative motion between the telescope platform and any object of interest determine the longest. The minimum integration will ideally occur over several atmospheric time constants, τ_0. For timescales longer than τ_0, the temporal correlation of the atmospheric aberration is poor. Because of this poor correlation, extending the leaky integration time much longer than τ_0 allows the anisoplantic warping to average out. Conversely, to determine the maximum timescale for integration the relative motion of objects in the scene needs to be small enough to not cause significant blurring. The relative angular motion between the viewing platform and the object of interest in one frame time is $\frac{\Delta x}{d}$ where Δx is the lateral distance the platform and the object have moved with respect to one another and d is the distance between the platform and the object. Ideally, these objects have moved less than the full width at half of the maximum (FWHM) of the point spread function. In angle space, this is approximately $\frac{\lambda}{D}$ where λ is the wavelength and D is the diameter of the telescope's entrance pupil. Comparing these two quantities, the derived inequality is $\frac{\Delta x}{d} < \frac{\lambda}{D}$. Substituting $\Delta x = v\Delta t$, the inequality becomes

$$\Delta t < \frac{d \cdot \lambda}{v \cdot D} \qquad 2.2$$

where Δt is the maximum integration time. This too can vary by application, but the above equation offers a good rule of thumb.

2.2.2 Computing Warp Maps

With the leaky integration providing a continually updated reference image, local warping in each of the sub-images can be computed. The first step in comparing a given sub-image to the reference is the removal of overall tilt. This allows the objects in the scene to be in the same region of the science image and each sub-image. The overall tilt of each sub-image contains information about the isoplanatic aberration content, and this slope information should be combined with the local warping to determine the overall atmospheric aberration. With the science and sub-images aligned to one another, each image is broken into patches roughly the angular size of the isoplanatic patch, θ_0, yielding $\left(\frac{FOV}{\theta_0}\right)^2$ number of object related patches in the scene (also referred to in this text simply as objects or patches). An example of a reference image being broken into patches is shown in Figure 2.5.

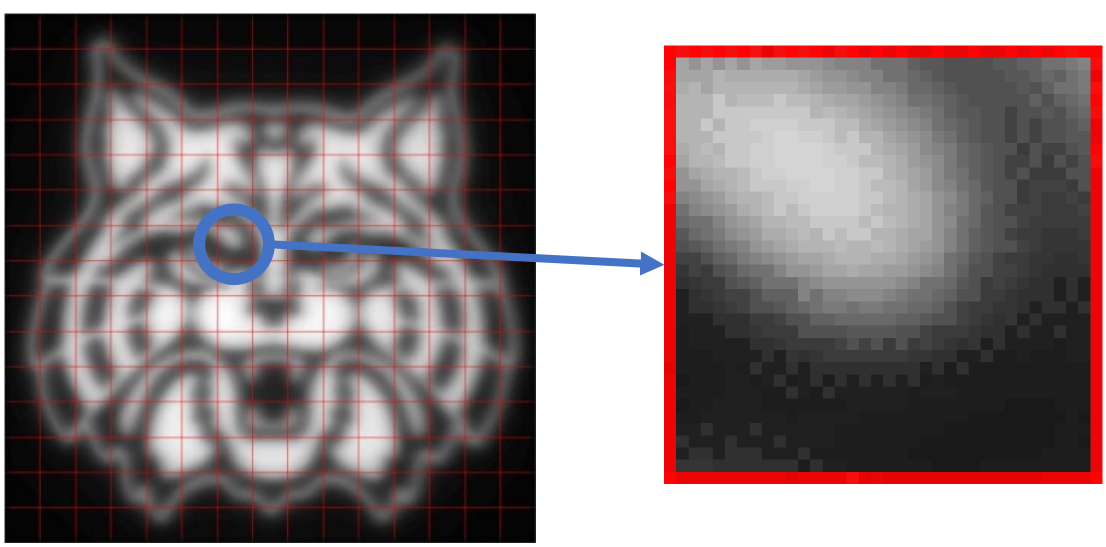

Figure 2.5: Example of a leaky integrated reference image being broken up into a 15×15 grid (left). One of the patches used for cross-correlation with the sub-images is also shown (right). Red gridlines are shown for demonstrative purposes only.

The chosen patch size is θ_0 because the PSF experiences little change over this angular extent, but this comes with the challenge that θ_0 changes with varying atmospheric conditions. To overcome this challenge, the WFS operation can begin with a conservative estimate of θ_0 for warp map generation. The WFS can then characterize the turbulence profile as described in Section 2.3 to determine the ranges and strength of significant layers. Because the WFS continually monitors the turbulence profile, it is possible to monitor θ_0 throughout operation and update patch sizes appropriately on-the-fly. This method of operation requires a brief time period for the system to "warm up" and begin producing results tuned to the local atmospheric parameters.

With both the science and sub-images broken into nearly identical patches, the patches from each sub-image can be compared to the corresponding science image patches to determine local warping. This comparison helps determine the induced atmospheric tilt along the line of sight from the given portion of the scene to the sub-image being analyzed. This comparison is most efficiently performed using a cross-correlation. Because there is a flux difference between the leaky integrated reference image and the sub-aperture images, these images should be normalized prior to performing such a cross-correlation. One normalization method that shows promising results is to force each image to have a common dynamic range and make the mean value of each image zero. This forces the images to be equally weighted and emphasizes the matching of both light and dark regions of the images. The location of the peak of the cross-correlation shows how far the patches have shifted relative to one another and yields the gradient of the wavefront aberration seen through that specific line of sight. This shift information is analogous to the measurements made through a Shack-Hartmann WFS for a single guide star.

Repeating the cross-correlation for each patch in a sub-image yields a warp map related to the corresponding lenslet. Once the warp maps are computed for each lenslet, we achieve an

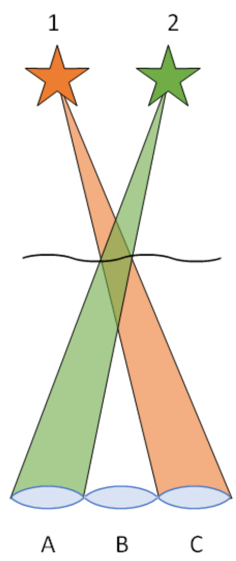

Figure 2.6: Example of two lenslets seeing the same aberration content from a given layer along different lines of sight.

object-rich scene passively illuminated with the object points forming a grid. While each lenslet has a unique line of sight to a given object in the scene, Figure 2.6 shows how turbulence information from a distant layer can be imprinted onto warp maps from multiple lenslets. In this case lenslet C sees aberration from the turbulent layer while viewing object 1. Lenslet A sees the exact same aberration content from this layer while viewing object 2. Both lenslets see the aberration induced from this small patch of turbulence, but it is while viewing different portions of the scene. This concept forms the basis of SLODAR which is discussed in detail in Section 2.3.1.

Examples of simulated warp maps for a 5×5 lenslet array viewing a 15×15 grid of objects are shown in Figure 2.7, Figure 2.8, and Figure 2.9. Figure 2.7 shows a warp map where turbulence is located near the entrance pupil which results in isoplanatic aberration. Isoplanatism appears in the warp map as a constant slope across each lenslet, or in other words, an overall shift for each sub-image. Figure 2.8 shows the resulting warp map from turbulence located far from the telescope entrance pupil. This results in anisoplanatic aberration, or aberration that changes based on the line of sight. Similarities between warp maps from adjacent lenslets can be seen showing the common aberration between different lines of sight as was shown in Figure 2.6. When multiple layers of turbulence are present, the isoplanatic and anisoplanatic effects are combined resulting in the warp map shown in Figure 2.9. This figure uses the same turbulence layers used to generate Figure 2.7 and Figure 2.8, but the line-of-sight effects that are easily observed with either layer individually are more obscure when combined.

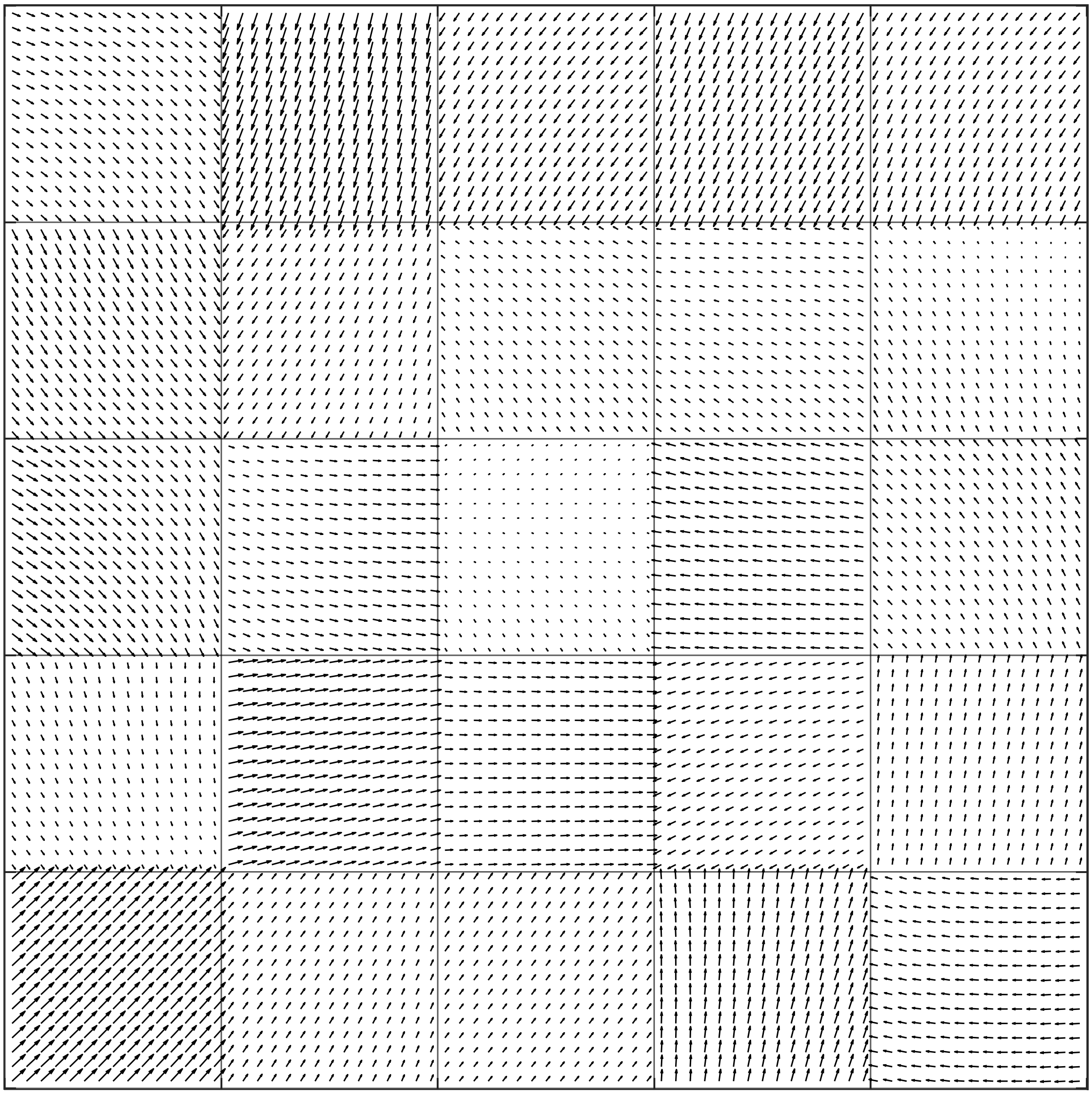

Figure 2.7: Warp map demonstrating primarily isoplanatic aberration. This warp map is generated for a 5 × 5 lenslet array with 15 object points across the scene and aberration located near the telescope entrance pupil. Each sub-image is dominated by tip/tilt resulting in warp maps with a single direction for each lenslet.

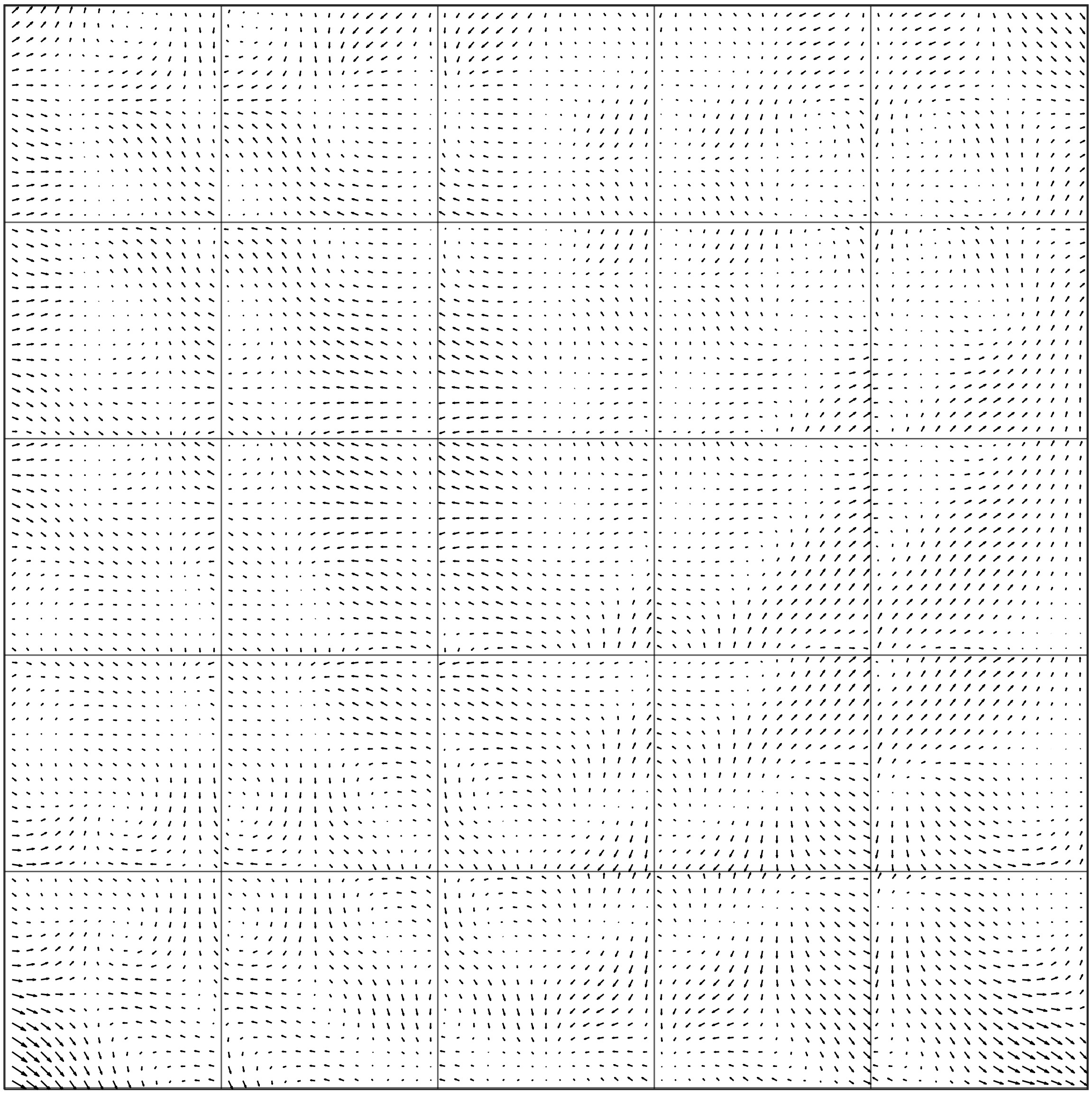

Figure 2.8: Warp map demonstrating anisoplanatic aberration. This warp map is generated for a 5 × 5 lenslet array with 15 object points across the scene and aberration located far from the telescope entrance pupil. Specifically of interest are the warp map features which are shared between warp maps from adjacent lenslets. These features are displaced between the adjacent warp maps by roughly 1/3 of a lenslet width.

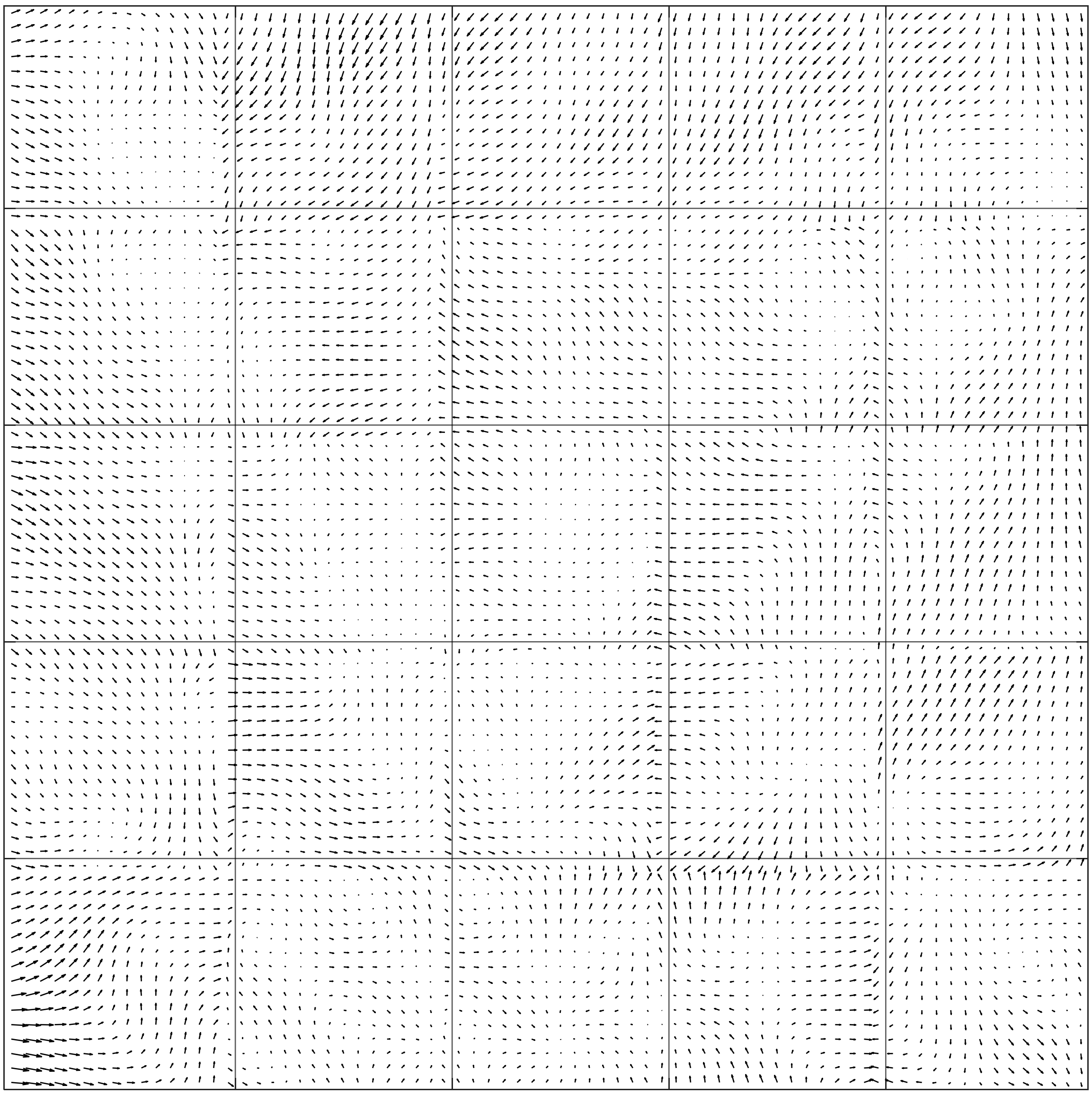

Figure 2.9: This warp map combines the warp maps from Figure 2.7 and Figure 2.8 to show a combination of isoplanatic and anisoplanatic warping. This warp map is generated for a 5 × 5 lenslet array with 15 object points across the scene. This warp map contains aberration from two turbulent layers with one located near the telescope entrance pupil and the other far from it.

2.3 Atmospheric Analysis

One of the key aspects of the WISH WFS is the ability to measure and respond to changes in the makeup of the turbulence profile. The warp maps are key to this analysis as it describes the average tilt seen along each of the WFS's lines of sight. Each warp map is analyzed by the SLODAR algorithm which outputs an estimate of the turbulence profile. Additional detail regarding the atmospheric composition can be obtained using a temporal correlation of successive warp maps. With this temporal correlation comes an estimate of layer velocities which are used in conjunction with frozen flow modeling to improve range estimates and the resolution of atmospheric reconstruction. Peaks in each of these correlation profiles correspond to ranges where significant aberration occurred. Each profile is analyzed using a variation on the CLEAN algorithm developed for radio astronomy to iteratively find the most significant layers. All of this information is used to understand the atmospheric profile so that an appropriate reconstruction matrix can be generated for the current atmospheric conditions.

2.3.1 Slope Detection and Ranging (SLODAR)

SLODAR is a technique that was originally developed for use with binary stars seen through a Shack-Hartmann WFS (Wilson 2002) and has been expanded on for use with multiple stars taking measurements between each baseline pair (Wang et. al. 2008). The SLODAR theory is expanded further in this work for observation of an evenly spaced grid of objects. Figure 2.10 shows how different lenslets see each object through a different line of sight and how some of these lines of sight will have regions of overlap. Figure 2.11 further lays out the basic geometry associated with SLODAR and showcases the relationship of relevant quantities.

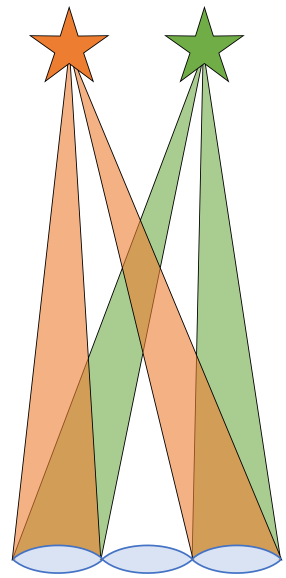

Figure 2.10: Cartoon showing how objects are seen along different lines of sight through different lenslets. An overlap region between these lines of sight is also observed as was shown in Figure 2.6.

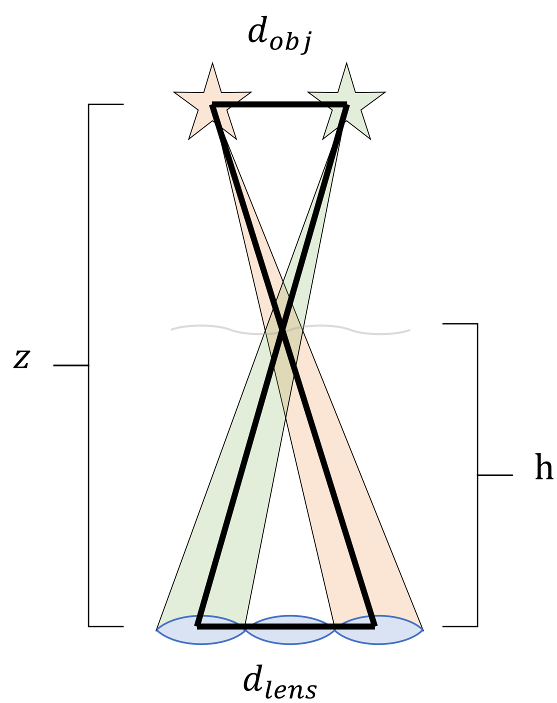

Figure 2.11: WFS cartoon showing the relationship between objects, lenslets, and the range of a common volume of atmosphere.

2.3.1.1 Layer Ranging

Looking at a pair of objects separated by some distance z from the telescope through a lenslet array, one can see a pair of similar triangles that intersect at some range h. Comparison of the triangles as shown in Figure 2.11 gives the following relationships

$$\frac{d_{obj}}{z-h} = \frac{d_{lens}}{h} \tag{2.3}$$

$$h = \frac{z * d_{lens}}{d_{obj} - d_{lens}} \tag{2.4}$$

where d_{obj} is the projected object separation and d_{lens} is the physical separations of the two lenslets. For two objects with a small angular separation, one can define the separation as $\theta = \frac{d_{obj}}{z}$. Since the WFS typically uses relatively small lenslets to image objects with relatively large spacings, the assumption that $d_{obj} \gg d_{lens}$ is almost always true. Combining these two assumptions, Equation 2.4 simplifies to give the relationship

$$h = \frac{z * d_{lens}}{d_{obj}} = \frac{d_{lens}}{\theta} \tag{2.5}$$

This relationship allows one to determine the distance to a volume of atmosphere common to two different lines of sight. This relationship is what allows the turbulence profiling to take place by knowing the angular separation between each patch in the scene and the lenslet through which it is viewed.

With the range of the crossover region defined, the warp map is used to compare tip and tilt of the atmosphere between all patches of the scene viewed through all lenslets. The warp map gives the overall tilt of a patch relative to the leaky integration of the science image, but the data processing considers the x and y components of the slopes independently. To outline the SLODAR process we will consider only the x-slope for some given patch (n, m) compared with a second patch $(n + \delta n, m + \delta m)$. To retrieve information about a given region of atmosphere, there also needs to be a lenslet separation present and so we compare the slope from the first patch in some sub-image (i, j) to the second patch in a different sub-image $(i + \delta i, j + \delta j)$. These two slopes are noted as $s_{i,j}^{n,m}$ and $s_{i+\delta i,j+\delta j}^{n+\delta n,m+\delta m}$. As can be seen in Equation 2.5, the important parameters to keep track of are the angular separation of the patches

$$\theta = \theta_{obj}\sqrt{\delta n^2 + \delta m^2} \tag{2.6}$$

and the lenslet separation

$$d_{lens} = w\sqrt{\delta i^2 + \delta j^2} \tag{2.7}$$

where θ_{obj} is the angular separation of adjacent patches and w is the lenslet pitch. Substituting Equations 2.6 and 2.7 into Equation 2.5, the layer range for correlations between $s_{i,j}^{n,m}$ and $s_{i+\delta i,j+\delta j}^{n+\delta n,m+\delta m}$ is

$$h = \frac{w\sqrt{\delta i^2 + \delta j^2}}{\theta_{obj}\sqrt{\delta n^2 + \delta m^2}} \tag{2.8}$$

To gain a general understanding of Equation 2.8, it can be useful to examine a few example cases. If $\delta i = \delta j = 0$, then there is no lenslet separation and the information obtained relates to the ground layer $(h = 0)$. If we look at the same patch through different lenses, then $\delta m = \delta n = 0$ and the impulse response function is obtained. The impulse response function is typically labelled $A(\delta i, \delta j)$ and is discussed further in Section 2.3.1.2. Other cases to note are the minimum and maximum ranges sampled. For a given lenslet array, let the total number of lenses be $n_{lens} \times n_{lens}$. Similarly, the field viewed will be broken into $n_{obj} \times n_{obj}$ patches. Aside from sampling the ground layer as previously mentioned, there is a maximum range from the entrance pupil that can be sampled along with a minimum range. To sample the layer nearest the pupil, one would use slopes with the largest object separation viewed through adjacent lenslets, which yields the equation

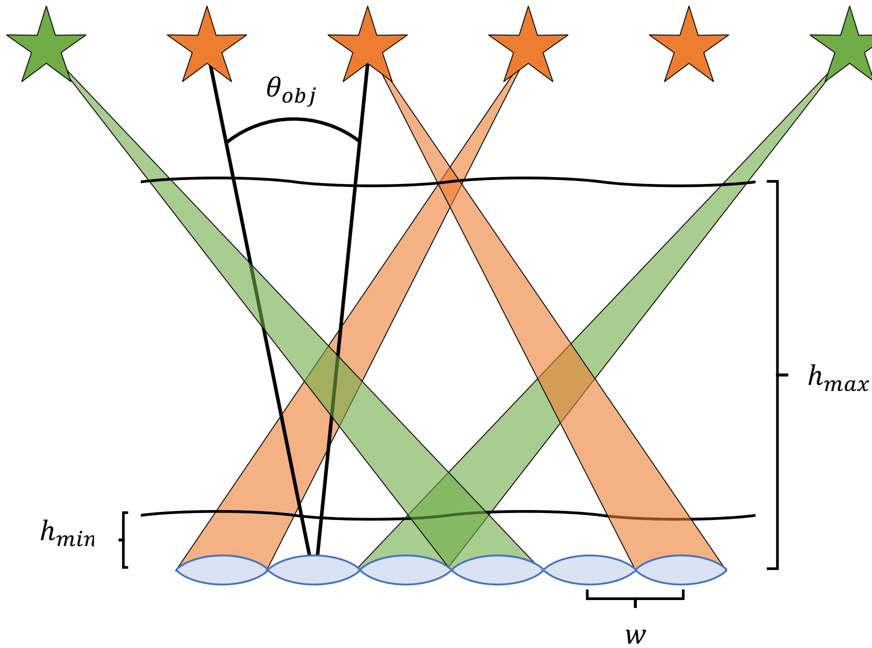

Figure 2.12: Graphical depiction of maximum and minimum sampling ranges for a given lenslet array with lenslet spacing w and an array of objects with angular spacing θ_{obj}.

$$h_{min} = \frac{w}{\theta_{obj}(n_{obj} - 1)\sqrt{2}} \tag{2.9}$$

Alternately, to determine the maximum layer range which can be sampled, one would look at adjacent objects across the largest lenslet separation to get the equation

$$h_{max} = \frac{w(n_{lens} - 1)\sqrt{2}}{\theta_{obj}} \tag{2.10}$$

Graphical representations showing the sampling of both h_{min} and h_{max} are shown in Figure 2.12.

2.3.1.2 Slope Correlation

The strength of a given layer can be determined by how correlated the slopes are from lines of sight that overlap at that layer. To measure the slope correlation, a simple multiplication is used for the x- and y-slopes from the warp map (Wilson 2002). The relative layer strength is given by the equation

$$C(\delta n, \delta m, \delta i, \delta j) = \frac{\langle \sum_{n,m,i,j} s_{i,j}^{n,m}(t) s_{i+\delta i,j+\delta j}^{n+\delta n,m+\delta m}(t) \rangle}{O(\delta i, \delta j)\, M(\delta n, \delta m)} \tag{2.11}$$

where $s_{i,j}^{n,m}(t)$ and $s_{i+\delta i,j+\delta j}^{n+\delta n,m+\delta m}$ are the wavefront slopes from objects (n, m) and $(n + \delta n, m + \delta m)$ respectively seen through sub-apertures (i, j) and $(i + \delta i, j + \delta j)$ during the same frame taken at time t. The summation, $\sum_{n,m,i,j}$, indicates that this process is repeated over all illuminated sub-apertures for all object pairs. The angled brackets, $\langle\ \rangle$, denote time averaging over multiple frames and is discussed in Section 2.3.1.3. $O(\delta i, \delta j)$ is the number of illuminated sub-apertures for the lenslet separation $(\delta i, \delta j)$ and $M(\delta n, \delta m)$ is the number of object pairs for object separation $(\delta n, \delta m)$. These two parameters average the slope contribution from all object and lenslet pairs so that all probed ranges are equally weighted despite some ranges being much more densely sampled than others. By tracking the separation in object and lenslet positions, $(\delta n, \delta m, \delta i, \delta j)$, the probed range is determined using Equation 2.8. In general terms, the SLODAR implementation is accomplished using cross-correlations between sorted warp maps. A detailed description of the software implementation is given in Section 3.5.2.

Typically, the final output of SLODAR includes a deconvolution of Equation 2.11 with the impulse response function defined as

$$\mathrm{A}(\delta i, \delta j) = \frac{\langle \sum_{i,j} s_{i,j}(\mathrm{t})\, s_{i+\delta i,j+\delta j}(t) \rangle}{O(\delta i, \delta j)} \tag{2.12}$$

This is derived from Equation 2.11 when $\delta n = \delta m = 0$. While this deconvolution aids in retrieval of the turbulence profile, deconvolutions can introduce significant error and noise into the system. Simulations were performed to assess the best implementation of the deconvolution for this application, but even with regularization (Tikhonov & Glasko 1965), there was little to no benefit found due to the large increase in noise. Instead, the proposed layer identification technique utilizes a variation of the CLEAN algorithm developed for radio astronomy to remove range-dependent response functions and to identify turbulent layers (Högbom 1974). Use of the CLEAN algorithm is discussed further in Section 2.3.4 and the simulation implementation and results are discussed in Section 3.6 and Section 4.3 respectively.

To recover a one-dimensional estimate of the C_n^2 profile, the final step is to take slices through the datasets based on the object separations (Wilson 2002; Butterly et. al 2006). Two objects will only exhibit a correlation along the direction of their separation. If the data is sorted such that a given object is represented by a $n_{lens} \times n_{lens}$ warp map, then $C(\delta n, \delta m, \delta i, \delta j)$ is easily computed via a cross-correlation between the warp maps of the two objects. The resulting two-dimensional matrix gives correlation information for each pair of lenslets in the array and must be normalized by the matrices $O(\delta i, \delta j)$ and $M(\delta n, \delta m)$. A corresponding height matrix is computed for each of these points using Equation 2.8. The correlation and height matrices are sliced along the direction $\langle \delta n, \delta m \rangle$ and the two resulting vectors are the correlation strength and the corresponding altitude. Performing this analysis for each pair of objects and combining the results yields the estimate of C_n^2 for each of the sampled ranges. The correlation strength vector can be averaged over several frames to improve the estimate as needed for the given system.

2.3.1.3 Sampling Density

The density of measurements can be adjusted by changing the parameters ${FOV}/{\theta_0}$ and ${D}/{w}$ as alluded to in Section 2.1. The layer range from the telescope pupil for a given object and pupil baseline is given in Equation 2.5 in a way that readily shows how these parameters affect atmospheric sampling. Increasing the FOV increases the maximum angular separation (θ) and increases sampling towards the pupil. The addition of lenslets increases overall sampling density and can slightly increase d_{lens} as lenslet centers are pushed closer to the edge of the entrance pupil. Increasing either factor increases the sampling towards the scene. In general, the number of samples through the atmosphere is as a function of both the number of points in the scene ($N_o = n_{obj}^2$) and the number of lenslets in the array ($N_L = n_{lens}^2$) and is given in the equation

$$N_{Samples} = \frac{N_o(N_o - 1)\sqrt{N_L}}{2} \qquad 2.13$$

One additional benefit of the dense sampling offered by a grid of evenly space objects in the scene is the ability to decrease the necessary number of frames that need to be averaged in the slope correlations given in Equation 2.11. Because the total aberration seen along a given line of sight is the combined effect of several turbulent layers, many slope correlations are necessary to determine where the significant layers are located. Aberration from the non-correlated layers will average to zero given a sufficient number of data points, so the traditional solution is to average over many frames to see positive correlation. To demonstrate the sampling that can be achieved using an object rich scene, a histogram of the range sampling for the benchtop simulation described in Section 3.1.2 is shown in Figure 2.13. This system has a pupil width of 11.25 mm sampled using a 10×10 lenslet array. The simulated WFS is viewing a 0.995° FOV broken into 15× 15 object patches. Key features of this plot are the high sampling of the ground layer and dense sampling of ranges were $h < \frac{w}{\theta_{obj}}$. There are several regions where no data is collected especially towards h_{max}. This occurs because there are no combinations of integer lenslet spacings, $(\delta i, \delta j)$, and integer object spacings, $(\delta n, \delta m)$, which probe these ranges. With such a histogram and a knowledge of system objectives and environments, the WFS can be designed such that the ranges of interest are sampled most densely. The fact that there is a dense population of layers sampled more than 20 times per frame allows for more averaging to take place with each frame captured compared to SLODAR using guide stars with irregular spacings (Wilson 2002; Wang et. al. 2008). While traditional SLODAR averages over timescales on the order of minutes, this technique allows for averaging over a reduced number of frames for faster characterization of the atmosphere.

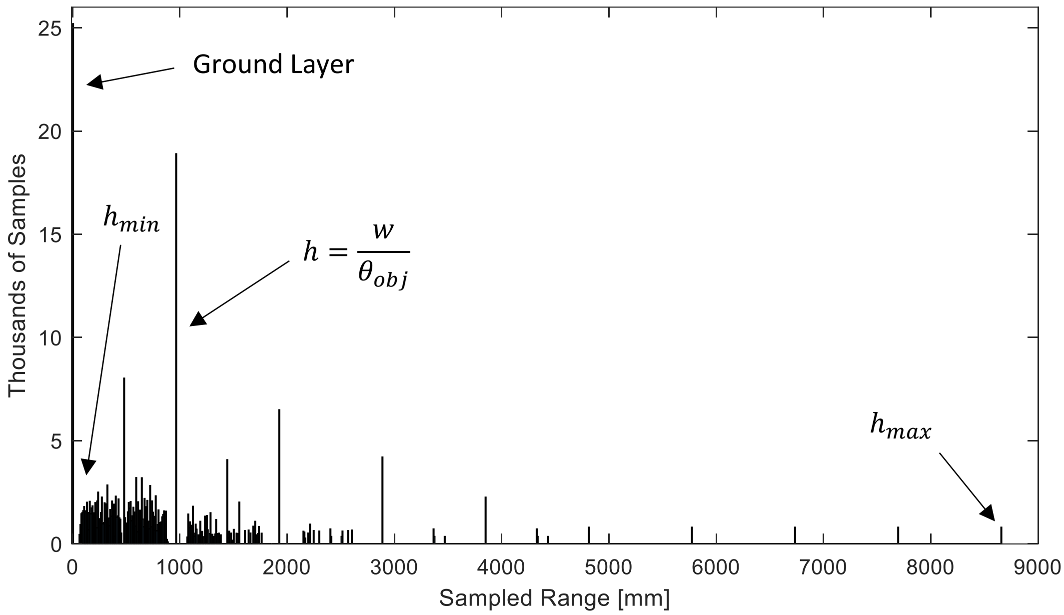

Figure 2.13: Histogram showing layer sampling for a 15×15 grid of object points viewed through a 10×10 array of lenslets. Of particular interest is the high sampling of the ground layer and a very large h_{max} compared to the bulk of the sampling.

2.3.2 Wind Speeds

While the turbulence profile is measured with each WFS frame, additional atmospheric parameters and increased resolution are achieved by looking at information stored in warp maps between consecutive frames (Schock & Spillar 1998, St. Jacques 1998, Wilson 2002, Wang et. al. 2008). This comparison is achieved via a cross-correlation similar to Equation 2.11 with the slope measurements taken from different frames separated by δt as shown in Equation 2.14

$$C(\delta n, \delta m, \delta i, \delta j, \boldsymbol{\delta t}) = \frac{\langle \sum_{n,m,i,j} s_{i,j}^{n,m}(t) s_{i+\delta i,j+\delta j}^{n+\delta n,m+\delta m}(t + \boldsymbol{\delta t}) \rangle}{O(\delta i, \delta j)\, M(\delta n, \delta m)} \quad 2.14$$

Equation 2.14 is also typically deconvolved by the impulse response function in Equation 2.12 when recovering the atmospheric profile. It is likely that an implementation of the CLEAN variation would be preferred in this application as well, but the simulation of such lands outside the scope of this work. The cross-correlations across multiple frames each separated by δt shows motion in the peaks of the SLODAR data that can be tracked over time to recover wind velocity, layer ranges, and layer strengths. This formalism assumes the frozen-flow hypothesis in which each layer of atmospheric turbulence is a fixed phase disturbance that flows in the direction of the wind vector corresponding to that layer (Taylor 1938). Using this hypothesis, atmospheric aberration measured in one warp map will show strong correlation to offsets in the warp map from an adjacent frame. It has been shown that the frozen flow hypothesis can apply to Shack-Hartmann WFS measurements of atmospheric turbulence over short time scales and that looking at correlations between adjacent frames does yield the velocity for significant turbulence layers (Poyneer et. al. 2009; Shöck & Spillar 1998; St. Jacques 1998; Gendron & Léna1996). Wang et. al. (2008) and Osborn (2010) have also shown that the turbulent patches can be tracked across the scene using the SLODAR data to determine the horizontal wind velocity and the range of these layers for a second, independent way to determine the C_n^2 profile and increase the SLODAR resolution.

For a graphical depiction of the spatio-temporal correlation of turbulence, Figure 2.14 shows two layers with different ranges and wind speeds passing through light from a pair of objects viewed by a lenslet array. One layer is depicted as moving slowly near the telescope pupil while

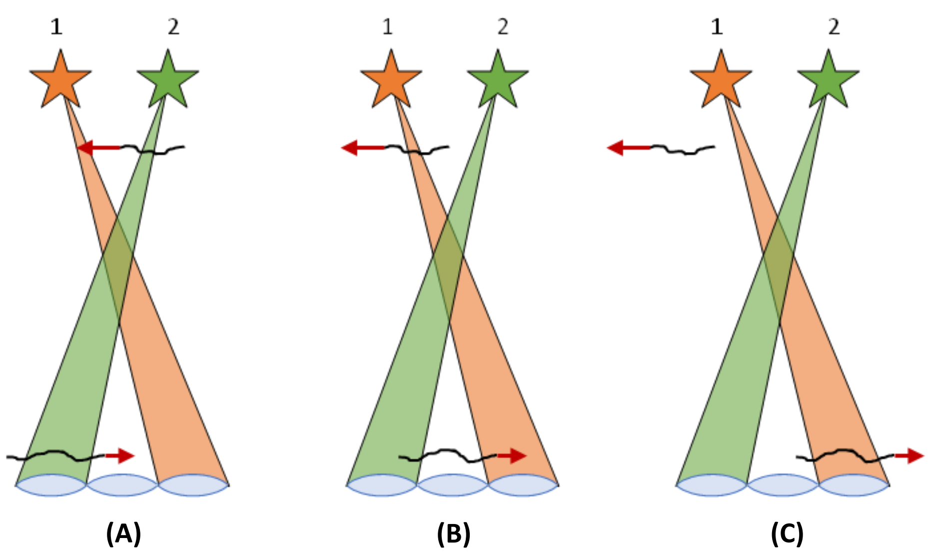

Figure 2.14: Example of turbulent patches from separate layers blowing across the telescope pupil. (A) shows the initial condition with turbulence both near the pupil and near the object, (B) shows the turbulent regions of interest after some time Δt, and (C) shows the turbulent regions after $2\Delta t$.

the other moves quickly closer to the objects. It is assumed that each figure is separated by some time, Δt, and that the turbulence can be modeled as a frozen phase screen over these frames. If we take the warp map from Frame A of Figure 2.14 and perform a cross-correlation with Frame B, there will be a peak corresponding to the high layer moving between objects 1 and 2. Similarly, a cross-correlation between Frames A and C will show a peak due to the aberration being the same within the low layer. Since the time gap between frames is well known, we can infer how far each layer traveled in each frame and determine the wind velocity driving the turbulence in that layer.

2.3.3 Frozen Flow Modeling

Knowing the wind velocity as well as the past reconstructions of a phase of a layer, the frozen flow hypothesis described in Section 2.3.2 is implemented to increase the resolution of the layer reconstruction. This assumes that the primary features of the phase disturbance for a given layer travel across the telescope's field of view without significant degradation on short time scales. Because of this, past realizations can be implemented with the current reconstruction to interpolate layer features smaller than the lenslet array would typically allow during reconstruction of a single instance. This technique interpolates the layer features on time scales much longer than the atmospheric coherence time, τ_0, while each frame is taken with τ_0 as the upper bound on integration time as described in Section 2.1. Jefferies and Hart (2011) were able to show that implementation of the frozen flow hypothesis on timescales of $10\tau_0$ dramatically increases the layer reconstruction quality and the recovered image quality when implementing deconvolution from wavefront sensing (DWFS) as described briefly in Section 2.5.2. The interpolation technique using the frozen flow hypothesis is performed in real-time alongside the layer reconstructions. This allows the improved three-dimensional atmospheric reconstruction to be used for higher quality estimates of the field-dependent point spread functions used in the image deconvolution.

2.3.4 CLEAN Algorithm Variation

To implement the variation on the CLEAN algorithm (Högbom 1974), the results from Equation 2.11 and Equation 2.14 are processed to recover one-dimensional turbulence profiles. All the one-dimensional slices are combined and averaged to produce the final estimate of the C_n^2 profile. Implementation of the CLEAN algorithm first requires an understanding of the range-dependent impulse response function for a given layer. This is computed by simulating the warp maps and corresponding correlation strength vectors for turbulence at a given range through several independent realizations and averaging the results to produce the impulse response for that range. The range dependent responses are characterized into an appropriate functional form. For this application, the use of a Lorenztian fit described as

$$L(a,b,c,d) = (c-d)\left(\frac{b^2}{(x-a)^2+b^2}\right)+d \qquad 2.15$$

was found to be a good, localized representation of the impulse response. The fitting parameters in Equation 2.15 allow for variation in the vertical offset (d), the amplitude $(c-d)$, the peak location (a), and the width (b) of the Lorentzian profile. With the functional form of the responses defined, the CLEAN algorithm searches for peaks larger than some pre-defined threshold, fits a response function to that peak, records the fitted peak location (a) as the layer range, records the Lorentzian amplitude (c) as the relative layer strength, and removes the peak from the dataset. This process is repeated until all identified peaks are removed from the dataset. The layer ranges are now used in the atmospheric reconstruction described in Section 2.4. More information about the implementation of these techniques are given in Section 3.6 and simulation results are provided in Section 4.3.

2.4 Atmospheric Reconstruction

With the atmospheric profile measured and ranges to significant layers computed, the sensing of the atmosphere is complete. The next step in correcting the atmospheric aberration is reconstruction of the phase disturbance imparted by each layer. This process includes either a hardware or software calibration of the WFS to determine the response to known inputs at relevant ranges. Calibrations from individual layers can be combined to create a calibration that is suited to the given number of layers and their specific ranges. The combined calibration matrix is then used in conjunction with the warp maps to reconstruct each layer giving an overall estimate of the volume of turbulence through which the scene is observed.

2.4.1 Response Matrices

The atmospheric reconstruction begins with a calibration of the WFS. The calibration of the WFS is range dependent as the anisoplanatic effects grow stronger the further from the pupil the layer is. This can be observed in Figure 2.15 and Figure 2.16 where warp maps are shown for an identical defocus aberration both near the pupil and far from it. The phase disturbance is identical, but the WFS response is quite different. Because of this, it is necessary to calibrate the WFS for each potential range of interest. The calibration for a given range can be generated via measurements in a benchtop environment prior to observation or on-the-fly using simulation software to estimate the WFS response. Once the calibration is performed for each desired range, the calibrations can be combined to allow for reconstruction of all layers simultaneously.

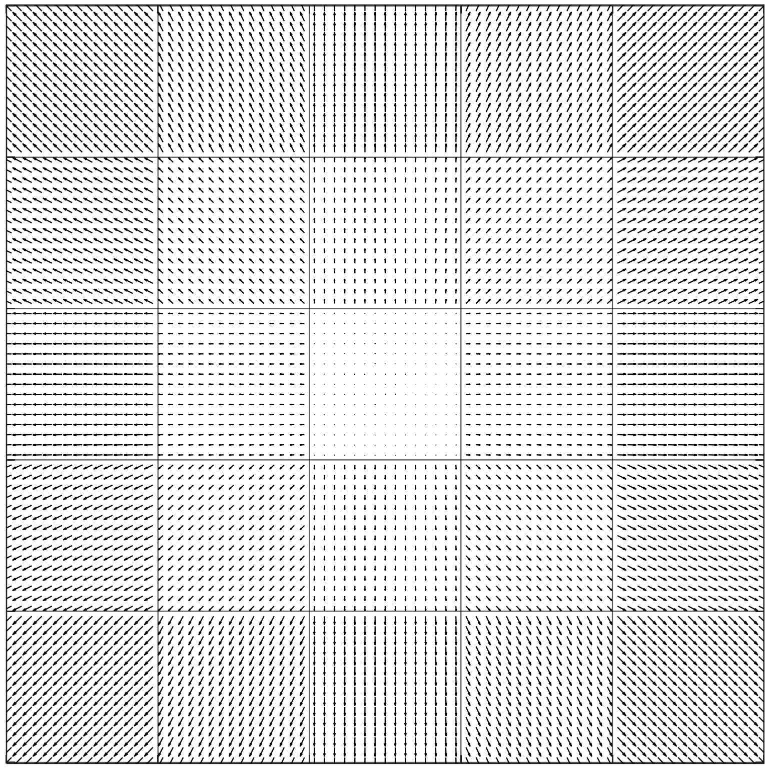

Figure 2.15: Warp map demonstrating defocus aberration from a layer near the telescope pupil. This warp map is generated for a 5×5 lenslet array with 15 object points across the scene.

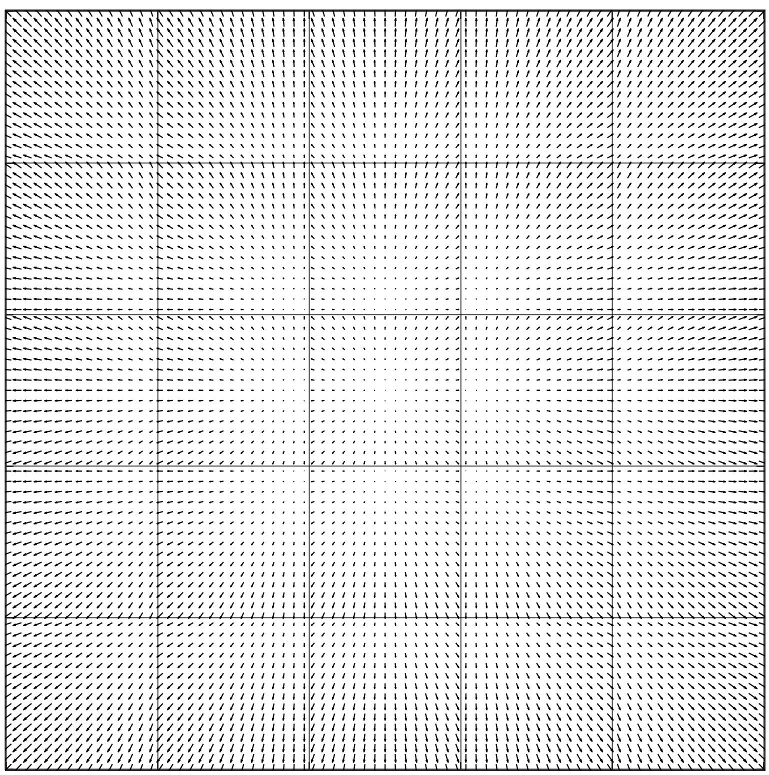

Figure 2.16: Warp map demonstrating defocus aberration from a layer far from the telescope pupil. This warp map is generated for a 5×5 lenslet array with 15 object points across the scene.

To calibrate the WFS for a given range, a response matrix ($\boldsymbol{R}$) is generated by inputting a basis set of known aberrations commonly referred to as “modes”. The WFS response to these input modes are referred to as influence functions. The influence functions allow the aberration seen during operation to be decomposed into the basis set of the input modes. The functional forms of the modes are negotiable but recording each calibration mode along with its corresponding influence function is critical for reconstruction. To generate the response matrix, the wavefront sensor is perturbed using one function from the basis set conjugate to the desired range. The WFS output is analyzed to determine the wavefront slope for each object point within each lenslet. The slope information that is output is then formatted into a column vector containing both the x- and y-slope information. An example slope vector for a calibration containing $n \times n$ lenslets and $m \times m$ objects is given in Equation 2.16

$$S = \begin{bmatrix} Sx_{1,1} \\ Sx_{1,2} \\ \vdots \\ Sx_{1,m^2} \\ Sx_{2,1} \\ \vdots \\ Sx_{n^2m^2} \\ Sy_{1,1} \\ Sy_{1,2} \\ \vdots \\ Sy_{n^2m^2} \end{bmatrix} \tag{2.16}$$

The manner of sorting the slopes is not important so long as it is consistent for each influence function and maintained throughout the atmospheric reconstruction. The response matrix is then built by combining the slope vectors from all modes into the columns of the response matrix as

$$\boldsymbol{R} = [S_1 \quad S_2 \quad \cdots \quad S_{M_{modes}}] \tag{2.17}$$

where M_{modes} is he number of calibration modes. Once all influence functions have been measured and input as columns, the response matrix for the given range is complete. Response matrices for multiple ranges can be combined by appending the columns of the response matrix for a single range to the response matrix of another as

$$\boldsymbol{R}_{\boldsymbol{atmosphere}} = \left[\boldsymbol{R}_{\boldsymbol{Range1}} \quad \boldsymbol{R}_{\boldsymbol{Range2}} \quad \cdots \quad \boldsymbol{R}_{\boldsymbol{RangeN_{layers}}}\right] \tag{2.18}$$

where the atmosphere is comprised of N_{layers} layers of interest. With this in mind, it is possible to store a library of response matrices and simply call and combine the matrices relevant to the current combination of atmospheric layers once they are retrieved from the SLODAR algorithms. This allows for the accommodation of a changing number of layers each with a dynamic range and allows the required flexibility for a mobile platform or moving target.

2.4.2 The Reconstruction Matrix

With the response matrix $(\boldsymbol{R})$ identified for the given atmospheric conditions, a reconstruction matrix can be formed. For any given disturbance, the slope vector can be written as a linear combination of the basis vectors in the response matrix through the equation

$$S = \boldsymbol{R}\Phi \tag{2.19}$$

where Φ is an $\left[M_{modes} \cdot N_{layers} \times 1\right]$ column vector describing the relative contribution of each mode. When the WFS measures the atmosphere, it outputs the slope vector (S), so to retrieve the phase responsible for the observed aberration one needs to solve the inverse problem such that

$$\Phi = \boldsymbol{R}^{-1}S \tag{2.20}$$

Because the response matrix, $\boldsymbol{R}$, is a $\left[m^2 \cdot n^2 \times M_{modes} \cdot N_{Layers}\right]$ dimensional matrix where the number of data points per mode for exceeds the number of modes and layers, it is overdetermined. The reconstruction matrix, $\boldsymbol{R^{-1}}$, is computed using the pseudoinverse of the response matrix (Moore 1920; Penrose 1955). This is accomplished using singular value decomposition (SVD) such that

$$\boldsymbol{U\Sigma V^T} = SVD(\boldsymbol{R}) \tag{2.21}$$

The unitary matrix $\boldsymbol{U}$ contians wavefront sensor modes and the unitary matrix $\boldsymbol{V^T}$ contains the corresponding influence modes (Tyson & Fazier 2012). The matrix $\boldsymbol{\Sigma}$ is a diagonal matrix containing the singular values which represent the relative responsivity of the wavefront sensor to the influence modes. The singular value matrix is typically truncated to reduce the effect of null-modes. These are modes that the wavefront sensor cannot respond to and incuding these in the reconstruction will add significant noise to the reconstructed phase. To retrieve the psuedoinverse of the response matrix, the matrices are combined such that

$$\boldsymbol{R^{-1}} = \boldsymbol{V\Sigma^{-1}U^T} \tag{2.22}$$

where $\boldsymbol{\Sigma^{-1}}$ is computed by inverting the non-zero matrix elements.

Typically the reconstructor is built once for the system and needn't be revisted unless a recalibration is taking place. To support a system that is adaptable in real time to different turbulent layers, I propose that the response matrix for each layer be computed on-the-fly using a simulation of the WFS response. The turbulence profile measured in Section 2.3 can be used to select which atmospheric ranges matter and thus which ones will be used in building a reconstruction matrix. The required atmospheric response matrix, $\boldsymbol{R_{atmosphere}}$, is then built by combining the layer response matrices from all important altitudes on an as needed basis and a custom reconstruction matrix, $\boldsymbol{R^{-1}}$, is developed based on current turbulence properties. This allows for a numerical reconstruction of the turbulent layers which are important to the current atmosphere and this reconstruciton matrix can be updated frequently.

2.4.3 Reconstructing Layers

With the turbulence profile measured and the appropriate reconstruction matrix developed for a given number and composition of layers, the atmosphere is reconstructed using Equation

2.20. The current warp map is formatted into the column vector, S, containing the x- and y-slopes utilizing the same sorting method as was used in building the response matrix. Multiplying by the reconstruction matrix, $\boldsymbol{R}^{-1}$, yields the weighting of each of the influence functions used in the calibration, Φ. This includes weightings for each layer if multiple layers were included in the reconstruction matrix. The atmosphere is then reconstructed by recalling the library of influence functions in the same order they were inserted into the response matrix, multiplying each by its corresponding weight, and then summing all of the functions that apply to a given layer. This gives a two-dimensional estimate of the phase disturbance for each range of interest. This reconstructed volume of atmosphere allows PSFs to be calculated along any given line of sight. The resolution of each layer can be increased using past reconstructions and each layer's wind velocity using the frozen flow model as was discussed in Section 2.3.3.

2.5 Image Correction

The final step in the operation of the WFS is the image correction. To facilitate a flexible system, the proposed image correction is a software-based removal of the PSFs via deconvolution rather than correction via an adaptive element such as a deformable mirror. This method has been demonstrated in other experiments as a viable method for image correction (Primot 1990, Welsh 1995, Mugnier 2001). Due to the anisoplanatic effects of the atmosphere, field-dependent PSFs are computed and removed by virtue of a Wiener filter to correct aberrations in the science image.

2.5.1 Computing Field-dependent PSFs

Using the atmospheric measurement and reconstruction process described in Section 2.3 and Section 2.4, all of the significant turbulent layers have been identified and phase estimates of each have been developed. Traditionally these phase estimates would be inverted, scaled, and applied to deformable mirrors (DMs) appropriately conjugated to each layer, but the reconstructions can instead be used to compute field dependent PSFs. To retrieve the field dependant PSFs, the footprint of a given object patch from the scene is projected through the three-dimensional, numerically reconstructed atmosphere to the science camera as shown in Figure 2.17. The resulting portions of each phase screen are summed to compute the total two-dimensional phase disturbance along the given line of sight. For distant objects, the entrance pupil is simply projected along a line of sight to the scene, but with fully distributed turbulence or shorter ranges to the object of interest, the summing is somewhat more complicated as the cone of light must be accounted for in the propagation and summing process. With the total phase disturbance known, the modulus square of the Fourier Transform yields the appropriate PSF for a given object patch. There will be some error due to the discretization of the atmosphere, but the major sources of degradation are calculated and anisoplanatic PSFs across the entire scene are recovered as the process is repeated for each line of sight to the scene.

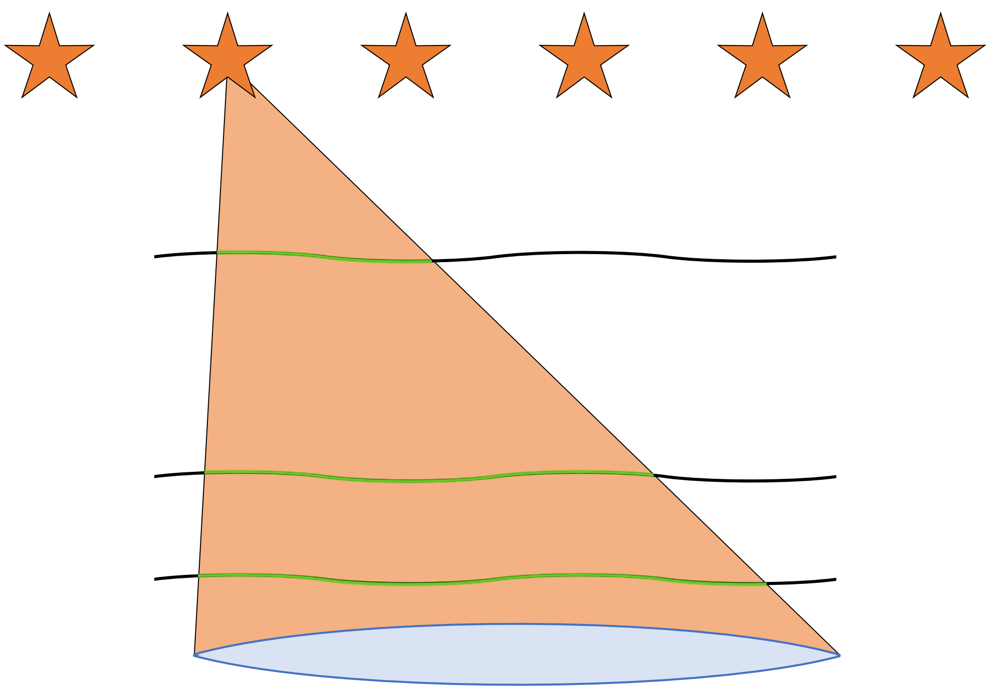

Figure 2.17: Graphical depiction of the portions of turbulent layers summed to compute a PSF for the given line of sight.

2.5.2 PSF Deconvolution

Computing the PSFs for each isoplanatic patch within the image as described in Section 2.5.1 allows a software-based correction via localized deconvolution. To begin this process, the overall tip and tilt for each patch in the image is computed and removed by applying the bulk shift to the center pixels in each patch and interpolating the effects to pixels between patch centers. This shift of regions within a patch is applied to rid the image of large-scale distortion between patches. Correction of higher order aberration with each image patch is then realized by deconvolution of the science image with the tilt-removed PSF using a Wiener filter of the form

$$W(u) = \frac{H^*(u)}{(H(u)^2 + \Phi)} \qquad 2.23$$

where $H(u)$ is the Fourier transform of the PSF and Φ is a user defined filter width (Bates & McDonnell 1986). The filter width, Φ, offers a free parameter in the correction that allows tuning based on the as-built system and local atmospheric conditions. Widening the filter reduces noise in the corrected image, but the image correction improves when the filter is narrowed. With the filter defined, the final step is applying the multiplicative deconvolution

$$f(x) = F^{-1}(A(u) * W(u)) \qquad 2.24$$

where $A(u)$ is the Fourier transform of the portion of the science image being corrected and $f(x)$ is the corrected image patch. Correction across the entire FOV is achieved once each patch has undergone the de-warping and deconvolution process yielding a version of the science image that has been corrected to remove the induced atmospheric aberration.

Chapter 3: Simulation and Algorithms

To verify the theory behind the WISH WFS and to understand the theoretical performance of such a system, a simulation was developed which models a benchtop prototype version of the WFS. This simulation effort is further supported by a preliminary design used to capture images for development of image processing tools which enable warp map computation. Simulating such a benchtop system allows for an atmosphere with a varied number of turbulence layers each with adjustable ranges and Fried parameters. The scope of this work, as described in Section 1.3, is the verification and characterization of the WFS for the static turbulence case. As such, dynamic turbulence has not been modeled in the simulation and incorporation of wind speed analysis and frozen flow modeling are left as future work. This simulation additionally does not address image deconvolution as this is a topic addressed in other works as previously noted (Primot 1990, Welsh 1995, Mugnier 2001). The scope of the simulation and benchtop development is shown graphically in Figure 3.1 where boxes outside the scope of both the simulation and benchtop experiment are outlined in red and faded.

The goal of the simulation and benchtop work is to provide a proof of concept showing successful reconstruction of multiple static turbulence screens. Section 3.1 discusses the relevant system parameters for both the simulation and benchtop work. The image processing algorithms are described in detail in Section 3.2. Generation of synthetic turbulence layers is discussed in Section 3.3 while Section 3.4 describes the transition to warp maps. Section 3.5 discusses the SLODAR implementation with Section 3.6 describing the layer identification using the variation on the CLEAN algorithm. Finally, Sections 3.7 and 3.8 discuss generation of the response matrix and the reconstruction of the atmosphere respectively.

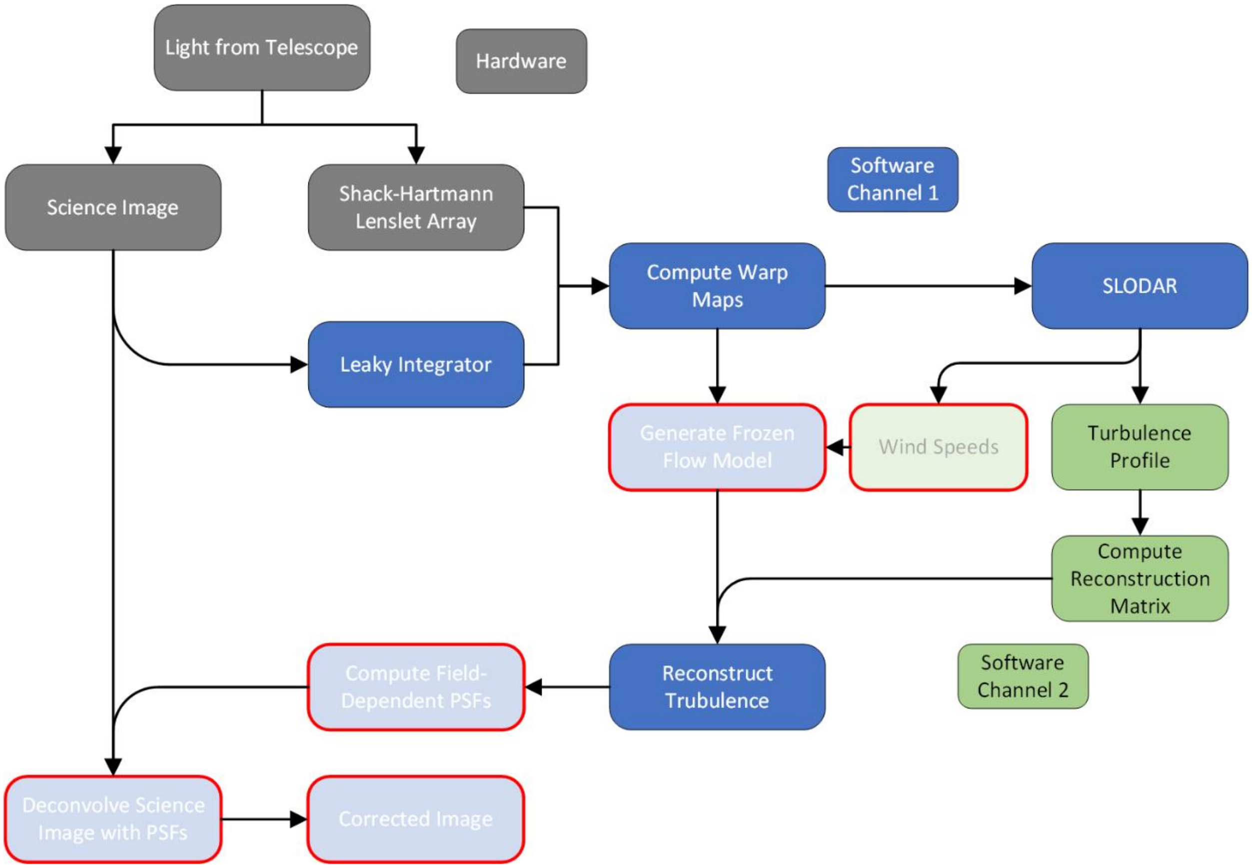

Figure 3.1: Block diagram showing the flow of data and the analyses performed. Sections of the diagram which fall outside the scope of this work are faded and outlined in red. These items are not addressed in either the simulation or benchtop design.

3.1 System Design and Simulation Parameters

To provide a proof of concept for the WISH wavefront sensor, a benchtop prototype was designed and built for laboratory testing. The hardware development occurred in parallel to simulation efforts to model the WFS. Because the work occurred in parallel, there are some discrepancies in the final system architecture, but an effort was made to remain consistent between hardware and software applications. These discrepancies and similarities can be seen in the details of Sections 3.1.1 and 3.1.2 where the hardware and software development are discussed respectively.

3.1.1 Benchtop System Description and Scope

The benchtop system is built to capture preliminary image data and demonstrate the process used to partition the science and wavefront sensor images. The system hardware consists of three primary subsystems:

1. The wavefront sensor – The WFS captures and records the aberrated image for processing.
2. The turbulence simulator – This subsystem induces aberration using phase screens to create aberration comparable to that induced by atmospheric turbulence layers.
3. The scene generator – This produces an arbitrary scene for WFS analysis.

The three subsystems are integrated to provide a method of capturing data representative of a telescope imaging through a simplified atmosphere.

This section proposes a fully fleshed out benchtop design with key parameters identified. The hardware was procured and assembled, and some initial work has been done to understand how the system operates. The assembled system is used to capture aberrated images shown throughout this work including the processing of the leaky integrated reference image discussed in Section 3.2.1. These images were used to perform initial investigations into hardware-based warp map computations with the methodology outlined in Section 3.2.2. While the methodology is developed and presented in this work, the computation and verification of such warp maps is largely left as future work as this work is dominantly focused on the development and performance of the wavefront sensor simulation.

The hardware was also used for preliminary reconstructions of arbitrary Kolmogorov aberration. Multiple basis sets were used to attempt this reconstruction including Fourier and Zernike modes along with a poke response basis set. The best reconstructions occurred using a basis set of randomly generated Kolmogorov phase screens. Comparisons of the various basis sets are not presented in this work, but the Kolmogorov basis set has become the baseline reconstruction set for ongoing and future hardware and software investigations.

3.1.1.1 Wavefront Sensor Design Parameters

The benchtop WFS design starts with the camera systems. Two PointGrey Flea3 cameras are used to capture the science and WFS data. A layout of the wavefront sensor subsystem is given in Figure 3.2 showing both the science arm and the lenslet arm of the WFS. The active area for each of these cameras is 5.2 mm × 3.88 mm. Both arms are designed such that light from the scene fills a 3.75 mm square region of this detector to avoid encroaching on the edge pixels. A 5×5 section of the lenslet array shown in Figure 3.3 is utilized to create 25 unique sub-images each captured within the 3.75 mm area on the WFS camera. The optics are designed such that the size of each sub-image matches the size of each lenslet resulting in lenslets with a pitch of 0.75 mm. This keeps lenslet images from overlapping one another on the CCD or from having an abundance of unused pixels. To get the lenslets far enough from the camera to eliminate mechanical interference with the C-mount interface, a 14.25 mm focal length lenslet array is used to achieve an f/19 imaging system. One design goal was to maintain the science camera at a similar f/# using a commercial off-the-shelf (COTS) lens to minimize magnification differences. To this end a 75 mm focal length lens is used to generate an f/20 imaging system for the science camera.

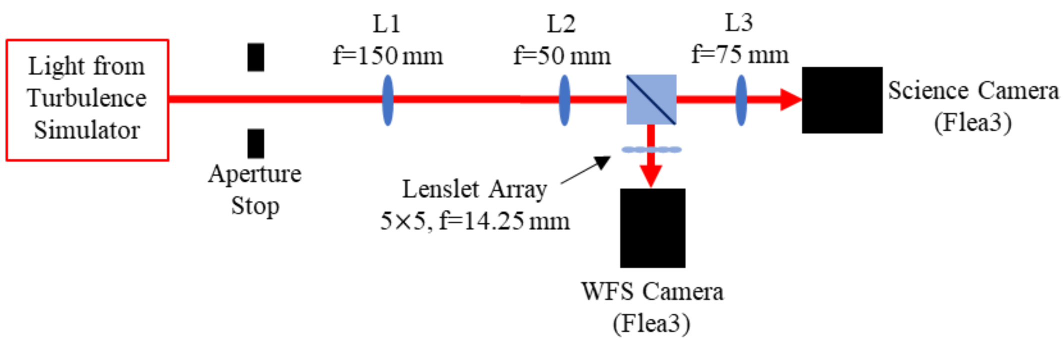

Figure 3.2: Cartoon layout of the benchtop WISH WFS.

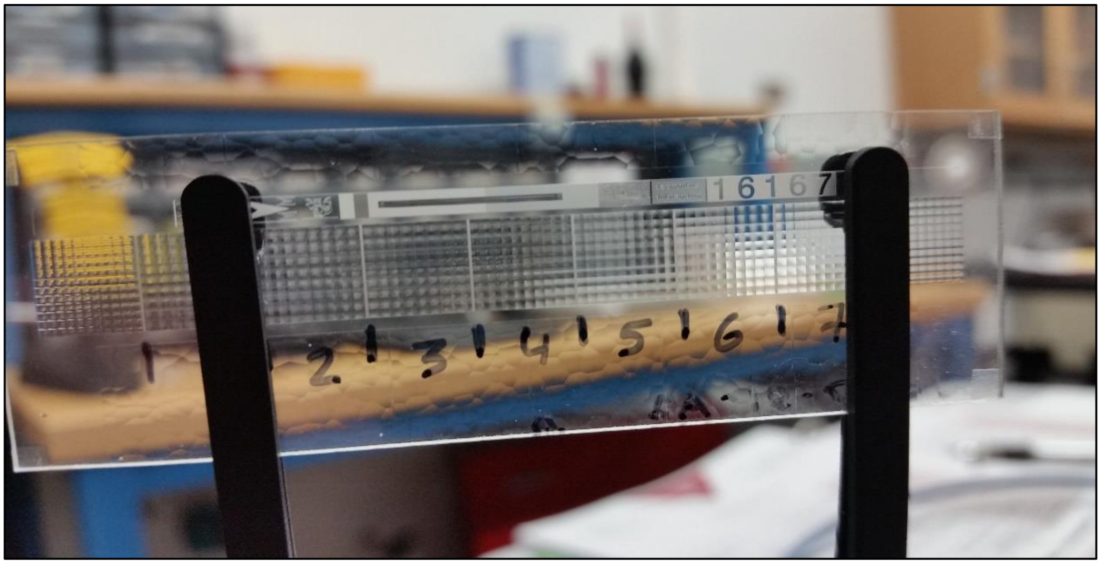

Figure 3.3: Image of lenslet arrays from RPC Photonics. Each 10×10 array offers a different option for lenslet focal length.

The lenslet array is placed conjugate to the telescope's aperture stop and a refractive telescope with 3X magnification is used to re-image the aperture stop onto the lenslet array. This magnification is chosen specifically to allow sufficient space to install phase screens in the turbulence simulator without mechanical interference. This design led to an object space full FOV for the science camera of 0.955° and for the lenslet array of 1.005°. Because the science camera is the limiting case, the remainder of the system is designed around the 0.955° which leads to a small additional separation between sub-images on the WFS camera. For this application a square pupil with a width of 11.25 mm is used to ensure that all 25 of the apertures are fully illuminated and usable. A photograph of the as-built system is shown in Figure 3.4 with the optical path overlaid in red. Table 3.1 summarizes the relevant parameters for the WFS including the details discussed in this section.

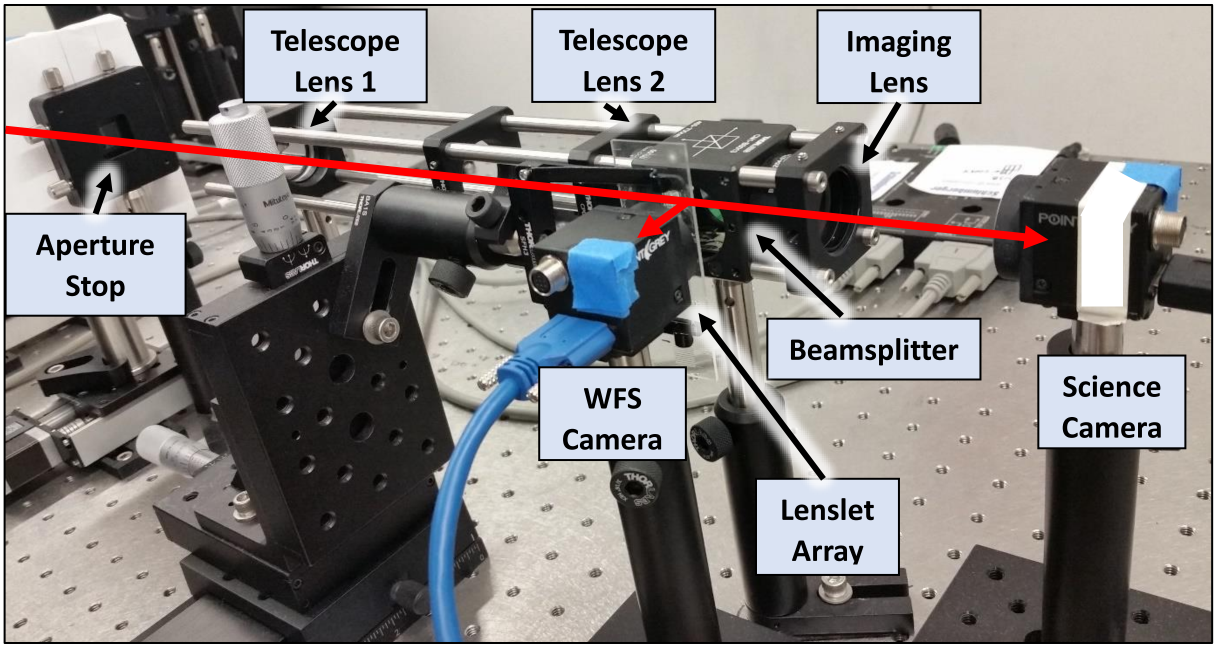

Figure 3.4: Layout of the benchtop WISH WFS.

Table 3.1: Relevant parameters used in the WISH WFS benchtop design

Description	Value	Origin
Pixel pitch	2.5 µm	Constraint (Camera)
Camera sensor size	2080×1552 Pixels (5.2×3.88 mm)	Constraint (Camera)
WFS/Science camera active area	1500×1500 Pixels (3.75×3.75 mm)	Design parameter
Image space f/#	19 (WFS) / 20 (Science)	Constraint (WFS mechanical interface)
Lenslet pitch	0.75 mm	Design Parameter
Illuminated sub-apertures	5×5	Design parameter
WFS telescope magnification	3X	Design parameter
Entrance pupil width	11.25 mm	Derived Quantity
Object space FOV	0.955°	Derived quantity

3.1.1.2 Turbulence Simulator Design Parameters

A synthetic atmosphere is generated using two phase plates to induce aberration representative of atmospheric turbulence effects. The plates were manufactured by Lexitek, Inc. using their Near-Index-Match^{TM} (NIM) production technique to create a custom designed turbulence phase screen. The two phase plates each include two BK-7 windows 100 mm in diameter and 10 mm thick joined by an acrylic layer and a layer of optical polymer. The polymer and the acrylic have a small refractive index difference, Δn. To create the customized phase screen, Lexitek scales a given phase pattern by $\frac{1}{\Delta n}$ and machines this pattern into the acrylic layer which has been deposited on one of the two windows. The optical polymer is then used to fill in the machined pattern and is sandwiched in place by the second window. This creates a phase plate made with any desired pattern within Lexitek's manufacturing tolerances. The final product for a single mounted phase plate is shown in Figure 3.5 with the NIM region identified.

The phase patterns on the procured plates are designed using Matlab to have a Fried length of 1.125 mm over a circular area 83 mm in diameter. The designs were developed following Kolmogorov statistics using the method outlined by Lane et. al. (1992). Interferometer measurements of the regions used in the benchtop tests are shown in Figure 3.6 and yield a measured r_0 value of roughly 1.65 mm which is roughly 50% larger than the intended design. The optical interface to the scene generator consists of a single lens which collimates the light presented

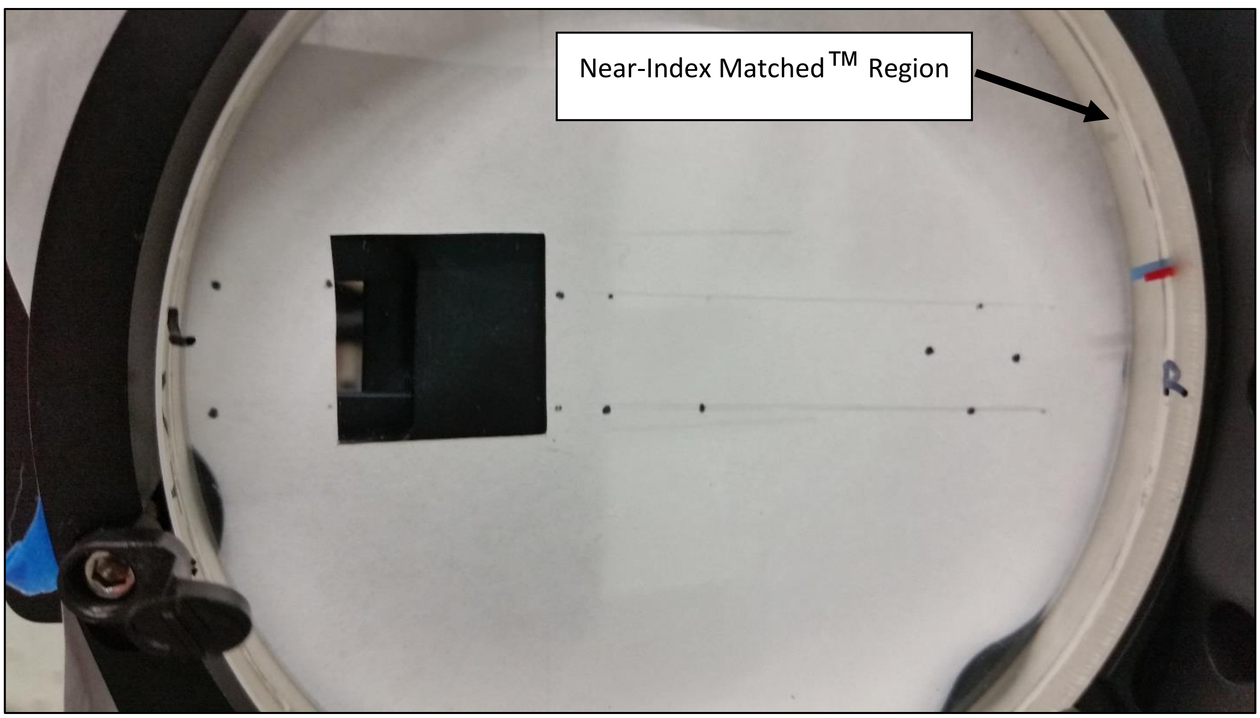

Figure 3.5: Turbulence phase screen developed by Lexitek, Inc. This picture is taken with a windowed region used to limit the transmission area.

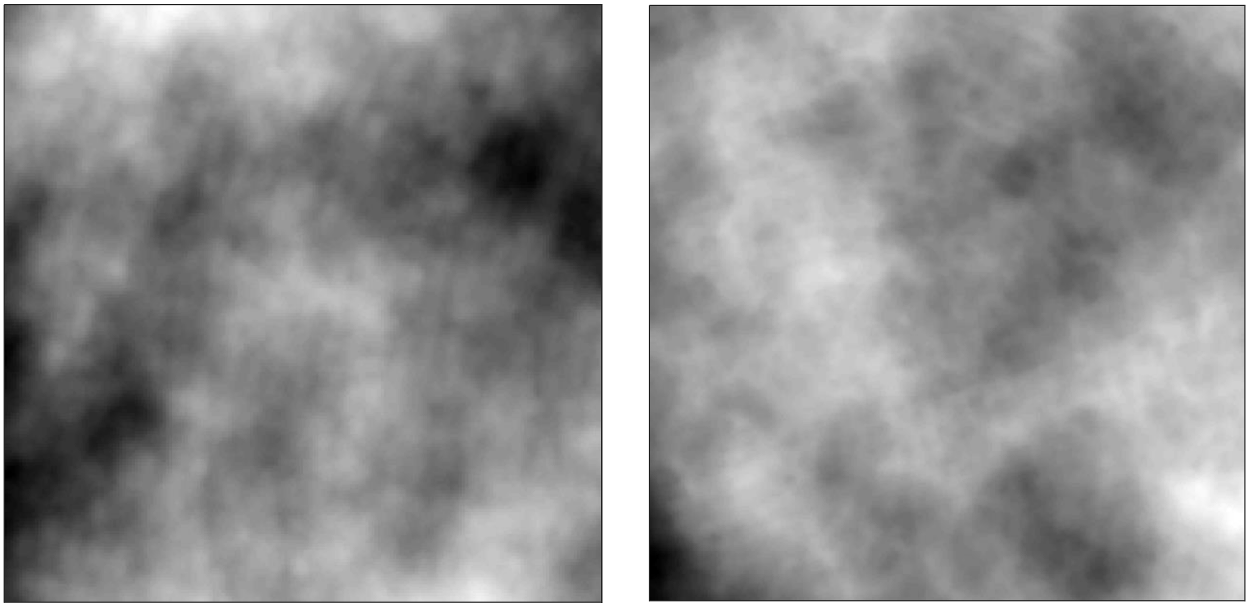

Figure 3.6: Interferometer measurements of the illuminated region of the isoplanatic phase plate (left) and anisoplanatic phase plate (right). Data taken using a Zygo Verifire XPZ interferometer.

to the phase plates and the WFS aperture stop. This allows both screens to operate individually with $\frac{D}{r_0} = 6.8$ regardless of their separation from the WFS entrance pupil.

The use of two phase screens was chosen to facilitate testing with both isoplanatic and anisoplanatic turbulence. This is accomplished by placing one screen as close to the aperture stop as physically possible with the other located some predetermined distance away. An image of the test setup is given in Figure 3.7 with a cartoon layout of the setup given in Figure 3.8. The phase layer of the isoplanatic plate is positioned 19.9 mm from the aperture stop which allows translation of the plate without mechanical interference with the aperture stop. The second phase screen is positioned 283.3 mm from the aperture stop to allow for anisoplanatic effects in the resulting aberration. The optical distance to each phase screen is found by computing the air equivalent thickness, τ, using the equation $\tau = t/n$ where t is the material thickness and n is the corresponding refractive index. The optical distance to the isoplanatic screen is 16.1 mm with the anisoplanatic screen optically separated from the WFS entrance pupil by 271.8 mm. To determine

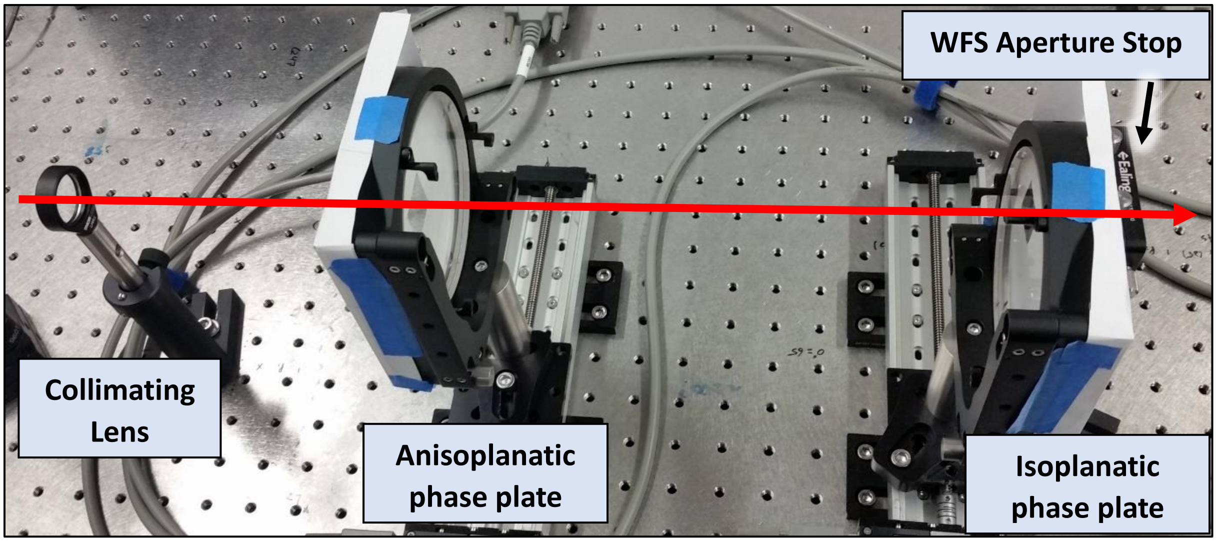

Figure 3.7: Layout of the benchtop turbulence simulator.

the total statistical aberration, contributions from both layers are considered simultaneously. Combining the Fried parameters from multiple phase layers is accomplished using the equation

$$(r_0)_{tot} = \left(\sum_{i=1}^{N} \left(r_{0_i}\right)^{-5/3}\right)^{-3/5} \qquad 3.1$$

which results in an overall Fried length of 1.1 mm for this synthetic atmosphere and a total $\frac{D}{r_0}$ of 10.3. Since the isoplanatic angle for a given layer is proportional to the Fried length as shown in Equation 1.5, combining the isoplanatic angle from multiple layers follows the same formalism given in Equation 3.1. This yields a total isoplanatic angle of 0.1° for a $\frac{FOV}{\theta_0}$ of 9.5 in the science camera and 10.1 in the WFS camera.

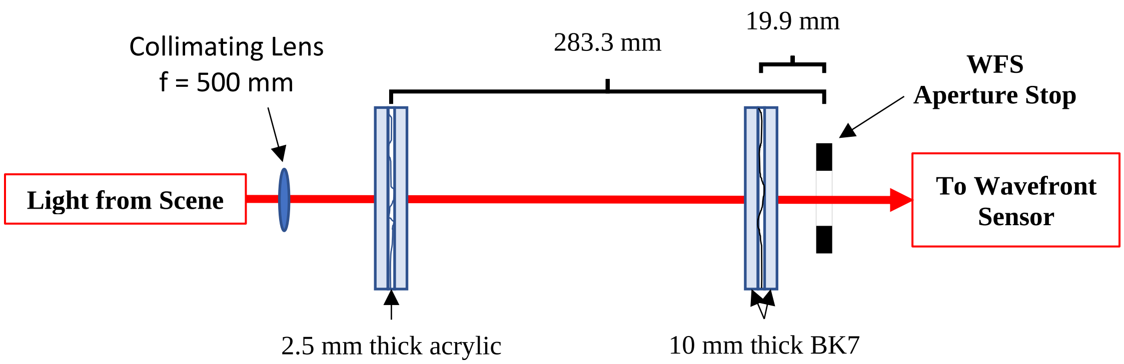

Figure 3.8: Cartoon layout of the turbulence simulator.

The final consideration for the design of the turbulence simulator is the incorporation of dynamic behavior for future work in wavefront sensor analysis. Each phase plate has a clear aperture more than seven times larger than the width of the aperture stop. This allows multiple independent regions of turbulence to be sampled on each of the plates as they are translated within the path of the science light. To create a dynamic atmosphere, each phase plate is mounted on a Zaber LHM150A-T3 linear translation stage with 150 mm of travel. This allows for computer control of each layer to create layer dependent motion and wind speeds. This also allows for leaky integration of the science image to occur as described in Section 3.2.1. Table 3.2 highlights the key parameters used in the design of the turbulence simulator.

Table 3.2: Relevant parameters used in the turbulence simulator benchtop design

Description	Value	Origin
Number of Layers	2	Design parameter
Phase plate clear aperture	83 mm	Design parameter
Phase plate Fried length (r_0)	Designed - 1.125 mm Measured – 1.65 mm	Design parameter Constraint
Layer 1 optical range	16.1 mm	Constraint (Mechanical interface)
Layer 2 optical range	271.8 mm	Design parameter
Sub-system $\frac{D}{r_0}$	10.3	Derived quantity
Sub-system $\frac{FOV}{\theta_0}$	9.5	Derived quantity
Translation stage travel	150 mm	Design parameter
Collimating lens focal length	500 mm	Design parameter

3.1.1.3 Scene Generator Design Parameters

The goal of the scene generator is to produce an arbitrary scene with enough spatial frequency content to allow for correlation between patches of the science image and corresponding sub-image patches from the wavefront sensor arm. To facilitate a variable scene, the scene generator is built around an iPad Mini 2 for generation of a programmable, diverse image. The other critical hardware component in the scene generator is a deformable mirror (DM) which can

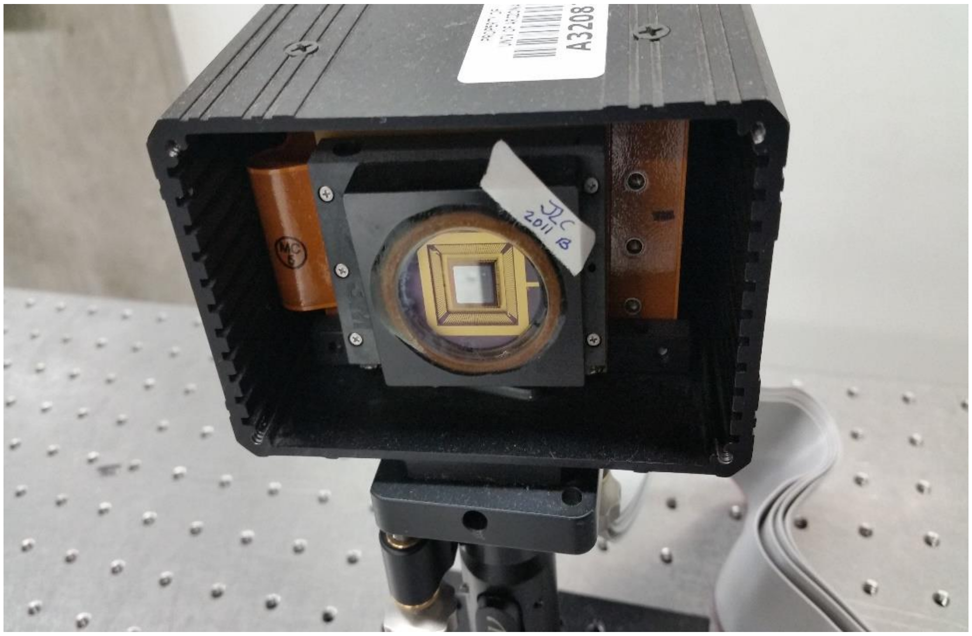

Figure 3.9: Boston Micromachines 140 actuator DM. Used to generate arbitrary modes for future WFS calibration.

be used in future experiments to generate modes for building a response matrix enabling WFS calibration. The part used for this purpose is a continuous face Boston Micromachines DM equivalent to the Multi-3.5 DM with 140 actuators in a 12×12 grid. This mirror is shown in Figure 3.9. The rest of the optics in the sub-system are designed to meet the two primary purposes of (1) coupling the scene to the turbulence simulator and (2) conjugating the DM to the two turbulence layers. A full layout of the scene generator is shown in Figure 3.10 with a picture of the benchtop setup shown in Figure 3.11.

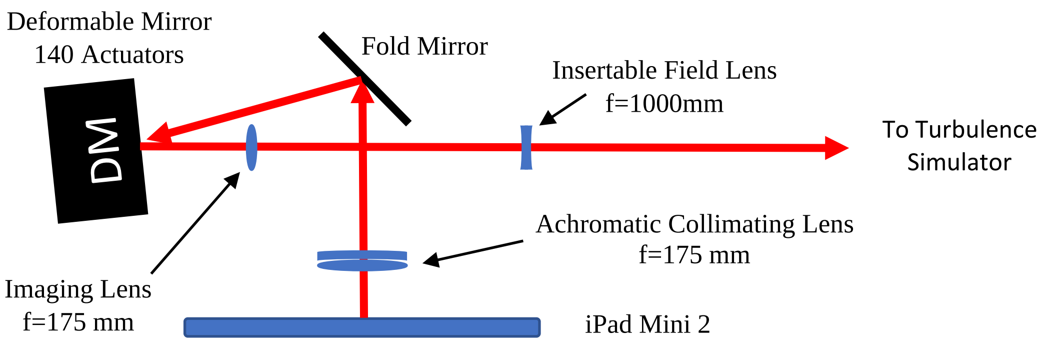

Figure 3.10: Cartoon layout of the scene generator.

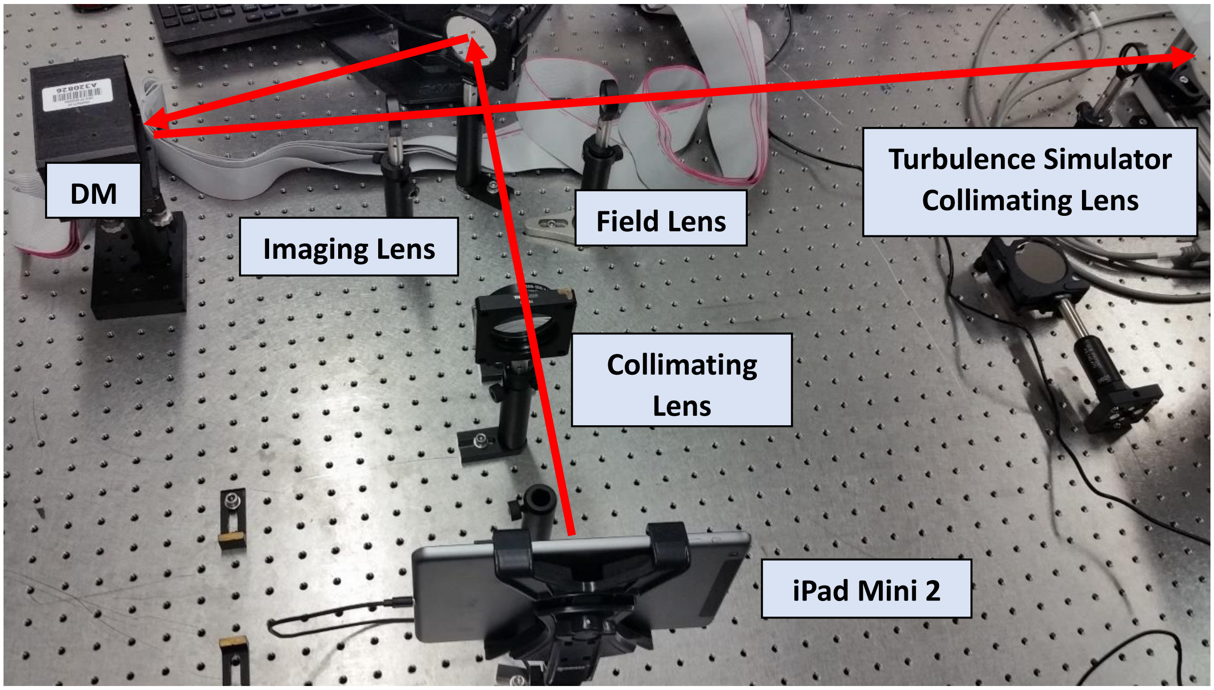

Figure 3.11: Layout of the benchtop scene generator.

The scene generator is coupled to the turbulence simulator by first collimating and then re-imaging the light from the iPad. The light from the scene is collimated using a 200 mm focal length achromatic doublet with a 2 inch lens diameter to collect as much light as possible. After reflection by the DM, the light from the scene is re-imaged through a 175 mm focal length lens which presents the scene to the collimating lens of the turbulence simulator. Viewing the benchtop system holistically, the two lenses in the scene generator comprise the first of three telescopes which make up the entire optical system from scene to detector. The second telescope is formed between the turbulence simulator's collimating lens and the first lens in the WFS and the third telescope is found in the WFS itself. The total magnification of the system is the product of the three telescopes and comes out to $m = \left(\frac{50}{75}\right)\left(\frac{500}{150}\right)\left(\frac{200}{175}\right) = 2.54$ for the science image. With an image size of 3.75 mm, the maximum object size is 9.5 mm or 122 pixels using the iPad's pixel pitch of 72 µm. The actual image generated uses roughly 105×105 pixels to allow for small amounts of misalignment in the overall system and to facilitate each of the 15^2 patches of the object to be comprised of a 7×7 array of pixels.

The positioning of the DM is such that the mirror surface is conjugate to the turbulence layer near the aperture stop. This allows modes generated on the DM to couple into the WFS such that the WFS is calibrated for the isoplanatic layer. To facilitate calibration of the second turbulence layer, a field lens can be inserted at an intermediate image of the scene. This lens does not change the magnification between the scene generator and WFS, but it does change the conjugation of the DM. By inserting a lens with a focal length of 1000 mm, the DM is made conjugate to the second layer for a second plane of calibration for the WFS. The key scene generator parameters are summarized in Table 3.3.

Table 3.3: Relevant parameters used in the scene generator benchtop design

Description	Value	Origin
Object pixel size	78 µm	Constraint (iPad Mini 2)
# of DM actuators	140	Constraint (DM)
Magnification from scene to image	2.54	Design parameter
Maximum object height	9.5 mm (122 pixels)	Derived quantity
Typical object height	8.3 mm (105 pixels)	Design parameter

3.1.1.4 Full System Alignment

With the full system defined, the alignment within and between sub-systems becomes a critical task. To accomplish the alignment of the optical elements, a fiber coupled laser is used in conjunction with the spatial filter depicted in Figure 3.12. The laser is fed through the system in reverse by removing the hardware from one of the WFS arms and inserting the collimated laser directly into the beamsplitter. The phase plates in the turbulence simulator are also removed so that beam quality is maintained from the WFS to the scene generator. The WFS optical components are mounted in a Thorlabs 30 mm cage system for ease of installation and alignment. The laser is

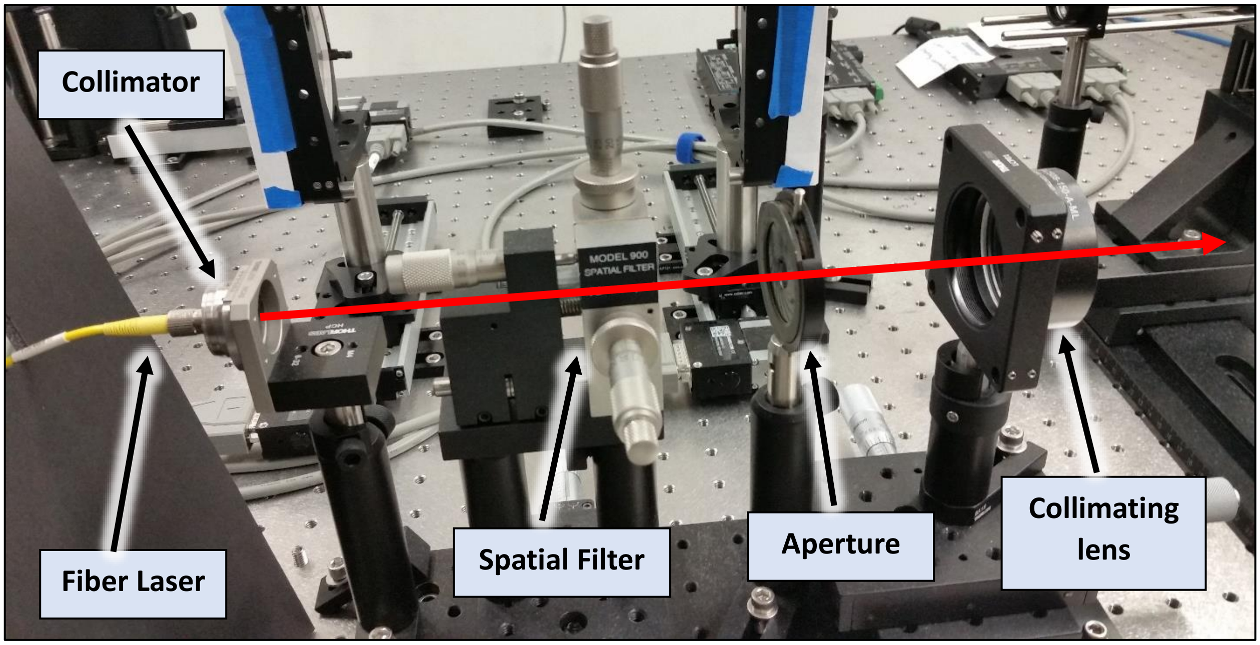

Figure 3.12: Spatially filtered fiber laser used for system alignment.

aligned to this cage system using two fold mirrors and is also used to align the remainder of the lenses and mirrors using typical alignment techniques. Centration of lenses is accomplished using a reference marker recorded prior to lens installation. Once installed, the lens is adjusted until the illumination is once more centered on the reference marker. When necessary, an iris is used to limit the illumination size for increased confidence in centering the illumination on the marker. The axial positioning of lenses was primarily accomplished using a shear plate interferometer to ensure lens spacing adequately collimated the beams where appropriate.

While alignment of most optical elements is relatively straightforward, some additional care is needed for the alignment of the DM. To make sure that the DM is centered on the optical path, the mirror surface is re-imaged onto a PointGrey Grasshopper camera. The mirror surface is illuminated simultaneously with the alignment laser and a flashlight placed outside of the optical path so that features like actuator print-through and wire-bonds can be seen and brought into focus. With the mirror surface imaged onto the camera, the laser is powered on allowing the footprint

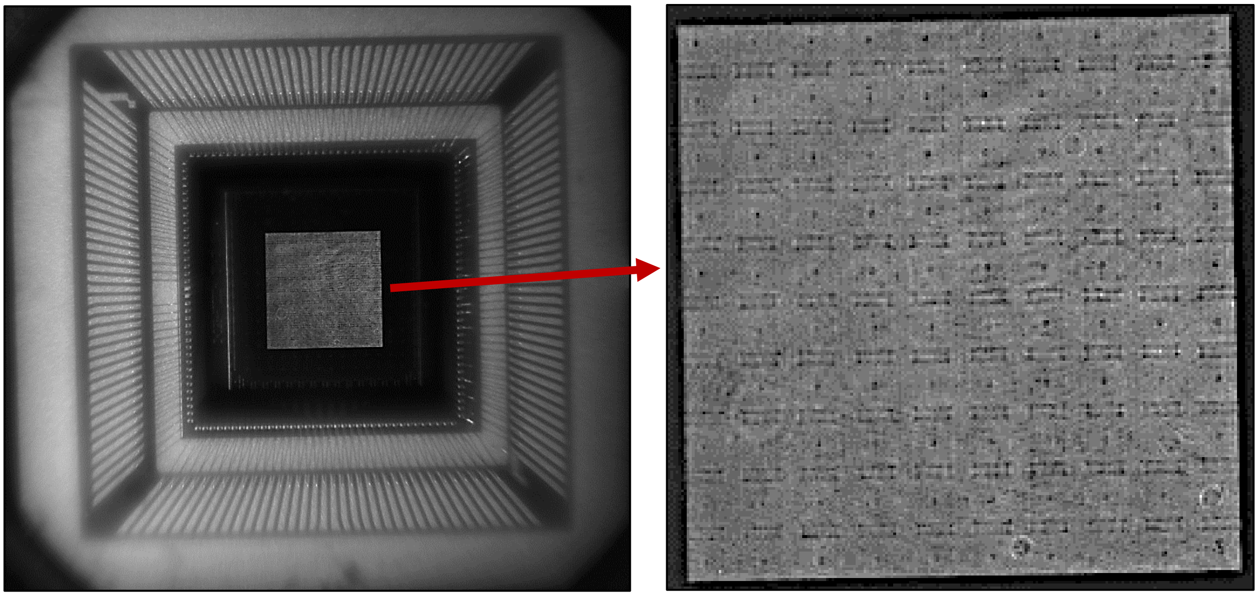

Figure 3.13: Image of DM surface with light from the alignment laser centered on the mirror surface. The left image shows the full mirror surface. The image on the right expands the illuminated region to show the 10×10 array of actuators printing through the mirror surface. The brightness and contrast have been adjusted to increase visibility of the actuators.

from the WFS aperture stop to be viewed with respect to mirror features. The mirror is then aligned so that the aperture footprint is centered on the mirror surface as shown in Figure 3.13.

With the optical elements aligned along a common axis, the final task is ensuring conjugation of the DM to the two phase layers so that future calibration datasets can be captured and used for image correction. Conjugation of the DM to both layers begins by aligning the DM to the isoplanatic layer near the system's aperture stop. A target is placed at the plane of the turbulence layer and is illuminated using a bright light. In this benchtop setup, the target was formed by marking paper with a black Sharpie marker and illuminating from behind with a flashlight. The transmitted light traverses the optical path to the DM surface which is imaged once more by a camera. The position of the DM is adjusted until the target's image coincides with the mirror surface showing that the planes are optically conjugate. Because the mirror position is adjusted during this step, an iterative alignment process is necessary between the alignment laser centration and the phase screen conjugation. When this is finished, the laser is centered on the DM and the DM is conjugate to the isoplanatic turbulence layer. With the DM alignment complete, the field lens is inserted for fine alignment of the anisoplanatic layer. The DM's new conjugate plane is determined by moving the target along the beam path until the target's image is once more clearly conjugate to the mirror surface. An example of a marked target conjugate with the mirror's surface is given in Figure 3.14.

As a final note regarding optical alignment, it is important when using the thick turbulence plates to account for the plate thickness and index when determining conjugate planes. This effect is important in conjugating the DM so that the calibrated ranges match the physical positions of the turbulence layers when generating response matrices. This also needs to be accounted for in the placement of the cameras in the WFS. Alignment takes place with the turbulence plates removed, so re-insertion will add a defocus term into the science images if one is not careful to adjust the final camera position. This was a challenge that was encountered in the data collection of the benchtop experiment and was not fully realized until the data processing was well under way and the benchtop hardware was repurposed for further experimentation.

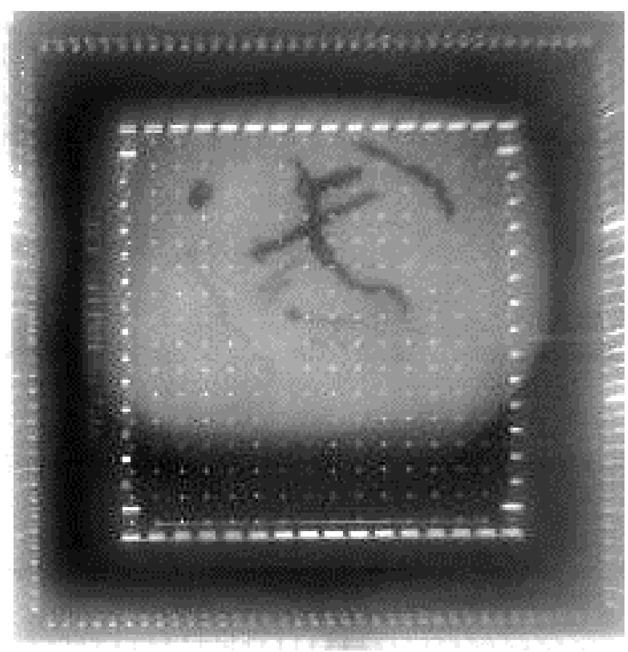

Figure 3.14: An image of the DM surface. The DM is conjugate with a target which contains coarse and fine features to aid in determining the best plane of conjugation. Brightness of the image has been increased for improved visibility.

3.1.2 Simulation System Description

The simulation is developed as a proof of concept for the data processing within the WFS. Because the primary goal is demonstration of successful data processing algorithms, noise sources such as photon noise or read noise have been excluded and remain as future work. The simulation parameters are adjustable, but the parameters used throughout this work were chosen in large part to mirror aspects of physical hardware. The main aspects of the simulation are:

1. The generation of a synthetic atmosphere made up of discrete phase screens.
2. The WFS sampling which measures phase gradients along a specific line of sight.
3. The atmospheric reconstruction which analyzes the phase gradients to predict the location and composition of turbulence layers.

The computational methods are outlined in Sections 3.3 through 3.8, but the parameters used throughout the simulation are discussed below.

The phase screens used in the simulation are created using methods developed by Roddier (1981). The phase screens are generated using random numbers scaled according to Kolmogorov statistics in the Fourier domain so that a unique turbulence pattern is generated each time the function is called. Because of the random nature of the screen generation, the turbulence strength, or Fried parameter, of each produced screen varies somewhat. To adjust the strength of a given layer, the phase can be arbitrarily scaled in amplitude. Alternatively, the pixel pitch of the simulated phase screen can be adjusted to alter the turbulence strength. Scaling either aspect of the screen maintains its adherence to Kolmogorov statistics and continues to mimic physical turbulence. This allows any screen to be scaled to match a desired Fried parameter by setting the width of a pixel and taking an initial measurement of the Fried length. One method to accomplish this measurement comes from theory established for telescope observations (Noll 1976). The Fried parameter for a tilt removed circular portion of a phase screen is related the variance of the phase using the equation

$$\sigma^2 = 0.134\left(\frac{D}{r_0}\right)^{5/3} \tag{3.2}$$

where the variance is in units of radians squared and D is diameter of the telescope pupil. To apply this to the randomly generated screen, one must mask a circular portion of the phase screen and remove the residual tilt of the remaining phase. Using the variance of this circular region, Equation 3.2 can be re-arranged to solve for the Fried parameter

$$r_0 = \left(\frac{0.134}{\sigma^2}\right)^{3/5} D. \tag{3.3}$$

The Fried length of the phase screen can be adjusted to any desired value by multiplying the amplitude of the phase aberration by the scaling factor A which is proportional to the rms wavefront error, σ. This scaling factor is caluclated using the equation

$$A = \left(\frac{r_{0_{new}}}{r_{0_{old}}}\right)^{-5/6} \tag{3.4}$$

where $r_{0_{new}}$ is the desired Fried length of the screen and $r_{0_{old}}$ is the original Fried length. For this simulation, the pixel size of the screens is designed to match the pixel pitch of the interferometer which was used to measure their physical counterparts and is set to is 60 µm. This allows simulations to use either simulated or measured phase screens interchangeably.

While most of the simulation focuses on data processing, there were several physical parameters of the WFS that were necessary to model for generation of data representative of a benchtop system. One of the key parameters of the system is the pupil size which mirrors the hardware at 11.25 mm. Other parameters that match the benchtop hardware are the object space FOV of 0.955°, a WFS telescope magnification of 3X, a 15×15 array of distant objects, and a lenslet f/# of 19. The simulation uses these parameters primarily to define the line of sight from each lenslet to each object. The pupil size $\left(D_{pup}\right)$ and WFS magnification (M) are used with the number of lenslets across the array (n_{lens}) to determine lenslet pitch (w) as $w = \frac{D_{pup}}{M \cdot n_{lens}}$. Since each lenslet needs to image the entire array of objects, the separation of objects in the image space (h_0) is determined using the lenslet pitch and number of objects along one dimension of the object array $\left(n_{obj}\right)$ according to the equation $h_0 = \frac{w}{N_{obj}}$. This spacing is used to form an array of image points $\left(h_{x,y}(n,m)\right)$ where h_x and h_y are negative for $m < \frac{n_{obj}}{2}$ and $n > \frac{n_{obj}}{2}$ respectively. Once the image space position of each object is known, the object space line of sight is determined using the magnification, the image point separation, the lenslet pitch, and the lenslet f/# according to the equation

$$\theta_{x,y}(n,m) = \frac{1}{M} \cdot \tan^{-1}\left(\frac{h_{x,y}(n,m)}{w \cdot f/\#}\right). \qquad 3.5$$

The line of sight to each object is a key parameter of the simulation as this allows computation of the anisoplanatic phase that each object sees as its light passes through the multilayered atmosphere.

One key parameter that was changed in the simulation is the number and pitch of lenslets. The lenslet array was originally simulated to mirror the hardware implementation, but the decision was made to increase the number of lenslets from a 5×5 array to a 10×10 array of lenslets. Because the pupil size is not increased to accommodate the increase in lenslets, the lenslet pitch was reduced by a factor of two. The motivation for this was to increase the resolution of atmospheric sampling, increase the maximum sampled range, and to increase the averaging that is possible from a single frame through the WFS by incorporating more overlapping baseline pairs. This increase in averaging is important since dynamic behavior and the associated averaging that is possible are not being considered in this work. Table 3.4 summarizes the parameters used for much of the simulation work presented in this text. Other atmospheric configuration have been used to verify operation with results from only a small portion presented in Chapter 4:.

Table 3.4: Relevant parameters used in the WFS simulation

Description	Value	Origin
Phase screen pixel size	60 µm	Design Parameter (Interferometer resolution)
Number of layers	2	Design parameter
Exit pupil magnification	3	Design parameter (hardware)
Field of view width	0.955°	Design parameter (hardware)
Pupil size	11.25 mm	Design parameter (hardware)
Number of Layers	2	Design parameter
Phase screen Fried length (r_0)	~ 1.1 mm	Design parameter (hardware)
Layer 1 optical range	16.1 mm	Design parameter (hardware)
Layer 2 optical range	271.8 mm	Design parameter (hardware)
Number of lenslets	10×10	Design parameter
Lenslet f/#	19	Design parameter (hardware)
Number of field points	15×15	Design parameter (hardware)

3.2 Image Analysis

The primary purpose of the benchtop system is to explore the image analysis including the use of a leaky integrated science image as a reference for the determination of local tilts on small scales in all sub-images. Once demonstration of warp map computation in a hardware environment is complete, the remainder of the proof-of-concept occurs in the software simulation. The image processing includes the development of the reference image and the comparison of patches from the reference image to each of the sub-images.

3.2.1 Leaky Integration

The goal of the benchtop hardware is to demonstrate the ability to measure the local warping in the various sub-images. The first step in this process is to collect a reference image. This was done by creating a video sequence of a scene while moving each phase screen with a unique velocity. While this method showed reasonable success, future experiments would benefit from taking a sequence of still images with a fixed layer motion between each frame to eliminate any blurring due to image warping during an exposure. Using the series of images captured in the video sequence to create a leaky integrated image involves removing the relative tilt from each exposure. This mimics the function that a fast steering mirror would perform in a field operated system. To remove the tilt, the initial image captured by the camera image is used as a reference. As each successive image is captured, its overall shift is determined via a two-dimensional cross-correlation with the selected reference image. Each new frame is then shifted into a common position and combined into the running average with newer photographs receiving a higher weight factor than older images. Eventually enough frames are captured that the leaky integrator considers only the most recent images in its running average and discards older images. This allows a moving scene to be continually updated as new objects enter and leave the scene. Because each frame is warped slightly differently by the atmosphere, high spatial frequency information beyond λ/r_0 is lost from the image, but large-scale features remain to provide a reference against which sub-images can be compared. An example of an image that has undergone the leaky integration process is given in Figure 3.15.

Figure 3.15: An image of the author's family as seen by the science camera. The image on the left shows the scene prior to disturbance by atmospheric aberration. The image on the right is compiled from 100 frames taken through dynamic phase screens. There is also some residual defocus included in the right image due to the addition of the optically thick phase plates.

3.2.2 Benchtop Warp Map Computation

With the reference image compiled, the next step is to determine the warping that occurs in each sub-image. To begin the process of measuring local warping in all 25 of the sub images, the overall tilt of the sub-image array is removed and ignored. This once more follows the assumption that a fast steering mirror can be used to stabilize the system. To remove the tilt in software, a solid white scene was imaged through the lenslet array to provide a template which shows where each image should fall in a case with no aberration present. This template is shown in Figure 3.16. The sub-image array from the scene is compared to this template and shifted using a cross-correlation to determine best placement. With the image array nominally centered, each sub-image is analyzed independently by breaking the frame into 25 individual scenes as shown using red lines in Figure 3.17. Each sub-image is resized by a factor of 5 in both directions to have the same pixel count as the science image. Any additional magnification differences between the WFS and science arms must also be taken into account so that features in the scene can be compared between the two images.

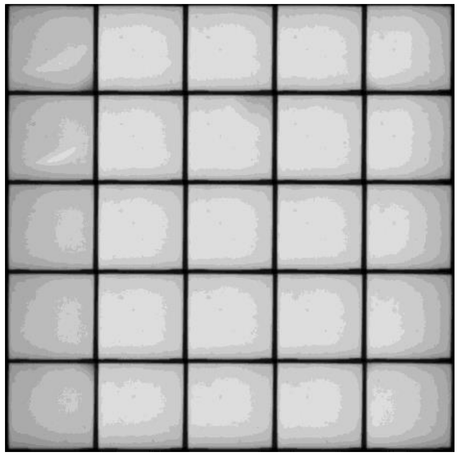

Figure 3.16: Image of a white scene observed through the lenslet array. This serves as the template image for tilt removal of the sub-images.

Figure 3.17: Example of a frame from the WFS lenslet arm. Each sub-image is separated and analyzed independently.

With the science and sub-images on the same scale, small patches of each can be compared to determine local warping. With the benchtop hardware designed with a total $\frac{FOV}{\theta_0}$ of 13.5, a value of $n_{obj} = 15$ is chosen and the scene is broken up into a 15×15 array of patches. The actual $\frac{FOV}{\theta_0}$ of 9.5 will be oversampled, but this does not pose a problem so long as there is sufficient spatial information in each patch. While one can simply break each image into 225 patches, performing the analysis iteratively allows large scale shifts to be removed before looking at fine scale shifts of smaller patches. The overall process is demonstrated in Figure 3.18 showing the various steps of image decomposition for comparisons. The process begins by removal of the overall tilt of the given sub-image which accounts for the shifting induced by the isoplanatic aberration. This shift is determined via a cross-correlation between each sub-image and the science image. The two-dimensional shift is removed to bring the images into better agreement and the inverse of the shift is saved as the bulk displacement of all patches in the current sub-image (s_1).

With the science and sub-images aligned, a further iteration of local tilt measurement and removal is accomplished by breaking both the sub-image and science image into relatively large patches for further comparison. As an example, the 15×15 array of patches can initially be broken into a 3×3 array before being further broken down into the desired scale. This allows alignment between many large-scale features in each patch. If for some reason a given region does not have enough spatial variation or contrast, the analysis does not return a slope for any of the patches in the given region. When comparing reference and sub-image patches, the reference image patch is oversized to accommodate correlation despite any potential large-scale local shifts in the sub-image patch. The two patches are compared via cross-correlation and the local shift is recorded

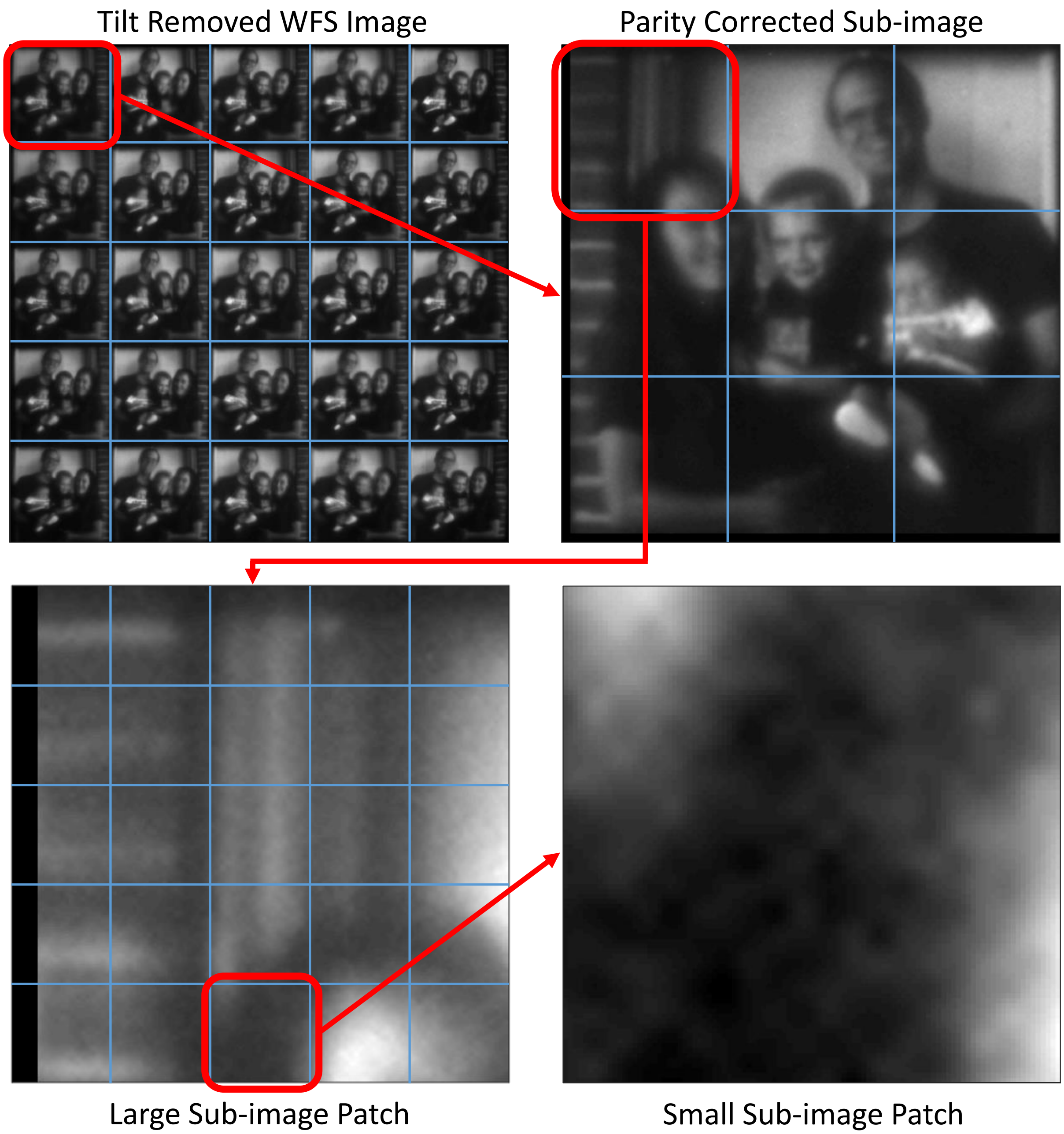

Figure 3.18: Sequence of image processing. At each stage the image shown is compared to a corresponding section of the science image to determine local displacements. Measured tilts are removed before moving to the next stage of image decomposition and comparison. The final local tilt for a small sub-image patch is the addition of the shifts calculated at the lenslet, large sub-image patch, and small sub-image patch levels.

(s_2) and removed. The processes is repeated by further breaking down each of the larger patches (3×3 array) into smaller patches (5×5 array per large patch). The same process is followed and the shifts are once more recorded (s_3) at this smaller level.

The total tilt for each small patch is computed by summing the tilt contribution from the tilt of the small patches, the tilt of the corresponding larger patches, and the tilt of the sub-image ($s_{tot} = s_1 + s_2 + s_3$). This method is repeated for each sub-image and the results are combined into a warp map which contains an x- and y-slope related to each patch in the sub-image array. While the iterative approach does add some small computational complexity, this method increases the robustness of the algorithm. The benefit of the iterative solution is a higher probability of success in correlating patches on the smallest scales because large shifts in the small patches are already accounted for at a higher level. In general, if the number of isoplanatic patches across a scene is not a prime number, the analysis can benefit from an iterative solution by first breaking the image into large patches before further sub-dividing to the desired scale.

While the method is fairly straightforward, there are some challenges that can arise in the processing. As mentioned above, regions of the image with little or no diversity cannot be used to determine local warping. The problem here is self-solving as regions with little spatial information do not contain features that can benefit from local tilt removal. Another problem is that of built-in optical aberration. A complication specifically related to a benchtop setup is the potential for shifting of the image position due to insertion of optically thick phase screens after the initial alignment. Other static aberrations such as distortion can adversely affect the overall tilt computation due to warping from a scene which is unrelated to the atmospheric turbulence. This only becomes a problem in the attempt to reconstruct the synthetic atmosphere and compare against measured phase plates. With static aberration in the system, the aberration will be attributed to the phase layers which will compare poorly with their physical counterparts.

The final point of interest is the image comparison algorithm. The quickest method utilizes cross-correlations, but initial comparisons showed better results using a raster scan and choosing shift locations with the smallest rms difference. To compute the rms difference, the sub-image patch is compared against a region of the oversized reference image patch. The images are first scaled such that the dynamic range is identical. The mean is then subtracted so that the largest rms differences will come from both the brightest and darkest regions of the image. An the rms difference is taken and then the image is shifted by a pixel and the process is repeated. As an example, Figure 3.19 shows one of the sub-images along with a large patch of the sub-image used

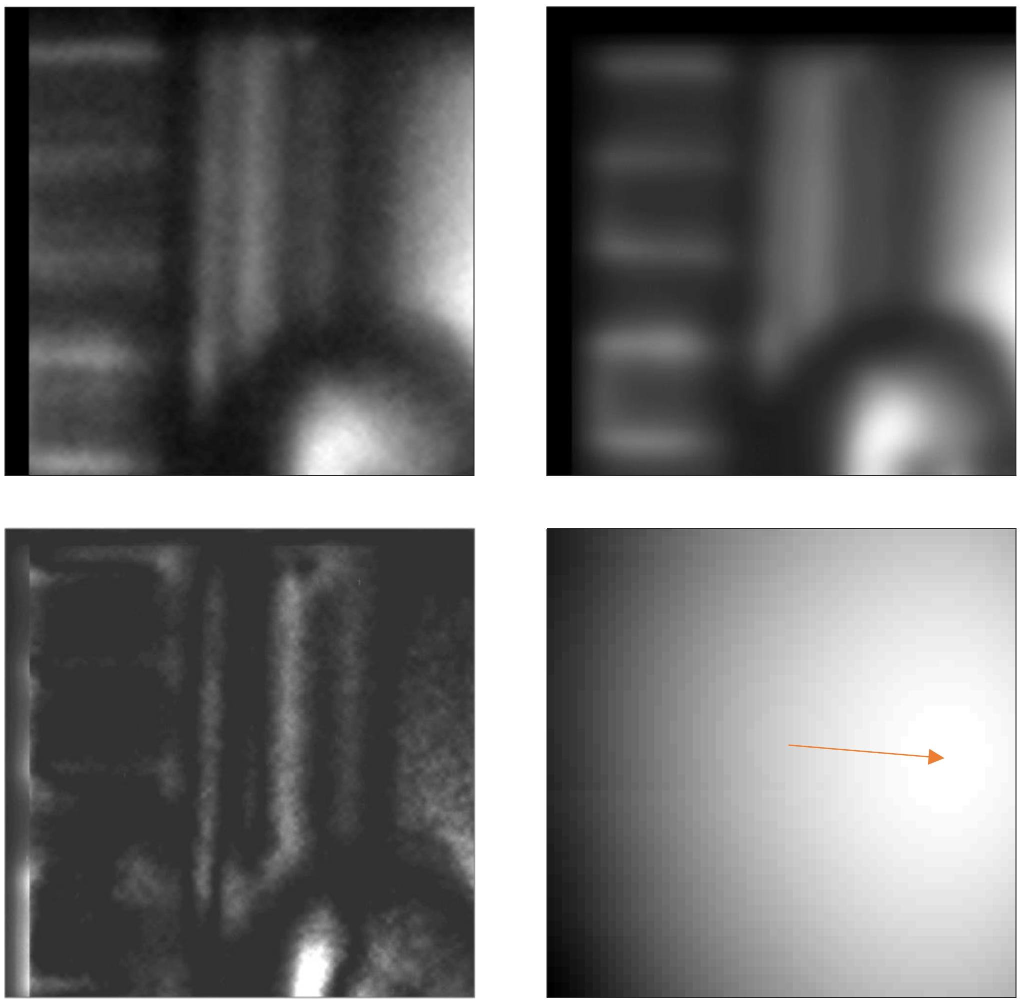

Figure 3.19: Example of the shift computation for a large sub-image patch. Top-left shows the large sub-image patch while the top-right image shows the corresponding oversized reference image patch. The bottom-left image shows the rms difference between the patches for no shift, and the bottom-right image is the rms difference as a function of image shift with the approximate shift vector shown in red.

to determine large scale shifts. Also shown is the oversized patch from the reference image and the two-dimensional map of rms difference as a function of image shift.

3.3 Layer Generation

The synthetic layers were generated in Matlab using Roddier's method from his publication "The Effects of Atmospheric Turbulence in Optical Astronomy" (1981). To overcome the underrepresentation of low frequency terms, each phase screen is generated at twice the requested size with the returned section cropped out of the larger phase screen. Explicit tilts can also be added as extra compensation, but the WFS simulation initially removes overall tilt to mimic the operation of a fast steering mirror. The screen is created by generating an array of random numbers from 0 to 2π. Each array element is used in the exponent of a complex exponential function with the amplitude scaled according to the power law in the Kolmogorov power spectrum ($k^{-11/3}$). This represents the phase screen in the Fourier domain. Taking the real and imaginary parts from the two-dimensional Fourier transform yields two fully independent phase representations of Kolmogorov turbulence.

To maintain consistency between simulation runs a library of four screens were used for most experiments, although the simulation also supports randomly generated screens. This small library allows for two separate two-layered atmospheres to be analyzed side-by-side. The simulation was also successfully performed with multiple distant layers to ensure to that atmospheres composed of three or more discreet layers were properly analyzed. The simulation can fully support an arbitrary number of layers, but many of the results given in Chapter 4: will focus on the two dual-layered atmospheres for the final proof of concept.

3.4 Warp Map Computation

The first task of the simulation related to the proof of concept of the wavefront sensor is the computation of the warp maps. The warp map for a given atmosphere is computed one layer at a time. Each layer is processed independently to determine the gradient along each line of sight. Once all layers have been processed in the same way, the total gradient along each line of sight is computed by summing the gradients from each of the layers. While each layer will perturb the line of sight slightly during actual operation, the relatively small effect is ignored in this simulation. This provides a reasonable first-order estimate of the total gradient induced by the given atmosphere.

Computation of the warp map for a given layer uses knowledge of the layer location relative to the WFS entrance pupil to determine the phase disturbance along each line of sight. Figure 3.20 shows a graphical depiction of the sampling of two phase screens at different ranges for a given line of sight from the entrance pupil. Determination of the angle for each line of sight is addressed mathematically using Equation 3.5 with corresponding details in the same paragraph of Section 3.1.2. The center of each line of sight is calculated on the phase screen using

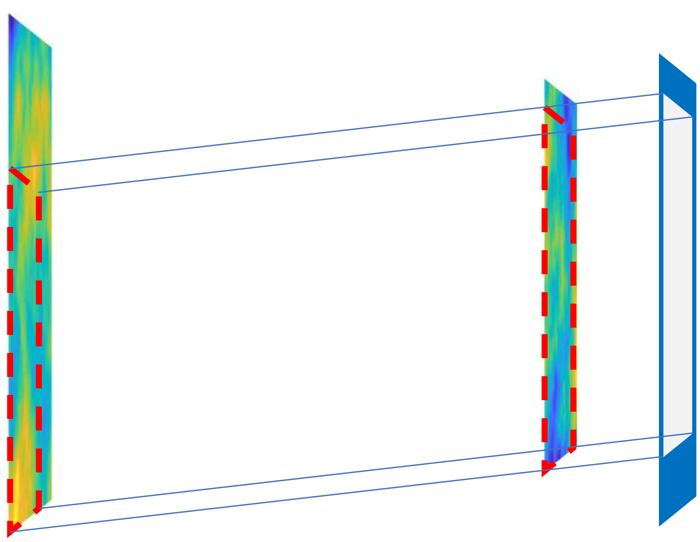

Figure 3.20: Graphical depiction of the phase accumulated along a single line of sight through a two-layer atmosphere.

$H_{x,y}(n,m) = d \cdot \tan\big(\theta_{x.y}(n,m)\big)$ where d is the distance from the entrance pupil to the phase screen. A pupil sized region of the phase screen centered on $(H_x(n,m), H_y(n,m))$ is identified as the phase disturbance along the line of sight for the given layer.

With the line-of-sight disturbance identified, tilt contributions are found for each lenslet in the array. The portion of the phase screen seen along the line of sight is broken into $n_{lens} \times n_{lens}$ pieces corresponding to the lenslet array. Each piece is fit with a plane and the x- and y-slope of the plane becomes the local tilt for the given lenslet along the given line of sight. This process is repeated for all lenslets in the array yielding the local warping seen from a single object patch in the scene. Repeating this for all lines of sight builds a complete warp map for a single layer. This process is repeated for all layers in the atmosphere. Upon completion of the final layer, the warp maps are summed together to get the final warp map for the current atmosphere.

The process outlined works well and computes the warp map quickly but is a simplification of the physical processes in imaging through a real atmosphere. A physical optics model was generated as a cross-check to the geometric model outlined above. The determination of phase aberration along a line of sight remained identical, but for the cross-check, the phase contribution of all layers along a line of sight was summed to estimate the total disturbance. This atmospheric aberration was again broken into pieces corresponding to lenslets in the pupil, but instead of computing local tilts based on planar fits to the phase, the PSF for each lenslet was computed and compared to the PSF formed by a collimated beam. The displacement of the PSF was used to measure the atmospheric tilt across the lenslet as is common in traditional Shark-Hartmann wavefront sensors. This general process is shown graphically in Figure 3.21. The warp maps resulting from the PSF method were compared to the summation of each layer's planar fit warp map and found to be in good agreement. This was done to verify both the use of the less

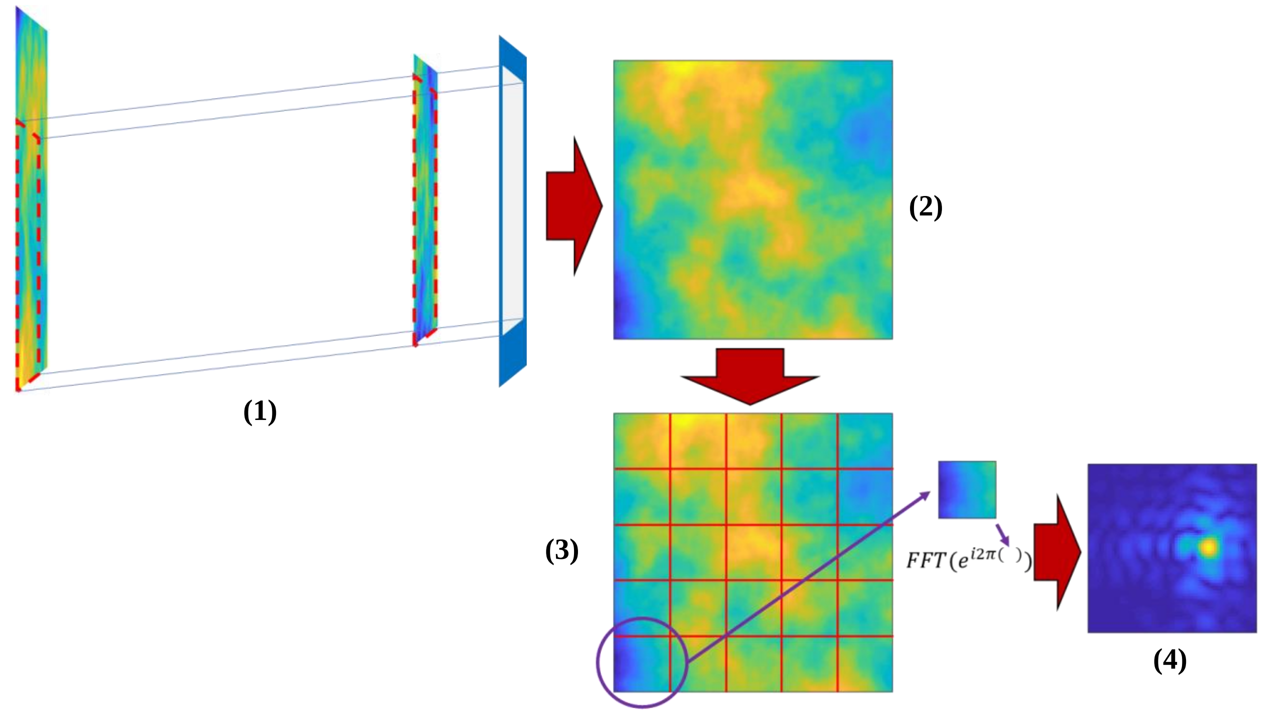

Figure 3.21: Graphical depiction of the processing performed in the benchtop simulation. Stage (1) uses the line of sight to select the relevant portions of all phase screens in the atmosphere. Stage (2) sums the contribution from each layer and Stage (3) breaks the corresponding phase into portions sampled by each lens in the lenslet array. Finally, Stage (4) computes the resulting PSF from each lens whose displacement is used to determine the local phase gradient.

computationally intensive approach using planar fits and the justification to analyze each layer independently rather than as a combined atmosphere.

The final consideration to discuss when developing warp maps is the sorting of the slope vectors. When creating a warp map from either simulation or data from the wavefront sensor, the data is transformed into a one-dimensional slope vector as described in Section 2.4.1. The sorting method used is not so important as the consistency of use. The same sorting regime must be used when creating the slope vector, the response matrix, and when interpreting the results of the atmospheric reconstruction. The sorting method used in the current simulation is to create two column vectors with one containing x-slope information and the other comprised of the y-slopes. To sort the x- and y-slopes, the data points were collected from the top-left portion of the image with the data points sequenced first down columns then across rows as shown in Figure 3.22. Using

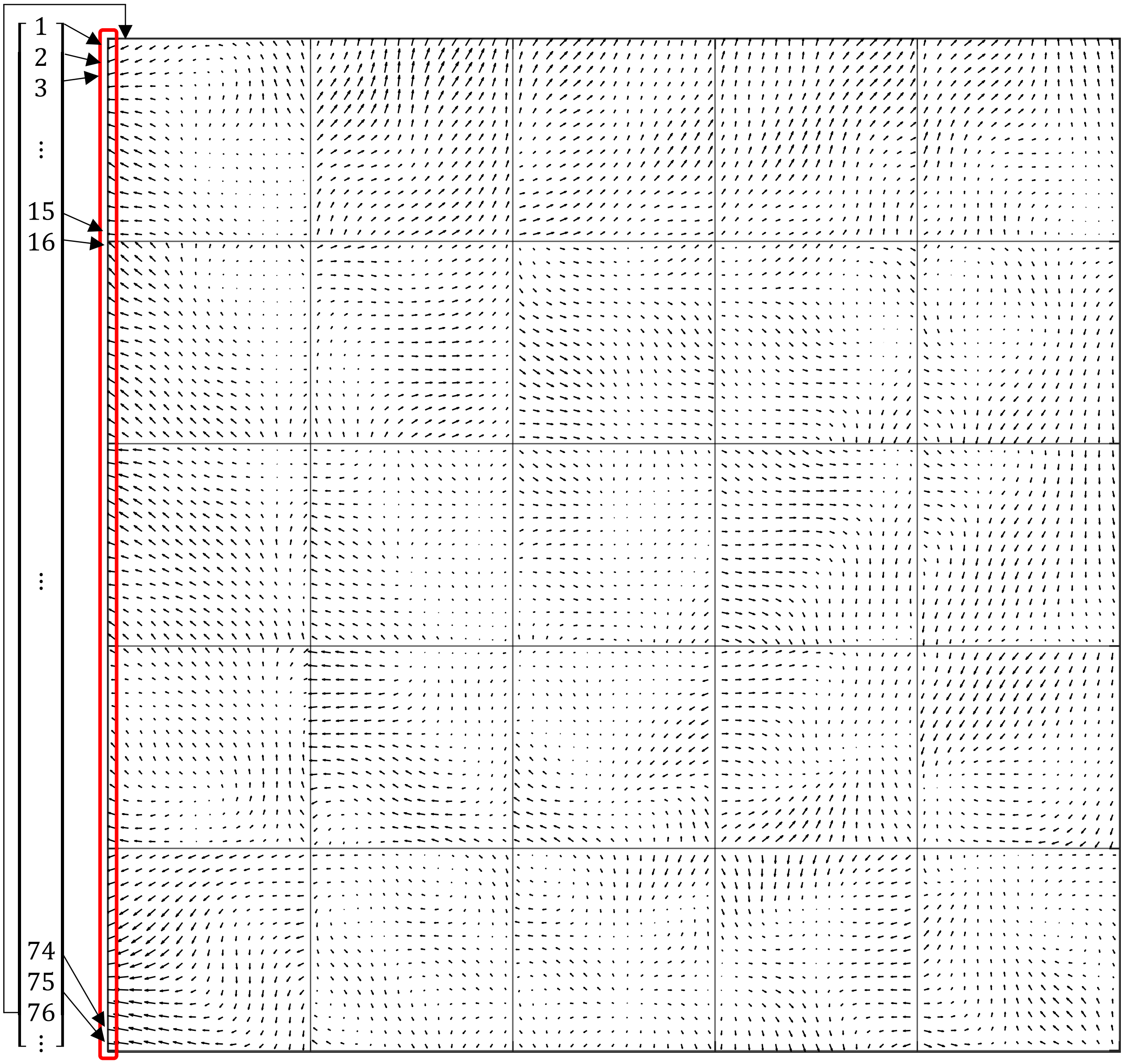

Figure 3.22: Example of sorting method used in the WFS simulation. A simulated warp map from a 5×5 lenslet array is shown for graphical simplicity despite the simulation utilizing a 10×10 array of lenslets.

this scheme provided a consistent way to sort the data between warp maps and slope vectors. Once the x- and y-slope vectors were developed the two were concatenated into a single column vector that describes the entire warp map.

3.5 SLODAR Implementation

Validation of the WFS methodology, and the simulation in general, hinges on the SLODAR algorithm described in Section 2.3.1 to determine the distribution of aberration strength along the line of sight. While knowledge of layer ranges was necessary to compute the warp maps, the remainder of the simulation makes no assumptions about the atmosphere from which the warp maps were generated. The analysis relies solely on knowledge of the hardware-based parameters which were used in the atmospheric measurement. This lack of knowledge extends to layer strengths, ranges, and the number of layers present in the atmosphere under analysis. Comparison between the simulation outputs and the known layer inputs provides the validation of the methodology and of the numerical implementation.

The implementation of the SLODAR algorithm can be broken up into three main parts:

1. Normalization Matrices
2. Warp Map Correlations
3. Atmospheric Profiling

The normalization matrices account for redundancy in many of the atmospheric measurements and convert the sums produced in the warp map correlations into averages. The warp map correlations comprise the bulk of the analysis and generate the information used to determine the aberration distribution. The atmospheric profiling section describes how information is extracted and organized from the correlation data. Each of these topics is discussed in detail in the sections below.

3.5.1 Normalization Matrices

The first thing that the SLODAR algorithm does is create the normalization matrices defined in Section 2.3.1.2 as $O(\delta i, \delta j)$ and $M(\delta n, \delta m)$. The first matrix, $O(\delta i, \delta j)$, accounts for the number of overlapping lenslet baseline pairs which occur from a given warp map cross-correlation as described in Section 3.5.2. Computation of the lenslet normalization matrix begins by creating a matrix of ones the size of the lenslet array. After zero-padding the matrix, the autocorrelation yields the normalization matrix $O(\delta i, \delta j)$. Each entry in this matrix describes the number of overlapping lenslet pairs created by comparing warp maps from two objects for a lenslet separation of δi in the x-direction and δj in the y-direction. Note that δi and δj are integer values from $-(n_{lens} - 1)$ to $+(n_{lens} - 1)$.

The normalization matrix for overlapping object baselines, $M(\delta n, \delta m)$, is created by multiplying entries from two number lines where one number line represents the column and the other represents the row. Each number line runs from n_{obj} down to 1 in integer values and each matrix entry is created by multiplying the number associated with the column by the number associated with the row. Any entries where neither the row nor column correspond to n_{obj} are multiplied by an additional factor of two. This factor accounts for a parity difference if either δm or δn are negative. This parity difference does not exist in the first row or column as comparison between adjacent objects can be accomplished in either direction. A graphical example of the parity for different object separations is given in Figure 3.23 where baseline pairs are connected in a 3×3 object array. Note that for the first entry, each object is compared with its neighbor and comparisons along $\langle 1,0 \rangle$ are identical to comparisons along $\langle -1,0 \rangle$. A complete object normalization matrix is shown graphically for n_{obj}=15 in Figure 3.24. In this figure the number

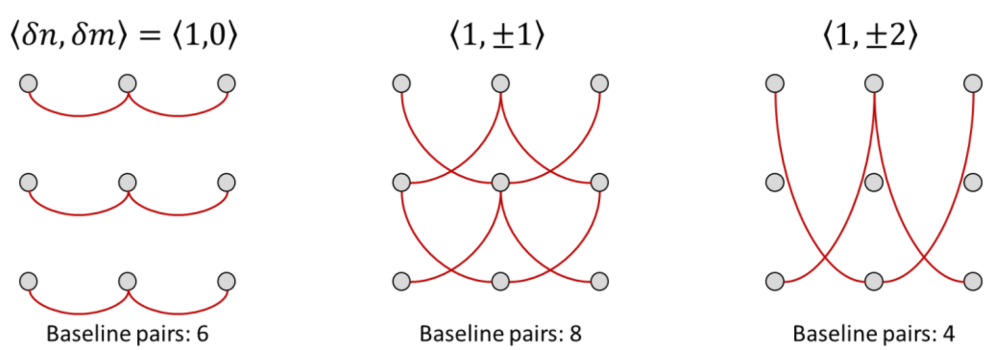

Figure 3.23: Graphical depiction of baseline pairs of objects for $\delta n = 1$ and $\delta m = 0, \pm 1, \pm 2$. Since SLODAR only cares about the total separation, all baseline pairs for a given case correspond to the same range and are averaged together.

Number lines		15	14	13	12	11	10	9	8	7	6	5	4	3	2	1
	$\delta m \backslash \delta n$	0	1	2	3	4	5	6	7	8	9	10	11	12	13	14
15	0	225	210	195	180	165	150	135	120	105	90	75	60	45	30	15
14	1	210	392	364	336	308	280	252	224	196	168	140	112	84	56	28
13	2	195	364	338	312	286	260	234	208	182	156	130	104	78	52	26
12	3	180	336	312	288	264	240	216	192	168	144	120	96	72	48	24
11	4	165	308	286	264	242	220	198	176	154	132	110	88	66	44	22
10	5	150	280	260	240	220	200	180	160	140	120	100	80	60	40	20
9	6	135	252	234	216	198	180	162	144	126	108	90	72	54	36	18
8	7	120	224	208	192	176	160	144	128	112	96	80	64	48	32	16
7	8	105	196	182	168	154	140	126	112	98	84	70	56	42	28	14
6	9	90	168	156	144	132	120	108	96	84	72	60	48	36	24	12
5	10	75	140	130	120	110	100	90	80	70	60	50	40	30	20	10
4	11	60	112	104	96	88	80	72	64	56	48	40	32	24	16	8
3	12	45	84	78	72	66	60	54	48	42	36	30	24	18	12	6
2	13	30	56	52	48	44	40	36	32	28	24	20	16	12	8	4
1	14	15	28	26	24	22	20	18	16	14	12	10	8	6	4	2

Figure 3.24: Graphical representation of the normalization matrix for the separation of object pairs.

lines used to generate the data are shown in dark gray, the relative shift between the objects is shown in light gray, and the data is shown colored relative to the number of overlapping baseline pairs.

Breaking the scene into an evenly spaced grid of object points allows for relatively large values of n_{obj} and n_{lens} leads to many redundant baseline pairs in both spaces. The normalization matrices tell exactly how many redundant pairs are expected for any given lenslet and object separation. Dividing any given slope correlation by the relevant entry in both the lenslet and object normalization matrices enables averaging when combining slope correlations which correspond to a common range.

3.5.2 Warp Map Correlations

The second major process in the SLODAR algorithm begins by reformatting the atmosphere's slope vector into an x-warp map and a y-warp map for each object point in the scene. This creates $2 \cdot n_{obj}^2$ arrays each of size $n_{lens} \times n_{lens}$. To implement the SLODAR technique, each slope corresponding to an object is multiplied by every other slope for every other object. This can be a daunting amount of data to keep track of, but the methodology is simplified using cross-correlations between the object specific warp maps. The correlations are tracked using a systematic approach to ensure that all slopes are compared with the results organized to enable easy retrieval of the relevant information. While the algorithms are platform independent, the terminology and methodology used in this work correspond to implementation in the Matlab programming environment.

Prior to implementation of the cross-correlations, two $n_{obj} \times n_{obj}$ cell arrays are created where each cell is pre-allocated with a $(2 \cdot n_{lens} - 1) \times (2 \cdot n_{lens} - 1)$ matrix for storing warp map cross-correlations. The two variables that are tracked in these arrays are (1) the slope correlations and (2) the corresponding ranges. Each cell corresponds to an object space separation, $(\delta n, \delta m)$, where δn and δm range from 0 to $n_{obj} - 1$. The cell (0, 0) contains the mean of the autocorrelations. Each other cells represent the mean of cross-correlations between warp maps corresponding to objects separated by an integer multiple of θ_{obj} in x and y. As an example, the cell (3,12) contains the average of cross-correlations obtained from each pair of objects separated by $3 \cdot \theta_{obj}$ in the x direction $(\delta n = 3)$ and $12 \cdot \theta_{obj}$ in the y direction $(\delta m = 12)$. The range matrix behaves similarly, but instead of averaging, each matrix is computed once for the given object separations.

In traditional SLODAR, the autocorrelation is used to characterize the impulse response since its range corresponds to a layer infinitely far away. The autocorrelation is typically used to deconvolve the results of the cross-correlations but results from this limited simulation showed a large degradation once the deconvolution was incorporated. Implementation of the deconvolution of the autocorrelation increased the noise in the atmospheric profile such that the ranges to turbulent layers were not recoverable. This occurred in spite of Tikhonov regularization which attempted to minimize the deconvolution noise (Tikhonov & Glasko 1965). Perhaps the autocorrelation could be implemented using additional averaging in the time domain, but successful results were obtained without the need of such deconvolution.

The correlations calculations are performed by starting with the warp map from a single object and comparing it against all others using cross-correlations. Prior to computation of the cross-correlation, each of the x- and y-warp map matrices are zero-padded on all sides by the value n_{lens} to allow for comparisons out to the opposite corners of the lenslet array. Comparing each of the warp maps results in $\frac{n_{obj}^2\left(n_{obj}^2-1\right)}{2}$ matrices, several of which probe identical altitudes. To condense the results, the normalized matrices are summed into lens cells based on relative object separation. To facilitate this, each object is assigned an x- and y-position with an arbitrary origin location. The object separation for a given cross-correlation, $(\delta n = |x_1 - x_2|, \delta m = |y_1 - y_2|)$, is tracked and used to determine the ranges probed, the storage location in the correlation cell array, and the normalization applied. The results of each cross-correlation are normalized by both the lenslet and object normalization matrices described in Section 3.5.1. The lenslet normalization is applied using an element-by-element division between the resulting correlation matrix and the normalization matrix. The object normalization is a scalar division applied based on the separation of the object pair $(\delta n, \delta m)$ as shown in Figure 3.24.

The ranging cell array is developed based on Equation 2.8. Each of the cells in the array corresponds to an object separation, $(\delta n, \delta m)$, with a sorting identical to the correlation matrix. Each cell contains a matrix which yields the height as a function of lenslet separation, $(\delta i, \delta j)$, where δi and δj are the integer number of x- and y-matrix elements from the center of the array. An example of such a matrix is given in Figure 3.25 for a 5×5 lenslet array with an object separation of $\theta = 1°$ and a lenslet pitch of $w = 1\ mm$. Note that negative ranges are non-physical and are ignored as outlined in Section 3.5.3. This combination of elements results in a minimum sampled range of $h_{min} = \frac{w}{\theta} = 57\ mm$ and a maximum range of $h_{max} = \frac{w(n_{lens}-1)\sqrt{2}}{\theta} = 324\ mm$ for the given object angular separation according to Equation 2.9 and Equation 2.10 respectively.

3.5.3 Atmospheric Profiling

The SLODAR theory for a single baseline pair as outlined by Wilson (2002) points out that the correlations only yield useful information in the direction of object separation. Correlations

324	286	256	236	229	-236	-256	-286	-324
286	243	207	181	172	-181	-207	-243	-286
256	207	162	128	115	-128	-162	-207	-256
236	181	128	81	57	-81	-128	-181	-236
229	172	115	57	0	-57	-115	-172	-229
236	181	128	81	-57	-81	-128	-181	-236
256	207	162	128	-115	-128	-162	-207	-256
286	243	207	181	-172	-181	-207	-243	-286
324	286	256	236	-229	-236	-256	-286	-324

Figure 3.25: Example of a ranging matrix for a 5×5 lenslet array with $\theta = 1°$ and $d_{lens} = 1\ mm$

outside of this plane do not allow intersections between lines of sight through the atmosphere. To extract both the correlation and ranging information for each object pair, the angle of the object separation vector is used to determine a cross-section through the corresponding correlation matrix. A similar cross-section is taken from the ranging matrix so that every slope correlation is matched with a corresponding range. Once the appropriate cross-section has been identified, the values nearest the cross-section are arranged into a vector. One example of such a cross-section is shown in Figure 3.26 where the red line represents the cross section used to select the relevant data. Once the values from all matrix cross-sections are extracted, each value is sorted according to its corresponding range. Negative ranges are removed, and a boxcar average is implemented with an adjustable width as a way to smooth the data. Negative correlation values are also set to

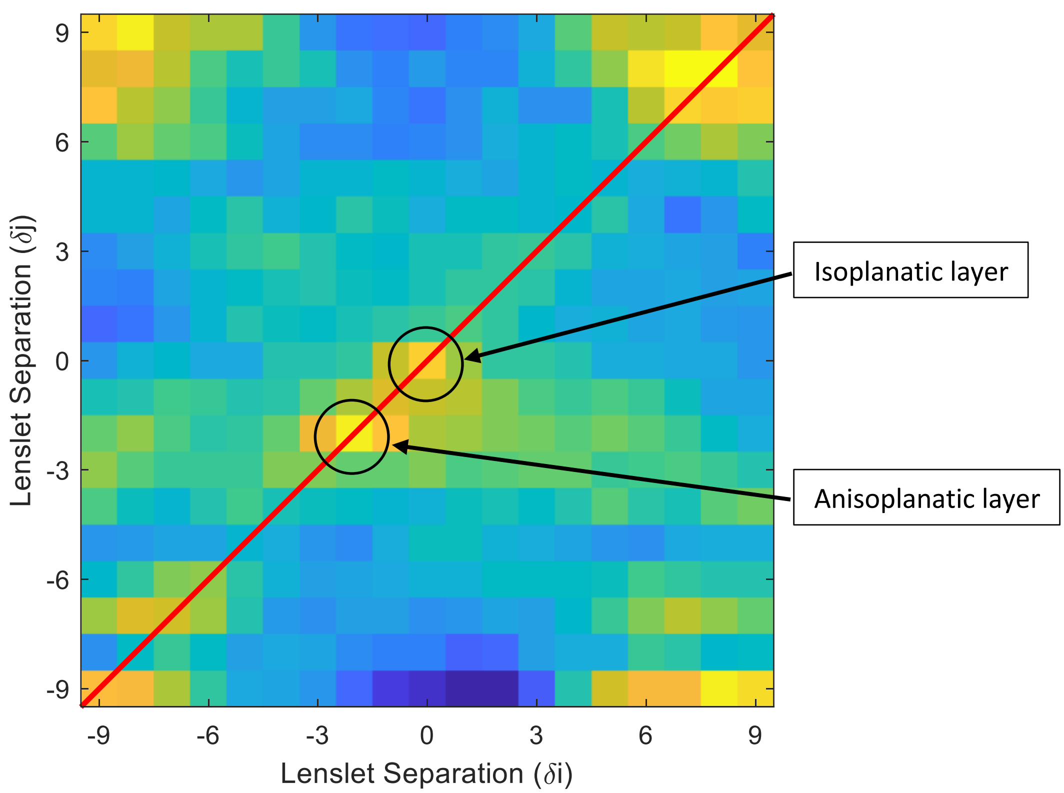

Figure 3.26: Example of a correlation matrix computed from the cross-correlation of warp maps from two different objects. The red line represents the direction of object separation. The two layers used to generate the warp maps appear as bright points along the direction of separation.

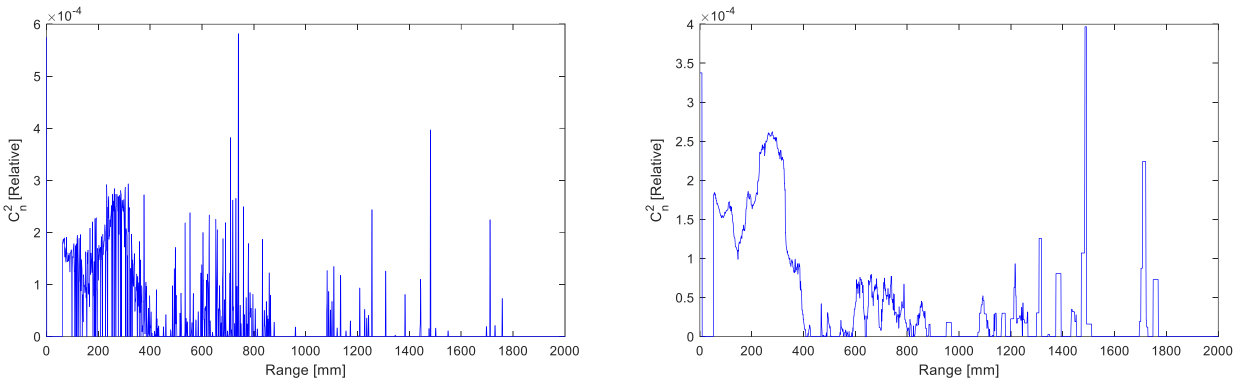

Figure 3.27: Recovered C_n^2 profiles from SLODAR analysis of a 2-layered atmosphere with turbulence phase screens at 16.1 mm and 271.8 mm. The figure on the left shows the raw results while the figure on the right shows a 19 mm wide boxcar average.

zero after the boxcar average is applied. The resulting profile is the SLODAR estimation of the atmospheric turbulence as a function of distance from the entrance pupil. An example of such a profile is shown in Figure 3.27.

3.6 CLEAN Implementation

There are many possible methods to extract layer ranges from the turbulence profile achieved through the SLODAR algorithm. The overall goal is to identify peaks in the data which correspond to layers of significant turbulence. The method used in this simulation is a variation on the CLEAN algorithm as described in Section 2.3.4. Through experimentation, the Lorentzian function described in Equation 2.15 proved to be a reasonable fit for the layer response functions of layers with a range greater than h_{min}. Altitude dependency was explored with results shown in Figure 3.28 and the fit variables are summarized in Table 3.5 for independent layers inserted every 100 mm. The Lorentzian fits perform well at all ranges, but consistently underestimate the amplitude of the ground layer. To overcome this limitation, the strength of the ground layer is taken from the SLODAR output value at a range of zero rather than the peak value of the Lorentzian fit. There is some mild variation in the width and relative strength as a function of range, although the location of the peak is consistently overestimated by approximately 5%. The

Table 3.5: CLEAN algorithm Lorentzian fit parameters for various ranges. Starting points for fit: $a = 0; b = 70; c = location\ of\ local\ maxima; d = value\ of\ local\ maxima$

Input Range [mm]	Range Estimate (a) [mm]	Lorentzian Width (b) [mm]	Relative Layer Strength (c)	Background Offset (d)	$\frac{Range\ Estimate}{Input\ Range}$
0	0.0	100.00	0.679	0.076	0.000
100	105.0	72.97	0.913	0.054	1.050
200	209.3	76.79	0.917	0.092	1.047
300	310.4	65.47	0.927	0.137	1.035
400	414.7	78.90	0.856	0.130	1.037
500	523.0	67.35	0.837	0.111	1.046
600	626.8	73.42	0.819	0.130	1.045
700	732.6	82.25	0.829	0.076	1.047
800	838.1	93.36	0.838	0.072	1.048
900	953.2	100.00	0.976	0.100	1.059
1000	1046.3	100.00	1.056	0.063	1.046

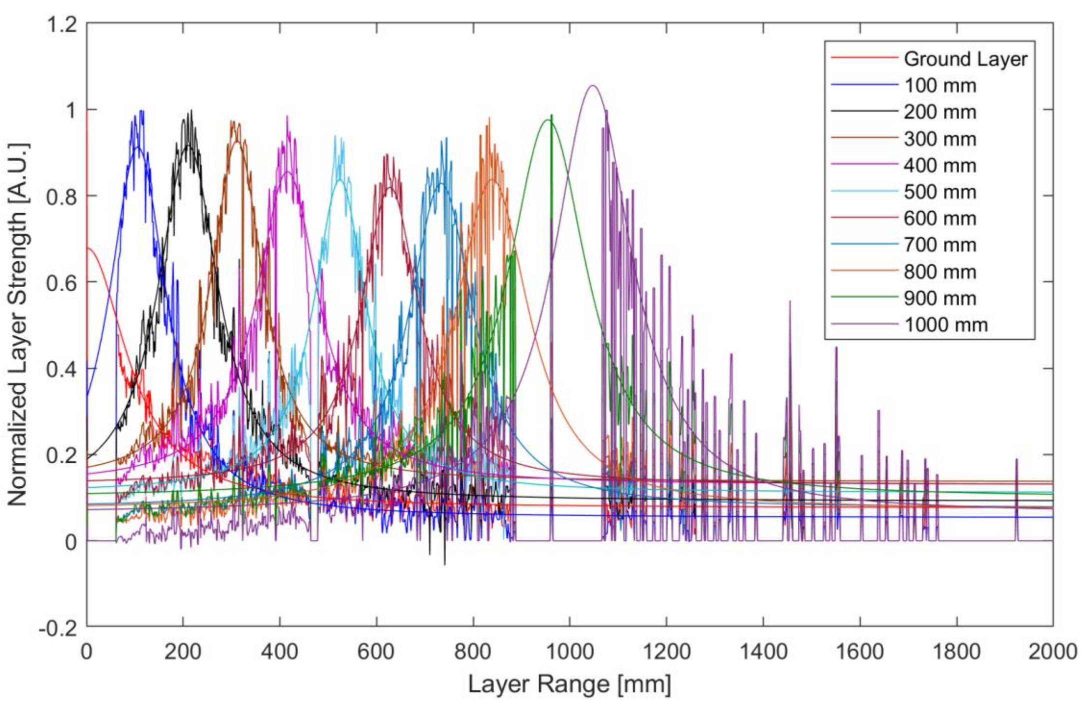

Figure 3.28: Layer dependent calibration functions from 0 mm to 1000 mm. A single layer was analyzed at a time and the profiles from 35 random variations were averaged together to achieve the results in this plot. Associated fit parameters are found in Table 3.5.

overestimate in the range prediction is implemented as a calibration factor in the resulting layer range estimates. The calibration functions are different enough that a generic fit is used rather than imposing a strict adherence to a Lorentzian shape with a fixed amplitude and width.

To locate significant layers, a peak finding algorithm is implemented to find the largest peak in the data. A threshold on further peaks that can be identified as significant layers is set at 50% of this maximum value. The algorithm first addresses the ground layer by comparing the C_n^2 estimate at 0 mm to the threshold. If the peak is large enough, then the peak value is recorded, and a Lorentzian function is fit to the first 150 mm of data with the peak forced to be at 0 mm. This fit is removed from the dataset. With the ground layer removed, the algorithm now iteratively searches for the highest peak, fits the peak using all data within 50 mm to Equation 2.15, records the peak location (c), and subtracts the fit function from the data. This is repeated until no data points are larger than the defined threshold. Any fits with too narrow or too broad of a Lorentzian width are discarded from the list of potential layers. These fits are still iteratively removed so that other layers can continue to be identified, but no reconstruction of the turbulent layer occurs. The fit region is limited to data within 50 mm of the peak so that the fit is not influenced by other layers

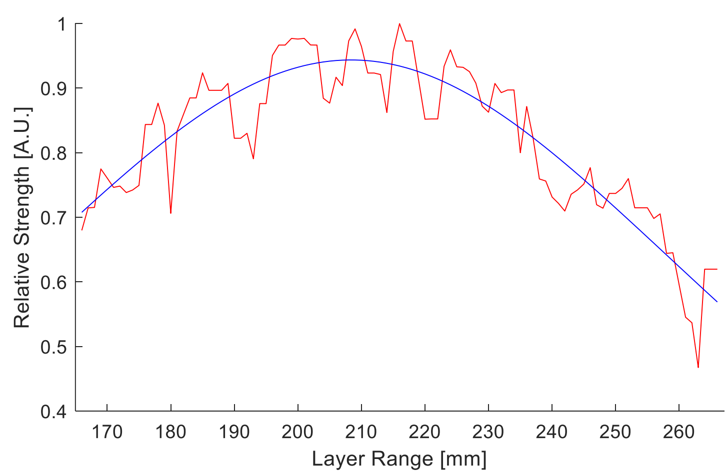

Figure 3.29: Example of a Lorentzian fit to the local maxima of 35 averaged profiles with a single layer at 200 mm.

distant from the peak being analyzed. An example of the local fit for the 200 mm calibration function is shown in Figure 3.29.

3.7 Response Matrix Generation

Once the approximate ranges to significant turbulence layers are known, a custom response matrix can be built for the current atmosphere. In practical applications where the hardware may be calibrated prior to flight, one option would be to store a library of response matrices for some finite number of ranges. The appropriate ranges can be recalled from system memory once the need is understood. Alternatively, such a library can be created on-the-fly by generating a simulated response matrix for each layer identified through the CLEAN algorithm.

Generation of a response matrix for a single layer involves simulation and analysis of many phase screens. Because the atmospheric sampling is poor at ranges well below h_{max}, a threshold can be implemented based on the ranges that can be viably reconstructed given the hardware limitations. For this proof-of-concept simulation, all layers able to be represented by a 1024×1024 matrix are allowed which limits the possible layer ranges to 3032 mm. Layers beyond this range are ignored. To measure the WFS response, a library of 502 Kolmogorov phase screens including tip and tilt was created to maintain consistency between calibration events and to maintain knowledge of the input modes. For each layer identified by the CLEAN algorithm, each of the 502 modes is simulated at each output range to generate 502 warp maps for each layer. These are sorted in an identical manner to the slope vector as described in Section 3.4. Assembling each of the 502 slope vectors into columns creates the response matrix as shown in Equation 2.17. The responses matrices from multiple layers are concatenated as represented in Equation 2.18 such that the number of columns in the final response matrix for the measured atmosphere is $(number\ of\ layers) \cdot 502$.

While this simulation uses Kolmogorov phase screens as the basis set for reconstruction, other basis sets are equally viable. As an example, for a circular geometry the Zernike polynomials create a complete orthogonal set. Similarly, Fourier modes may be used for applications with a square pupil. This was attempted in early calibration attempts on the physical hardware, but the Kolmogorov set showed better reconstruction in early experiments. One of the benefits of Kolmogorov phase screens is that each screen has a wide range of spatial frequency content that follows the same scaling as the atmosphere. This is by no means an orthogonal or complete set, but the singular value decomposition (SVD) described in Section 2.4.2 does create an orthogonal set out of linear combinations of the input modes. With enough randomly generated Kolmogorov modes, the simulation can successfully reconstruct randomly generated screens outside of the basis set. If the application is expected to observe turbulence which follows a different power law, it would be equally viable to develop a basis set of random screens following the anticipated scaling laws.

3.8 Layer Reconstruction

Using the mathematical foundation in Section 2.4.2, the atmospheric response matrix, $\boldsymbol{R}$, is converted into a reconstruction matrix, $\boldsymbol{R^{-1}}$. The reconstruction matrix is the pseudoinverse, or the Moore-Penrose inverse, of the response matrix and is computed using a singular value decomposition (SVD) as outlined in Equation 2.21 (Moore 1920; Penrose 1955). Prior to inverting the singular value matrix, $\boldsymbol{\Sigma}$, a condition number is applied to eliminate contributions from modes below a set threshold. The threshold is set by dividing the largest singular value by the condition number and setting all singular values below the resulting threshold to zero. The proper condition number must be determined based on the system definition and the number and type of modes used in the influence matrix. An example of such singular values along with the threshold for a

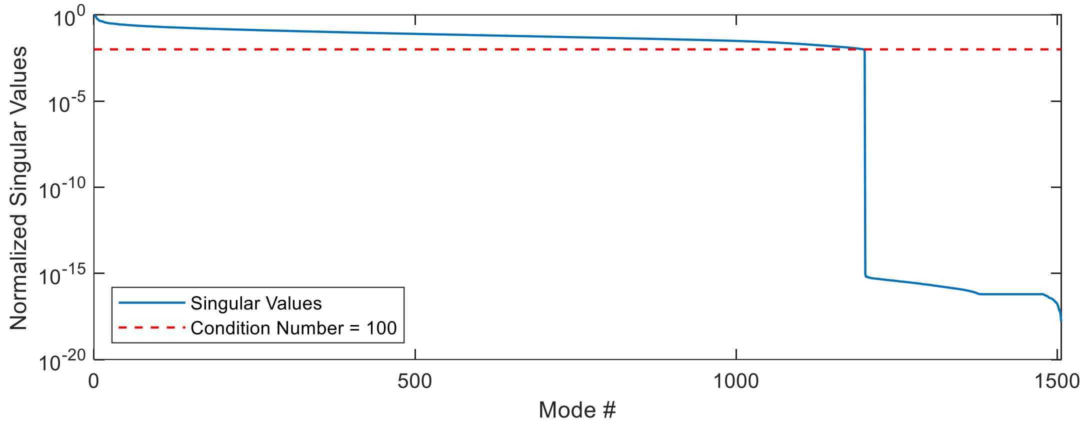

Figure 3.30: Singular values with a threshold set using a condition number of 100.

condition number of 100 are shown in Figure 3.30. Typically, a knee in the curve is used to decide where the condition number is set. With the basis sets used in this example, the condition number is set slightly above the knee to rule out additional modes that may prove problematic. Figure 3.31 shows the effects of decreasing condition number on the reconstruction of a phase screen from a two-layered atmosphere. The reconstruction with no conditioning is dominated by null modes and is appears in the reconstruction as high frequency noise. As the condition number is lowered and fewer modes are allowed in the reconstruction, the general trend seen is that high frequency detail is removed similar to the effect of a low pass filter on the phase screen. As seen in the bottom-left and bottom-right images in Figure 3.31, just removing the null modes does not guarantee the best reconstruction, but removal of additional modes can significantly improve the reconstructed phase screen. Once properly conditioned, the reconstruction matrix is formed using Equation 2.22.

Multiplying the slope vector, S, obtained from measurement of the atmosphere by the reconstruction matrix, $\boldsymbol{R^{-1}}$, yields a vector which describes the relative contribution of each mode to each layer, Φ. Using this vector and the knowledge of the modes input into the response matrix, the atmosphere is reconstructed by applying the appropriate weighting to each mode and summing the results relevant for each layer. As an example, for a three-layer atmosphere, the first 502

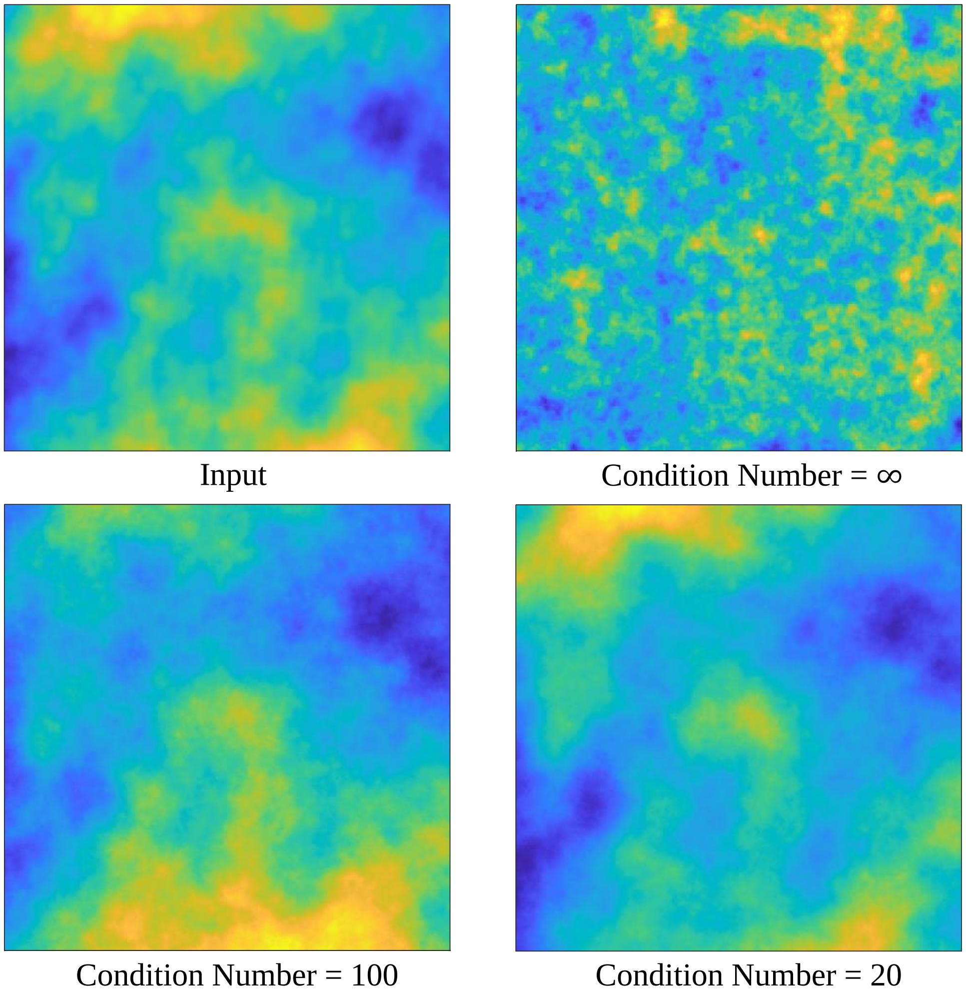

Figure 3.31: Example of a layer reconstructed from a two-layered atmosphere. The input phase screen is shown in the top-left image with the other three images showing the result of more and more restrictive condition numbers.

elements of Φ are used to scale the 502 input modes. All of the modes are then summed to produce a single phase estimate at the range used to generate the first 502 columns of the response matrix. The process is repeated for the next 502 elements to make the next layer and the final 502 elements comprise the third layer. In general, the process is repeated until all layers have been simulated. This provides a 1024×1024 matrix representation of each layer. Each reconstructed phase screen is only valid over the region that can be sampled by the WFS. Outside of this region, the reconstruction cannot be trusted similar to results beyond the isoplanatic angle in classical adaptive optics. Once each layer has been reconstructed, a complete estimation of the atmosphere between the scene and the WFS is achieved. A brief discussion of reconstruction quality is given in Section 4.4 and with a discussion of errors contained in Section 4.5. Once a successful atmospheric reconstruction is obtained, the proof-of-concept simulation is complete.

Chapter 4: Results and Conclusions

The simulation allows a flexible definition of the wavefront sensor to understand how best to design around a given application. Because the current application is working towards a benchtop demonstration, three different atmospheres of similar composition are analyzed to understand the theoretical performance of such a system and the consistency of the results. Each of the three atmospheres is comprised of two distinct turbulence layers at ranges of 16.1 mm and 271.8 mm from the entrance pupil. These ranges were selected to mimic benchtop experiments which are designed as described in Section 3.1.1. One of the three atmospheres is comprised of the two measured phase screens produced by Lexitek, Inc which are described in Section 3.1.1.2. The other two atmospheres use independently generated phase screens to produce additional test cases with worse atmospheric aberration.

These three experiments each followed the same process for generation, measurement, and reconstruction of the atmosphere as outlined in Chapter 3:. Additionally, each of the three simulations used the same hardware parameters and number of field points to enable consistent atmospheric measurements. Each portion of the simulation is analyzed throughout this chapter with the intent to verify performance beginning with the generation of the phase screens and ending with atmospheric reconstruction. Section 4.1 presents the phase screens used in each experiment and provides a comparison to Kolmogorov turbulence. Section 4.2 discusses a qualitative analysis of warp map generation. The results from SLODAR and CLEAN algorithms are analyzed for accuracy in layer identification in Section 4.3. Section 4.4 discusses the reconstruction results and presents various quality metrics for determining the accuracy of the reconstructed atmosphere. The primary reconstruction errors are analyzed in Section 4.5 to understand how each affects the reconstruction. Section 4.6 analyzes how the benchtop parameters scale to a real-world system and Section 4.7 provides conclusions based on the analyses in this chapter.

4.1 Phase Screen Quality

The phase screens are designed to follow Kolmogorov statistics to demonstrate WFS performance for a two-layered atmosphere representative of realistic turbulence. The six phase screens used in validation of the simulation are shown in Figure 4.1 with each row of images representing the two layers used in each of the three input atmospheres. The isoplanatic layers shown on the left-hand side of the figure are sized at 192×192 pixels while the anisoplanatic layers on the right-hand side are 262×262 pixels. This allows for requisite sampling at the specified range without making the phase screens overly large. The pixel size of each screen, both measured and simulated, is set to a 60 μm pitch as described in Section 3.1.2.

Each of the six input phase screens are analyzed to determine their turbulence properties. The simplest parameter to investigate is the Fried length, r_0, which is estimated using Equation 3.3 and following the corresponding procedure established in Section 3.1.2. Knowledge of the Fried length for each screen allows the computation of the atmospheric parameters D/r_0 and FOV/θ_0 which define the atmosphere as a whole. The process for combining the Fried parameters of the individual layers is outlined in Equation 3.1. Fried parameters for each screen are given in Table 4.1 along with the properties of each of the three atmospheres. As seen in the table, the measured plates exhibited the weakest turbulence, and the two simulations were relatively similar in terms of turbulence strength with the first simulation containing slightly stronger turbulence.

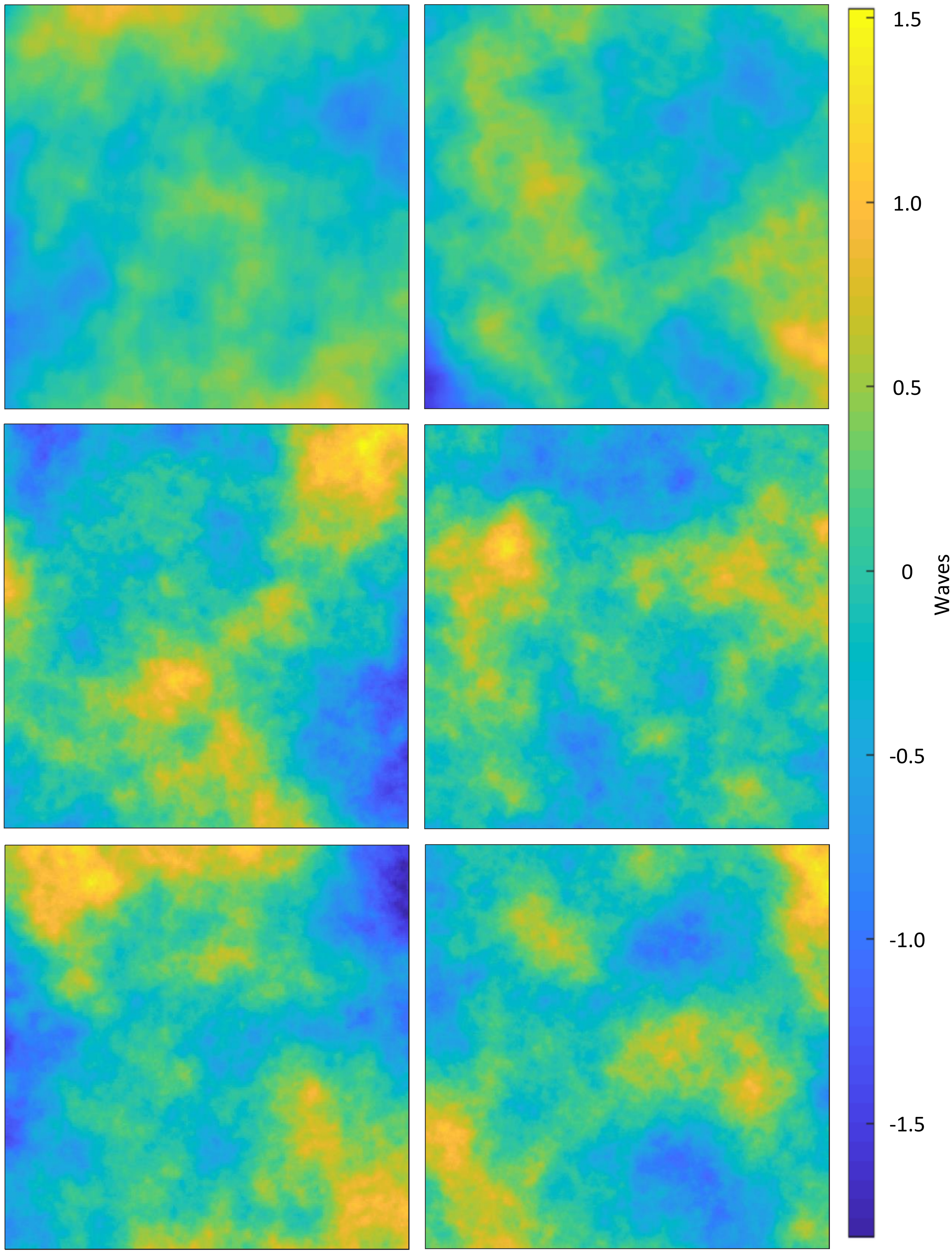

Figure 4.1: The six phase screens used in demonstrating WFS performance. The images on the left correspond to the isoplanatic phase screens and the right-hand images are the anisoplanatic phase screens. The top screens are the measured phase plates while the central and bottom pairs are simulated screens

Table 4.1: Summary of aberration parameters for measured and simulated phase screens and the resulting atmospheres

Atmosphere Label	Description	Value
Measured Screens	r_0 - Layer 1	1.7 mm
	r_0 - Layer 2	1.6 mm
	D/r_0 – Atmosphere	10.3
	FOV/θ_0 – Atmosphere	9.5
Simulation 1	r_0 - Layer 1	1.12 mm
	r_0 - Layer 2	1.07 mm
	D/r_0 – Atmosphere	15.5
	FOV/θ_0 – Atmosphere	14.1
Simulation 2	r_0 - Layer 1	1.07 mm
	r_0 - Layer 2	1.14 mm
	D/r_0 – Atmosphere	15.4
	FOV/θ_0 – Atmosphere	13.3

In addition to computing the Fried length, each screen is analyzed to assesses the structure function, D_ϕ. The structure function of a given screen is defined by Equation 1.3. D_ϕ is computed by creating a shifted copy of the phase screen $[\phi(\boldsymbol{r} + \Delta\boldsymbol{r})]$, subtracting the original screen $[\phi(\boldsymbol{r})]$, squaring the resulting values, and taking the mean of all overlapping matrix elements. This defines the structure function value for the shift $\Delta\boldsymbol{r} = (\Delta x, \Delta y)$. Doing this for all possible shifts yields the two-dimensional structure function. Equation 1.4 shows that the structure function for Kolmogorov turbulence follows a $\Delta\boldsymbol{r}^{5/3}$ power law. To assess the power law associated with the phase screen, the radial average of the structure function is computed. This one-dimensional curve is fit in log-log space with a line of the form $y = mx + b$ for small values of $\boldsymbol{\Delta r}$ as given in the equation

$$ln\left(D_\phi(\Delta r)\right) = ln\left(6.88\left(\frac{\Delta r}{r_0}\right)^\alpha\right) = m \cdot ln(\Delta r) + b. \quad 4.1$$

Rearranging Equation 4.1 to take advantage of properties of logarithms yields

$$\alpha\, ln(\Delta r) + \left[ln\left(\frac{6.88}{r_0^{5/3}}\right)\right] = m \cdot ln(\Delta r) + b. \quad 4.2$$

It is assumed that $\alpha \approx 5/3$ such that setting the exponent for the Fried length to 5/3 results in only a small error. This is done to allow for a clean separation of variables. This first order approximation makes α equal to the slope of the linear fit to the structure function in log-log space.

An example of a two-dimensional structure function for Simulation 1 Layer 1 along with the radial average and linear fit are shown in Figure 4.2. Modeling limitations typically underrepresent low spatial frequencies, and the tilt removal adds further deviations from a strict adherence to a $\Delta r^{5/3}$ power law. Because of these limitations, the linear fit is applied to small values of $\ln(\Delta r)$ and deviations at larger values are as expected. The slope of the linear fit for the radial average estimates a power law exponent of $\alpha \approx 1.84$ for this phase screen. The other phase screens shown in Figure 4.1 yield similar results with the measured screens deviating the furthest from Kolmogorov statistics. The value of α estimated from Figure 4.2 matches the expected structure function exponent of $\alpha = 5/3$ with a relative error of 10%. An important point regarding

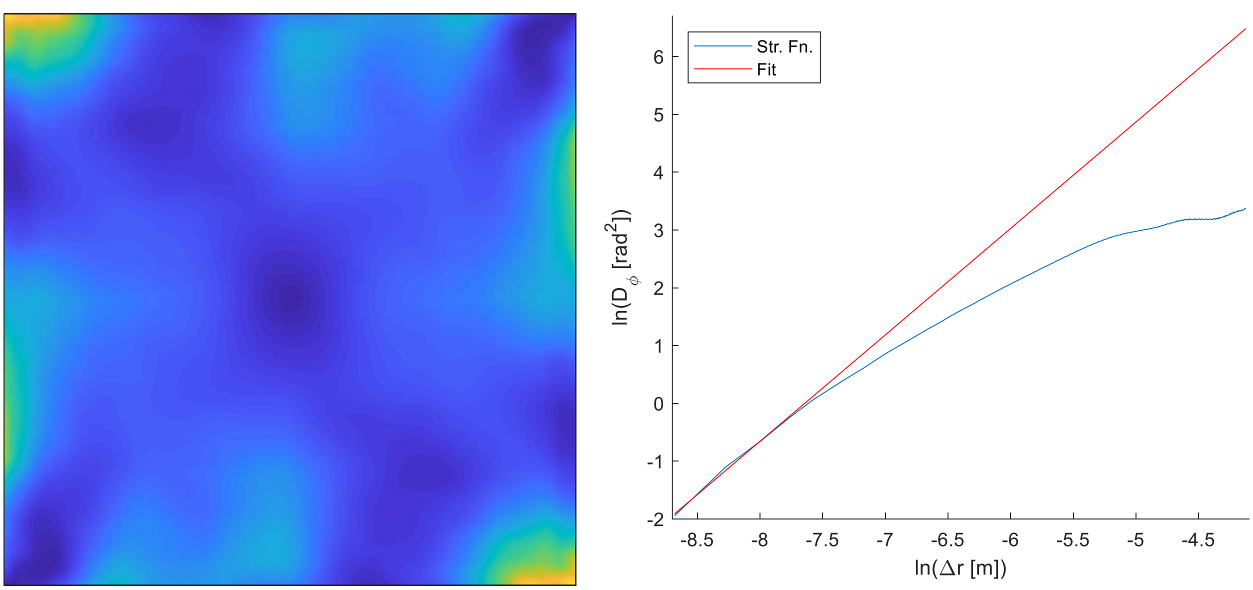

Figure 4.2: Structure function for the isoplanatic layer in Simulated Atmosphere 1. The left image shows the two-dimensional structure function while the right-hand image shows the radial average with a linear fit to small values of $ln(\boldsymbol{\Delta r})$.

the phase screen design is that while each screen is generated following Kolmogorov statistics, the ability of the simulation to reconstruct an input phase screen is not dependent on strict adherence to the $\Delta r^{5/3}$ power law. With this allowance, the input phase screens are deemed acceptably similar to an atmospheric environment for the proof of concept simulation.

4.2 Warp Map Generation

The ultimate measure of successful warp map generation lies in the reconstruction of the phase screens, but simple qualitative checks are made to ensure that expected behavior for a given input screen is observed. This includes effects due to anisoplanatism and comparisons of the slope magnitudes and directions based on the input phase screen. Anisoplanatism is expressed in the warp maps by variation in the slope vector directions within a sub-image and a repetition of patterns in the slopes between sub-images. The repetition in warp map features between adjacent lenslets occurs because the portion of phase screen sampled by a given sub-aperture increases with distance. A simple example of this is shown in Figure 4.3 where the full FOV for two adjacent lenslets is given along with a shaded region marking the portion of the phase screen sampled by both sub-apertures.. The overlapping portion of the phase screen observed by adjacent lenslets

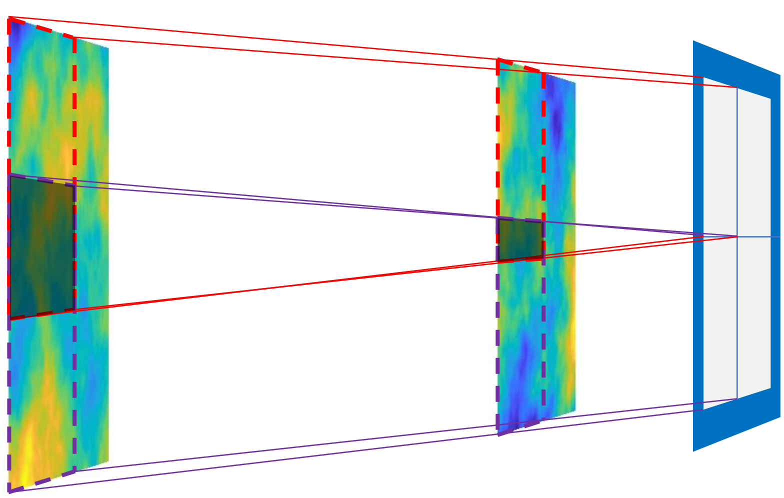

Figure 4.3: Cartoon showing the full FOV from two adjacent lenslets. The region of the phase screen sampled by both lenslets is shown in black. More overlap occurs for screens located further form the entrance pupil.

increases for more distant turbulence layers generating more overlap in the slope information contained in adjacent sub-images. On the other hand, isoplanatic aberration is expressed by all slope vectors having a consistent magnitude and direction within a sub-image. Because the phase screen is near the pupil, little to no overlap in warp map features is observed and each slope vector is dominated by the overall wavefront tilt across the lenslet.

To illustrate the qualitative features observed in warp maps at various ranges, two example phase disturbances are shown in Figure 4.4 for a 5×5 lenslet array viewing a 15×15 array of objects. The first row of images shows a parabolic phase disturbance representative of the defocus aberration. The bottom row shows the measured phase screens procured from Lexitek, Inc. The left-hand images are inserted near the telescope entrance pupil and the warp maps exhibit isoplanatic behavior. The right-hand images are inserted 271.8 mm away and the anisoplanatic behavior of warping within a sub-image and repeated features in neighboring arrays are clearly observed. It should be noted that while the phase disturbance responsible for the anisoplanatic warping is plotted beneath the warp maps, the locations on the warp map do not correspond one-to-one with the phase screen. This is because the field of view for each sub-aperture expands and overlaps at the turbulence layer. Additional phase aberrations were also investigated with similarly successful qualitative results for a variety of input screens at a variety of ranges.

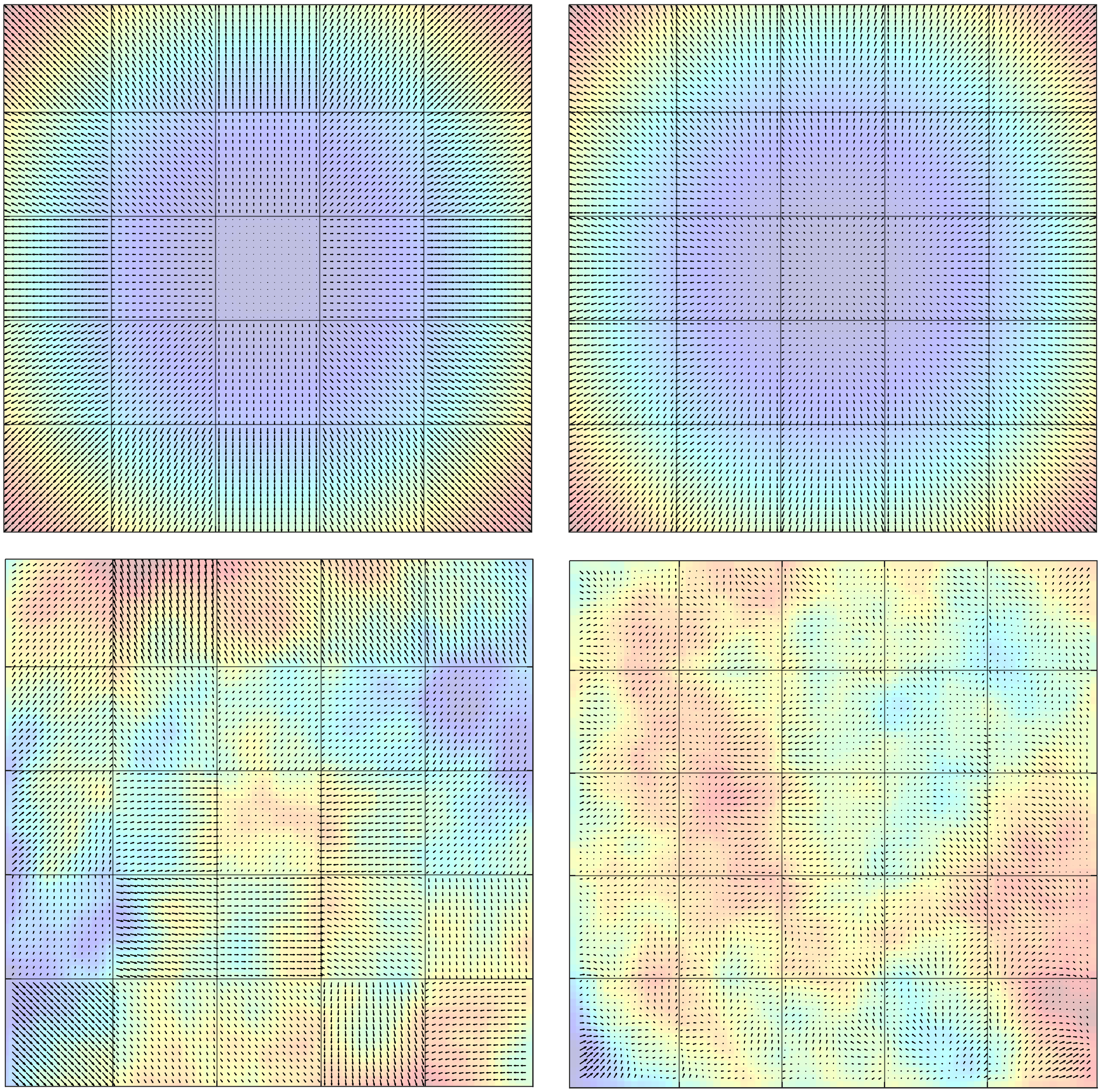

Figure 4.4: Images showing warp maps for qualitative analysis. The top images are for a parabolic defocus aberration and the bottom images are the measured physical phase screens. The left column is inserted near the pupil while the right column shows warping from a distant layer. Anisoplanatic effects are seen by varying vector length and direction within a lenslet and repeated features between lenslets.

4.3 Layer Identification

One of the key features of the WFS is the ability to identify significant layers of turbulence from the generated warp maps. Layer identification incorporates both the SLODAR and CLEAN algorithms discussed in Section 3.5 and Section 3.6 respectively. The modified SLODAR algorithm analyzes the correlations between all lines of sight through the atmosphere while the variation on the CLEAN algorithm analyzes the resulting profile for likely layers of turbulence. The CLEAN algorithm needs to be tuned to the given application, but successful preliminary results are achieved with a basic tuning as described in Section 3.6. While the SLODAR algorithm is performed on each dataset, the results can be averaged over several datasets prior to analysis using the CLEAN algorithm to reduce noise in the turbulence profile.

The metrics used to determine successful implementation of the SLODAR and CLEAN algorithms are the identification of input layers and the accuracy of range estimates to each input layer. The SLODAR profiles from the three atmospheres described in Section 4.1 were each analyzed with varying boxcar widths to assess the accuracy of layer identification in the presence of increased averaging. The turbulence profiles resulting from the SLODAR analysis for each of the three input atmospheres are shown in Figure 4.5. While the full dataset extends to $h_{max} = 8656$ mm, the plot extends only to 3032 mm due to the limited size of the phase screens as described in Section 3.7. As seen in each of the three plots, the increase in boxcar width diminishes the noise of the profile and reduces large spurious spikes which complicate the CLEAN analysis. Additional averaging through multiple frames in a dynamic simulation will aid in smoothing out the profile and reducing spurious values and may reduce or eliminate the need for wide boxcar averages prior to implementation of the CLEAN algorithm.

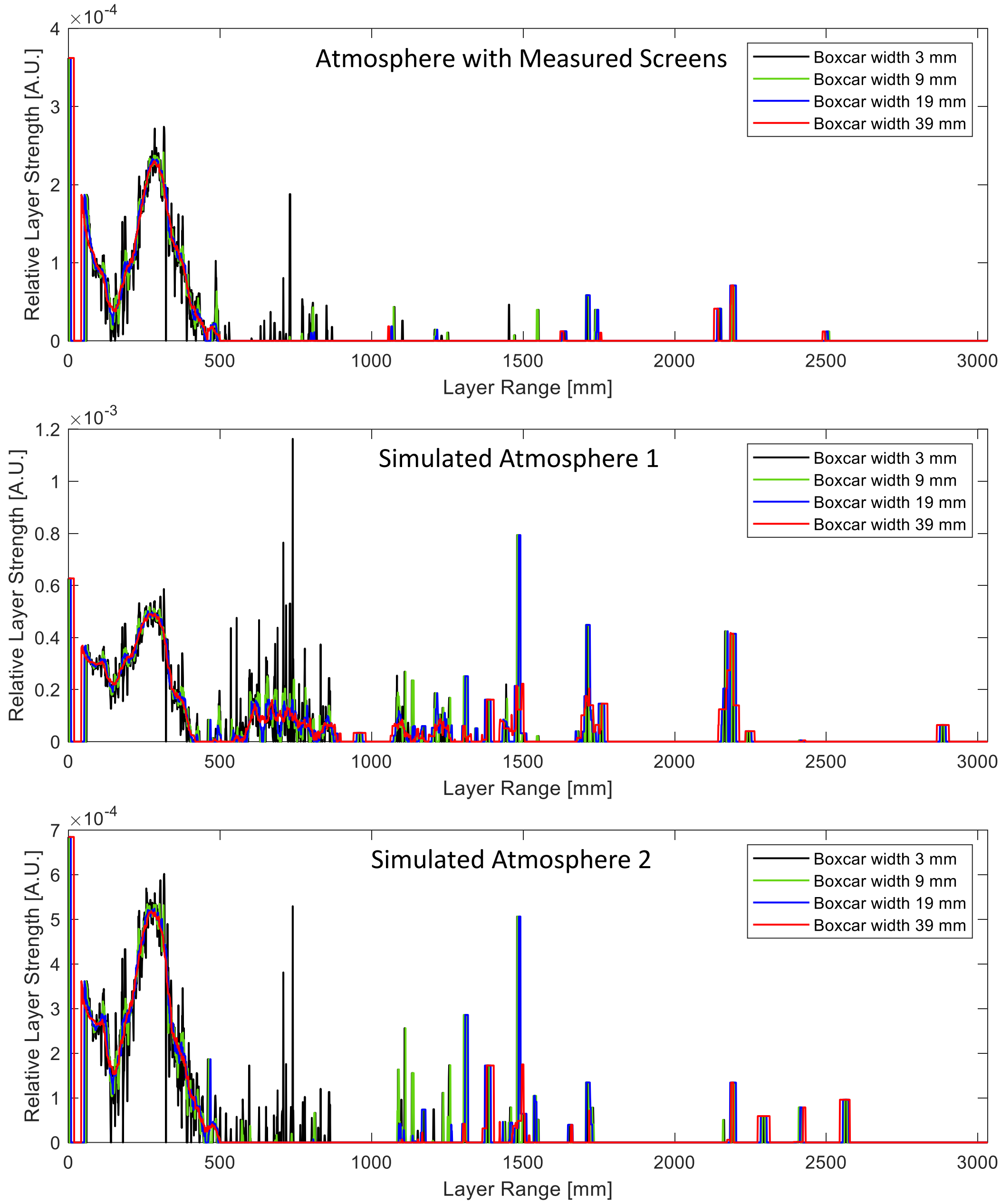

Figure 4.5: Turbulence profiles for the three generated atmospheres. Each atmosphere contains a phase layer at 16.1 mm and one at 271.8 mm. Each atmosphere was analyzed with four different boxcar widths to understand the ideal level of averaging

One requirement for the simulation is to correctly identify ranges to the input layers using the CLEAN algorithm variation. To determine the change in performance as a function of boxcar width, each of the twelve profiles plotted in Figure 4.5 were analyzed across their entire range. The results of the analysis are summarized in Table 4.2 with layers beyond the 3032 mm range cutoff identified in red. The layers beyond this cutoff are not carried through the rest of the analysis but are included in the CLEAN results for completeness. Table 4.2 also labels the cases numerically for a simplified identification in the references throughout this chapter. The output ranges were divided by 105% prior to insertion in Table 4.2 to account for the calibration factor identified using Table 3.5.

Table 4.2: Summary of the layers identified by the CLEAN algorithm for three different atmospheres

Case #	Atmosphere Label	Boxcar Width [mm]	Layer 1 [mm]	Layer 2 [mm]	Layer 3 [mm]	Layer 4 [mm]	Layer 5 [mm]	Layer 6 [mm]
-	Input	-	**16.1**	**271.8**	-	-	-	-
1	**Measured Screens**	3	0	299	699	-	-	-
2		9	0	294	-	-	-	-
3		19	0	278	-	-	-	-
4		39	0	273	-	-	-	-
5	**Simulation 1**	3	0	-	-	-	-	-
6		9	0	258	1412	2070	4130	4136
7		19	0	254	1425	2075	4137	-
8		39	0	270	4148	-	-	-
9	**Simulation 2**	3	0	250	701	-	-	-
10		9	0	298	1415	-	-	-
11		19	0	271	1422	-	-	-
12		39	0	264	-	-	-	-

The results listed in Table 4.2 show several interesting features. In general, larger boxcar averages yield more accurate results for a single frame in each of the two-layered atmospheres. The largest boxcar width is still well below the typical Lorentzian width found in Table 3.5, but use of a larger boxcar average could begin to wash out layers which may be adjacent to one another. This would limit the ability to identify multiple closely spaced layers using this static analysis, but the inclusion of dynamic turbulence will aid in recovering the lost information. The incorporation of layer identification through wind speed analysis will allow identification of closely spaced layers due to differences in the corresponding wind vectors (Wang et. al. 2008).

Table 4.2 also allows a quantitative analysis of CLEAN performance. The atmosphere generated using measured screens showed good range estimates in all cases with all anisoplanatic layer range estimates within 10% of the input value and only a single additional layer identified in Case #1. The atmosphere corresponding to Simulation 2 showed similar results with a third layer identified in three of the four cases and the anisoplanatic layer again within 10% of the input value. The atmosphere corresponding to Simulation 1 had the largest variety of results with several interesting features. The smallest boxcar average identified only a single peak at the entrance pupil. This is caused by the large spurious peak seen in Figure 4.5 at 740 mm setting a threshold which excludes the real layer at 271.8 mm. This spurious peak was not identified as a layer because the Lorentzian fit parameters fell outside of acceptable bounds. The next two cases, Case #6 and Case #7, identified the anisoplanatic layer within roughly 6% ranging error with both cases finding two additional layers within the valid analysis range due to large spikes in the correlation data. Finally, the widest boxcar case correctly identified the anisoplanatic layer with only a single additional layer which is located beyond the region of validity. In summary, eleven of the twelve cases show good identification of the anisoplanatic layer with improved ranging results using a wider boxcar average in each of the three atmospheres.

While the two layers of interest were identified with sufficient accuracy, over half of the cases identified additional layers which were not input into the simulation. As with the accuracy of layer ranging, wider boxcar averages tended to reduce the number of additional layers identified. One method to reduce the number of false positives is additional tuning of the CLEAN functional fits. Additional cross-checks can also be added at the expense of processing time and additional complexity. While the identification of additional layers is not ideal and increases the number of computations in atmospheric reconstruction, reconstruction results are not severely impacted by the reconstruction of additional layers. This is demonstrated and discussed further in Section 4.4. In general, the phase amplitude in reconstructions of non-input layers is small compared to reconstructions of input phase layers.

4.4 Atmospheric Reconstruction

The ultimate test for the WFS and the validation for the simulation is the reconstruction of the atmosphere. With a knowledge of the three-dimensional atmospheric composition, corrections can be made using either hardware or software solutions. Atmospheric reconstruction occurs by reconstructing each identified turbulence layer as detailed in Section 4.4.1. Once all layers are reconstructed, the atmosphere is built by inserting the layers at their corresponding ranges identified in Table 4.2 and observing the accumulated phase along different lines of sight as described in Section 4.4.2. Section 4.4.3 compares the wide-field results to reconstruction along a single line of sight as seen in classical adaptive optics methods. The goal for each of these three sections is to investigate a separate quality metric and to assess the ability of the WFS to successfully predict the atmosphere that it has measured.

4.4.1 Reconstruction of Individual Layers

The atmosphere is reconstructed layer by layer using a response matrix customized to the measured layer ranges. Each of the layers identified in Table 4.2 are reconstructed using a condition number of 33. This condition number was selected by analyzing the reconstruction quality for the measured screens and applying the result to the simulated screens as well. The simulated screens perform slightly better at a higher condition number, but the reduction in RMS wavefront error is small for a small change in condition numbers. Once the atmospheric reconstruction is complete, the reconstruction of each layer can be analyzed independent of the others.

For the most part, the layers were reconstructed with high accuracy. A few select cases are shown here to demonstrate reconstruction in some of the more interesting cases. Figure 4.6 shows the input and reconstructed phase screens for Case #1 where a single additional layer was identified. The additional layer shows low phase amplitude compared to reconstructions of input layers and the aberration content includes mostly low spatial frequencies. Case #5 is shown in Figure 4.7 where only the isoplanatic layer was identified. This case is very interesting as it is the only case where an input layer was not identified. This case is discussed in more detail in Section 4.5.1, but the isoplanatic layer shows good reconstruction and correction of this layer will result in performance similar to GLAO. Figure 4.8 demonstrated reconstruction with two additional non-input layers. Again, the additional layers show low spatial frequency, low amplitude reconstructions. Layer 1 and Layer 2 also show some crosstalk in the phase aberration. This is

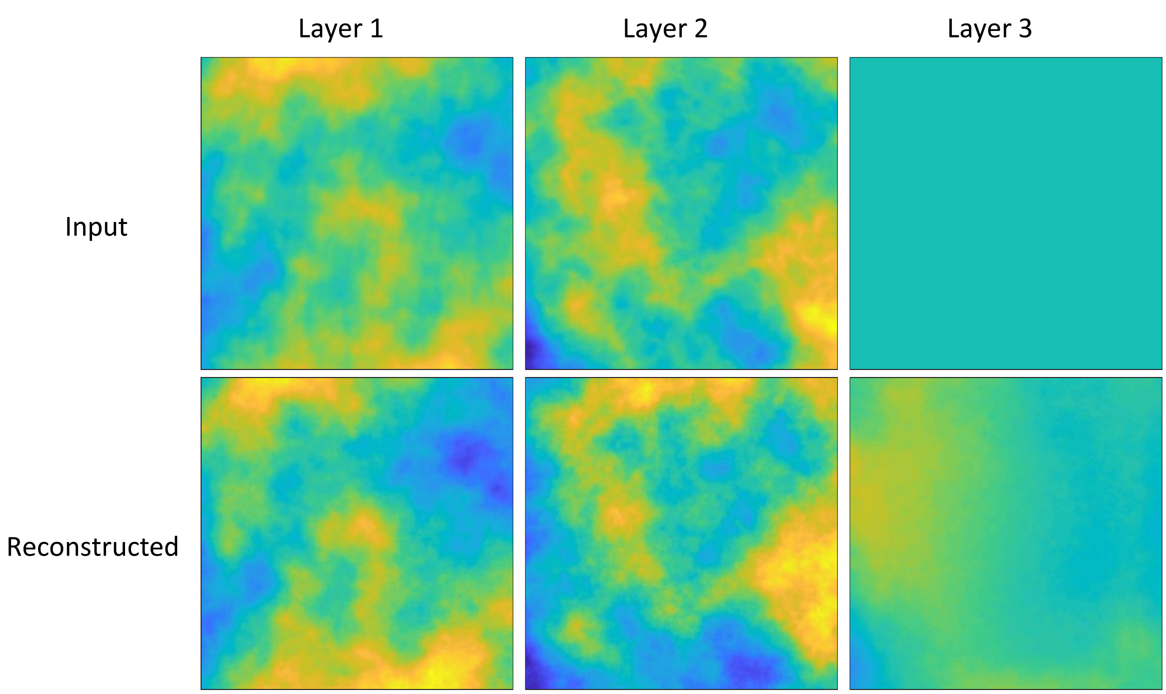

Figure 4.6: Input and reconstructed layers for Case #1 with a condition number of 33.

present in all of the plots but can be seen most easily in Figure 4.8. Finally, Case #12 correctly identifies the two phase layers and the input and reconstructed screens are shown in Figure 4.9.

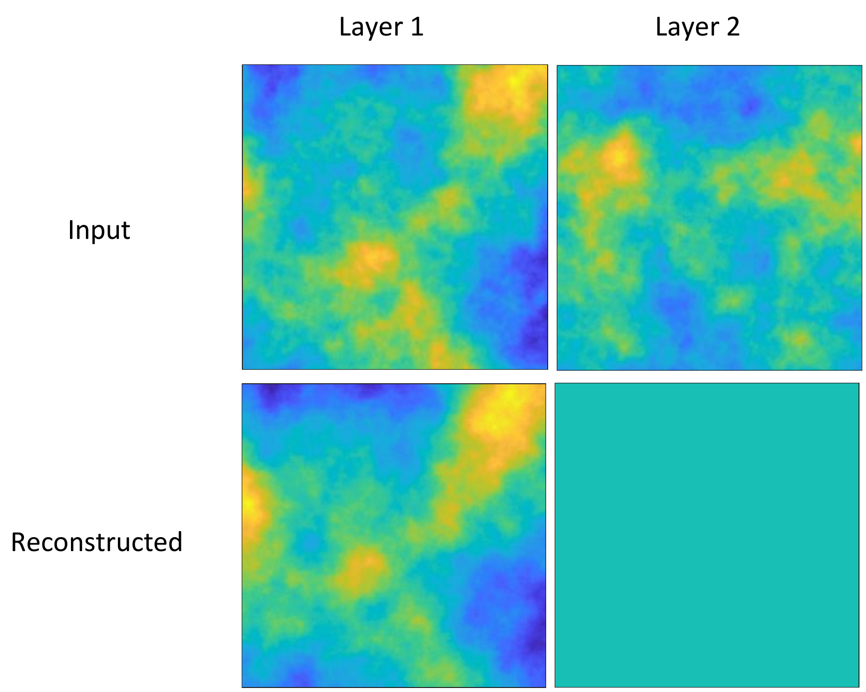

Figure 4.7: Input and reconstructed layers for Case #5 with a condition number of 33.

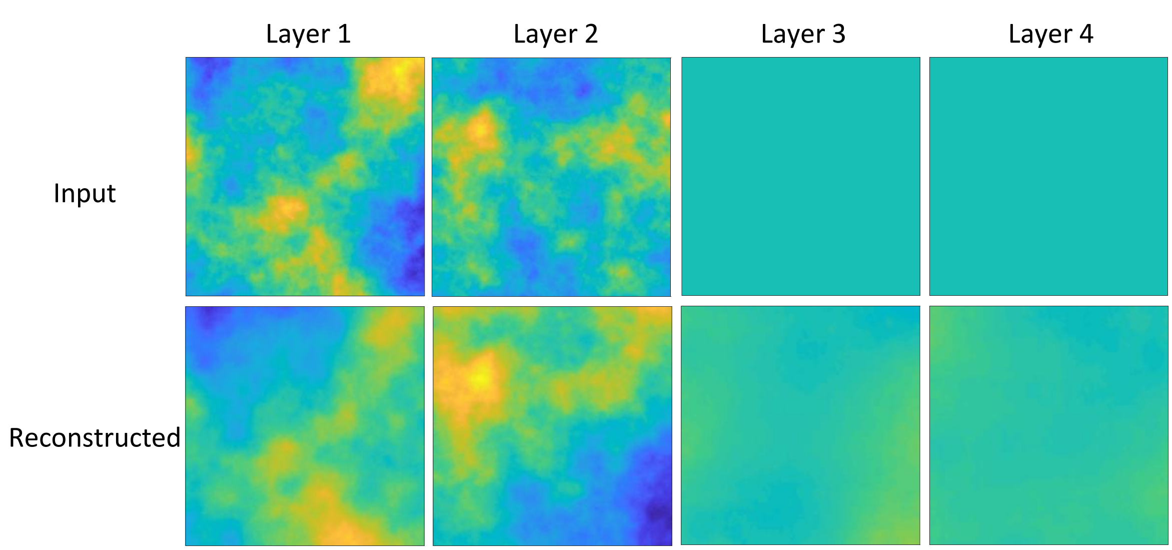

Figure 4.8: Input and reconstructed layers for Case #6 with a condition number of 33.

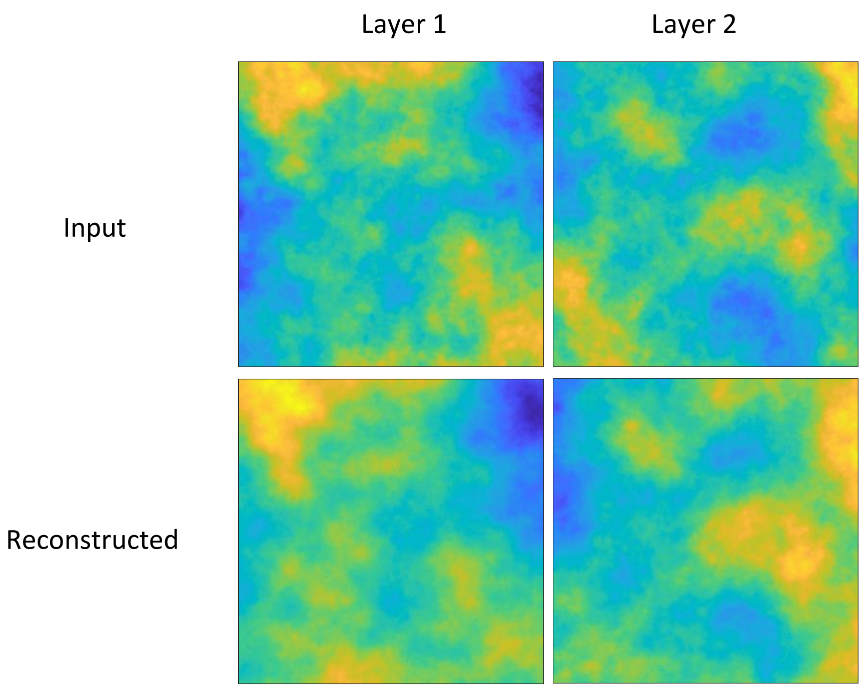

Figure 4.9: Input and reconstructed layers for Case #12 with a condition number of 33.

Because the total phase disturbance is redistributed somewhat between layers, a quantitative analysis of individual layer reconstruction is not a useful measure of success. A simple example of the redistribution of phase aberration is the distribution of overall tilt. Tilting in a single layer causes a change in the line of sight. Angular changes to the line of sight further from the entrance pupil cause smaller shifts for the same tilt, but there is no way to distinguish a small tilt from a screen near the entrance pupil from a large tilt in a screen far from the entrance pupil. Overall tilt can be applied to any of the layers without changing the overall reconstruction of the atmosphere. In spite of the phase redistribution, a qualitative look at the reconstructions shows high correlation between the input and reconstructed phase screens. A wide variety of atmospheres with a varying number of layers at more diverse ranges were also explored with similar qualitative results. Distribution of the reconstructed phase aberration to different layers occurs more frequently with an increase in layers.

4.4.2 Phase Aberration Along Lines of Sight

While individual layer reconstruction allows for a qualitative check that reconstruction is successful, the true test of the WFS lies in the reconstruction of the atmosphere as a whole. Individual screens may show deviations from the input screens which are compensated by other layers once combined. To analyze the success in reconstructing the atmosphere, the total phase aberration along discrete lines of sight are analyzed. Analyzing all lines of sight through the atmosphere enables a quantitative analysis of the reconstruction quality and the residual wavefront error that goes unmeasured along each line of sight. To compute the residual wavefront error along a line of sight, the total phase aberration is computed for both the simulated and reconstructed atmospheres. Results along two lines of sight for cases 4, 8, and 12 are given in Figure 4.10 and Figure 4.11 where each scale bar represents the residual WFE, but do not represent the simulated or reconstructed phase amplitude. These three cases represent each of the three simulated atmospheres. Input and reconstructed phase aberration along with residual wavefront error are

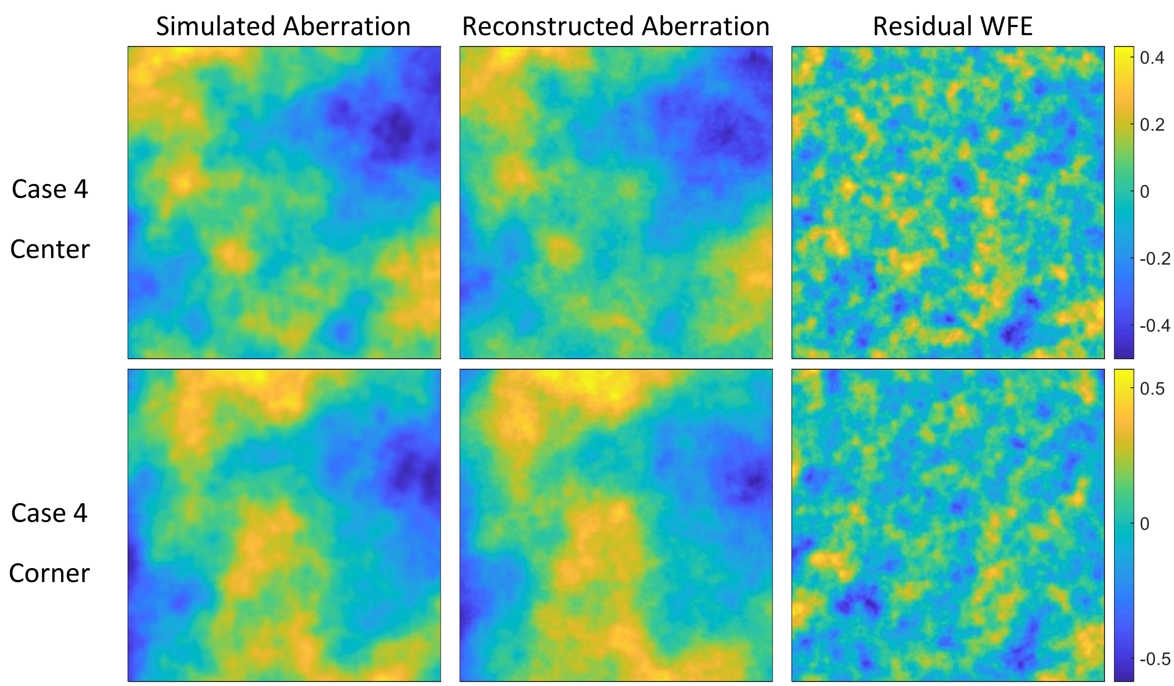

Figure 4.10: Simulated and reconstructed phase aberration along two lines of sight are given for Case #4 along with the residual wavefront error in units of waves.

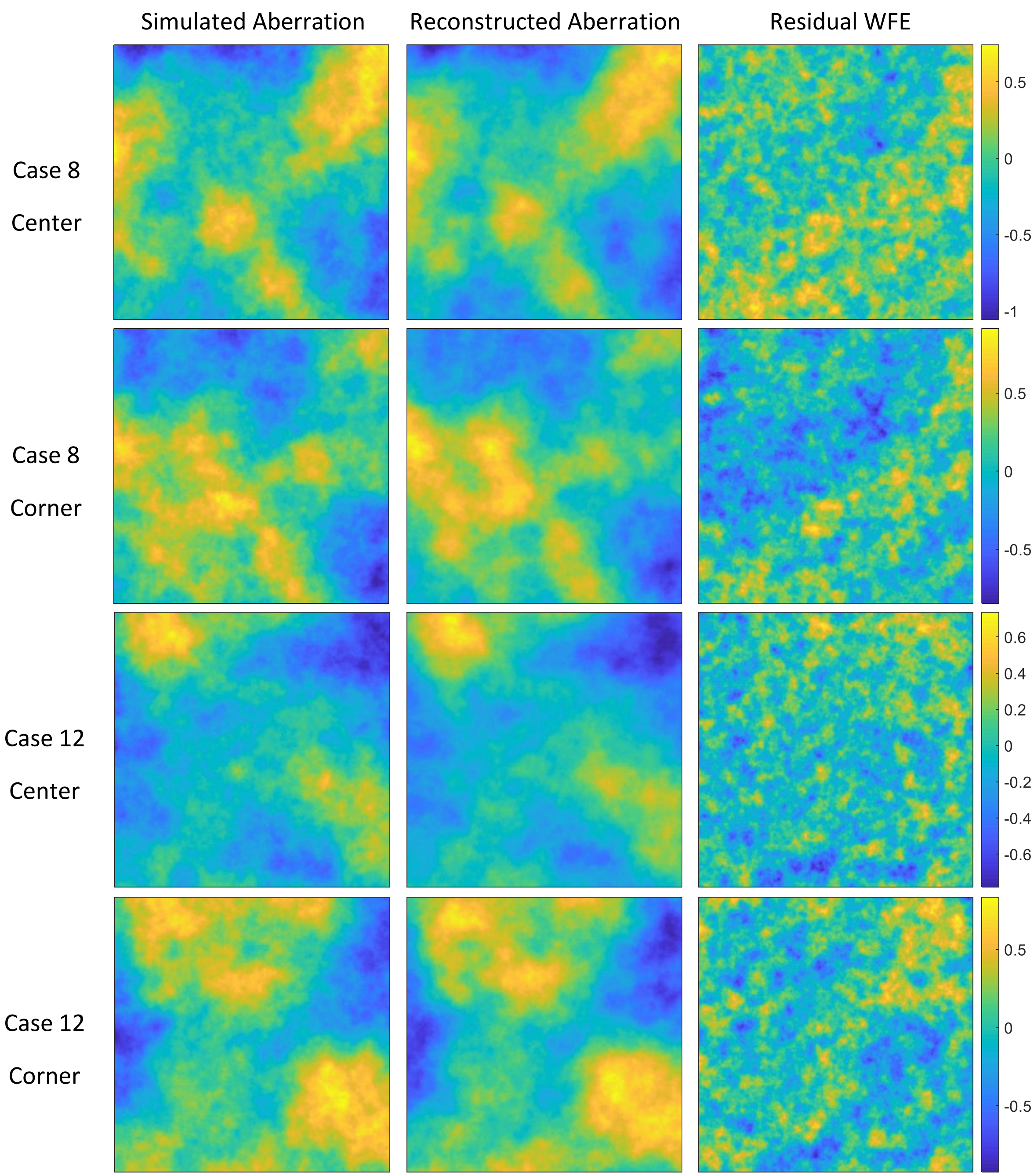

Figure 4.11: Simulated and reconstructed phase aberration along two lines of sight are given for Case # 8 and Case #12 along with the residual wavefront error in units of waves.

shown for each of the depicted cases. While the residual wavefront error has a peak-to-valley amplitude between 1 and 2 waves, the average RMS wavefront error from the six pictured lines of sight is 0.20 waves. Aberration with RMS wavefront error less than 0.25 waves is typically considered diffraction limited (Greivenkamp 2004). This line-of-sight information will eventually be used in the computation and deconvolution of the field dependent PSFs.

The ability to measure along any desired line of sight enables the ability to analyze the atmosphere across the full field of view. Each line of sight to the 15×15 array of object points is analyzed for each of the twelve reconstructed atmospheres described in Table 4.2. Once the RMS wavefront error is computed for a line of sight, it is assigned to a matrix element in a 15×15 array. A summary for eleven of the twelve cases is given graphically in Figure 4.12. Case #5 was excluded from this analysis since only a single layer was identified, but this case is discussed further in Section 4.5.1. Each of the images shows consistent reconstruction across the field of view with slightly worse results near the edges and corners. Additionally, the atmosphere using measured screens shows better reconstruction than the atmospheres with numerically generated screens. This is expected due to the lower values of D/r_0 and FOV/θ_0. In general, the reconstructions are shown to be near or below the diffraction limit of 0.25 waves of RMS wavefront error for most lines of sight in the eleven cases shown. This is important as any diffraction limited, field dependent PSF from the reconstructed phase screens will match the aberration content observed in the scene through the telescope. With accurate field dependent PSFs, accurate correction of the science image can be achieved without significant error contribution from the reconstruction process. Figure 4.12 verifies this wavefront sensor as a viable candidate for wide field adaptive optics with good reconstruction across the entire FOV for the three simulated atmospheres.

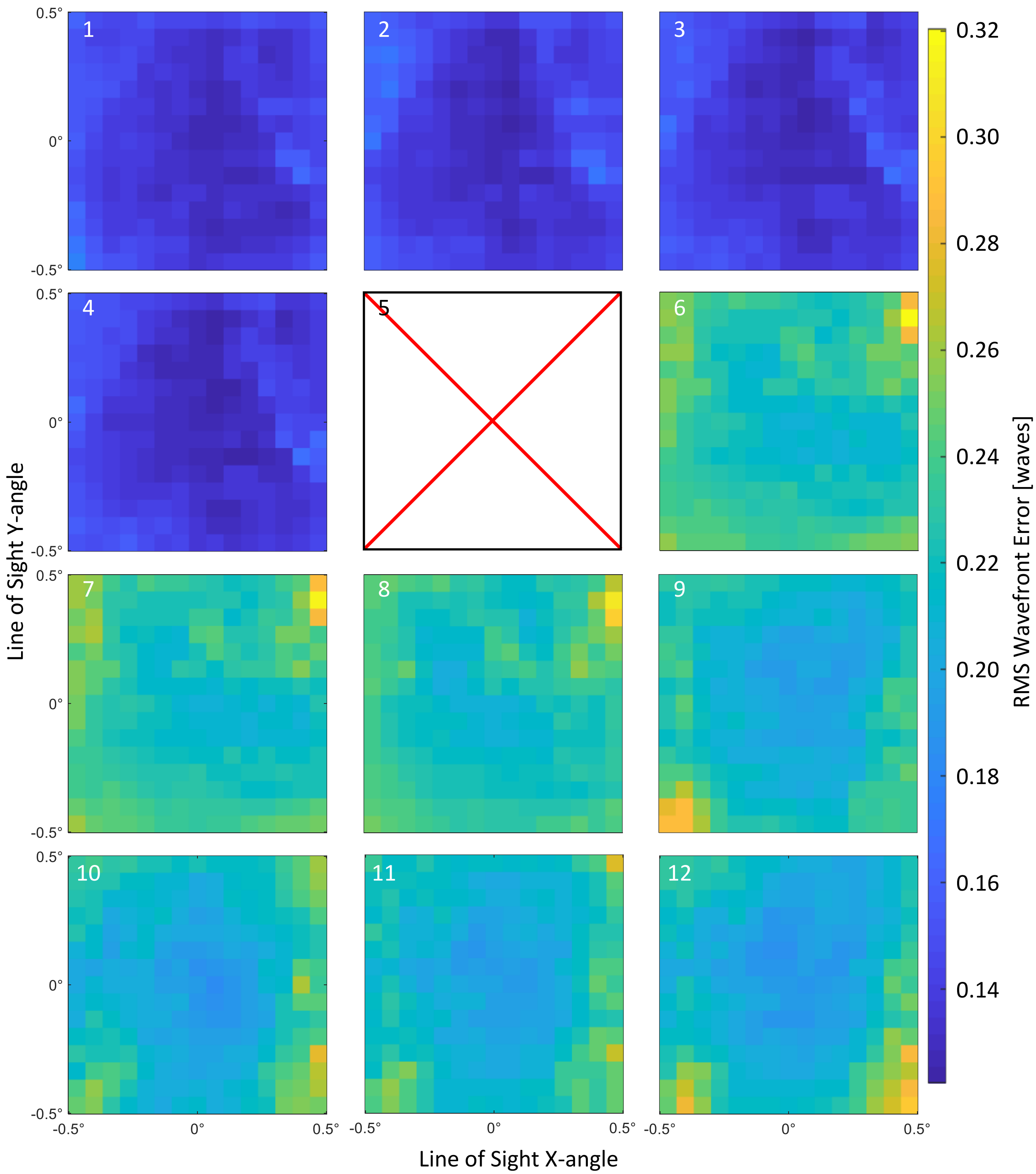

Figure 4.12: RMS wavefront error for all lines of sight within the instrument FOV for eleven of the twelve cases.

4.4.3 Comparison to Classical Adaptive Optics

Analysis along individual lines of sight enables comparison with classical adaptive optics to determine the improvement that can be achieved through off-axis atmospheric reconstruction. Classical adaptive optics measures the phase disturbance along a single line of sight using a single guide star and applies the correction over the full field of view using a single DM. To compare the wide-field reconstruction results to a classical AO system, the center line of sight reconstruction is assumed to be applied to all lines of sight. This assumption implies that the WFS for the classical AO system has identical performance to the central line of sight of the WISH WFS which may not be true for all systems. A two-dimensional map like those shown in Figure 4.12 is generated showing the residual wavefront error when the reconstruction from the central line of sight is compared to the known phase aberration across the full field of view. An example of this is shown in Figure 4.13 for Case #4. This graphical result matches what is theoretically expected from Equation 1.6 within a factor of two. Comparing this result on an element-by-element basis to the

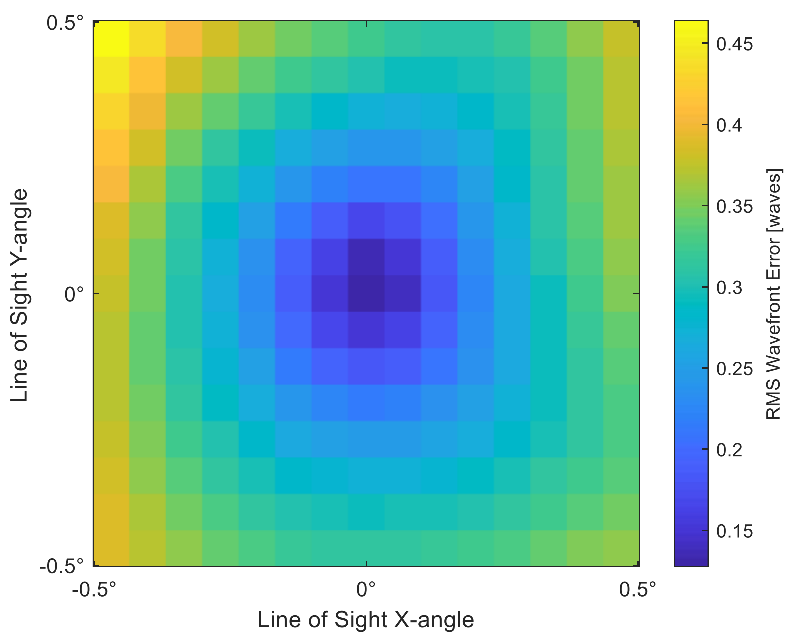

Figure 4.13: Example of reconstruction error predicted from classical adaptive optics measurements for Case #4.

results for Case #4 in Figure 4.12 demonstrates the improvement that is achievable by performing a wide-field reconstruction of the atmospheric aberration compared to the single line of sight reconstruction achievable through classical AO. The percentage reduction in RMS wavefront error is computed for each line of sight by dividing the error computed in the wide-field reconstruction by the error computed using only the central line of sight. The results for eleven of the twelve cases from Table 4.2 are shown in Figure 4.14 for this two-dimensional analysis. Case #5 is once more omitted in this analysis due to the missing anisoplanatic screen. The corresponding results for Case #5 are again discussed in Section 4.5.1.

The results of Figure 4.14 show that the wide-field reconstruction offers a considerable improvement on equivalent single line of sight techniques. The wavefront error along extreme lines of sight is reduced by nearly a factor of three in the best case and more than a factor of 2.4 in the worst case. All eleven cases show reduction rolling off from the central line of sight regardless of the input phase screens used and the number of phase screens which were reconstructed. Comparing both Figure 4.12 and Figure 4.14 shows a relatively weak overall dependence on the changing parameters from the wider boxcar averages. This includes the reconstruction of layers which were not input and ranging errors for the input layers up to roughly 10%. In general, the RMS wavefront error results along all lines of sight demonstrate that the atmospheric composition changed the results much more drastically than the small variations in the CLEAN algorithm outputs.

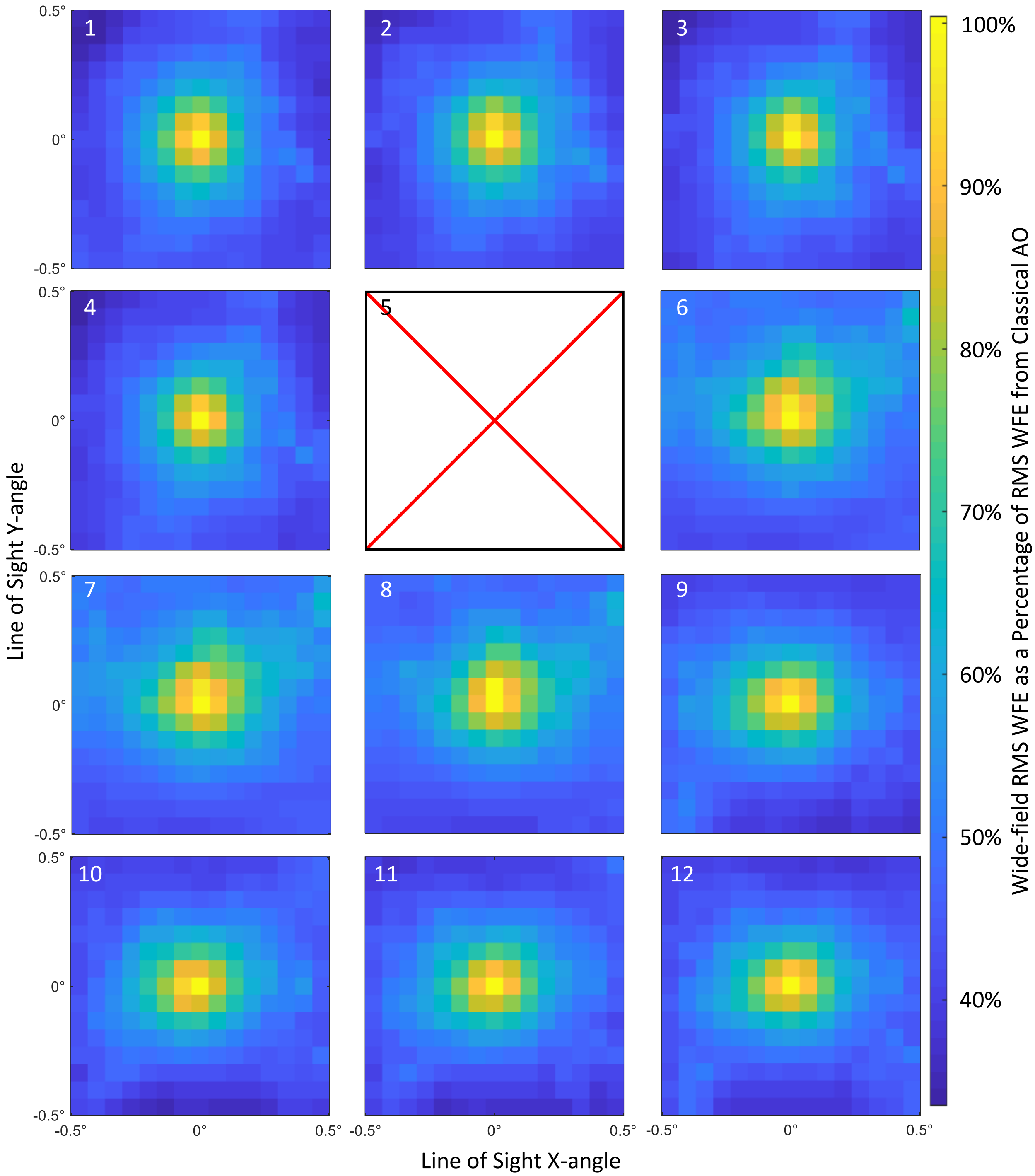

Figure 4.14: Comparison of RMS wavefront error (WFE) results from the simulated wide-field WFS and the reconstruction from classical AO. Results are shown as percentages using the ratio $\frac{WFE_{Wide-field}}{WFE_{Traditional}}$.

4.5 Analysis of Reconstruction Errors

With the successful reconstruction of each of the input atmospheres, an analysis is needed to demonstrate the effects of errors introduced throughout the processing. The three main questions addressed in this section regarding reconstruction errors are

1. How does the algorithm respond when input layers are not identified?
2. How does an error in range identification affect the reconstruction of a phase screen?
3. How does increasing the field of view affect the reconstruction error for a given atmosphere?

With the demonstrated ability to input and reconstruct an arbitrary atmosphere, the simulation is used to probe each of these effects to understand the additional wavefront error induced in the WFS processing.

4.5.1 Missing Layer Identifications

When performing the CLEAN algorithm variation described in Section 3.6, there is a risk that automated identification of a layer can fail. Optimizing the boxcar averaging and taking advantage of dynamic atmospheric measurements improves the likelihood of identification of all significant layers. Similarly, fine tuning the algorithm thresholds and increasing complexity for a more rigorous peak search will yield more robust results. Despite these efforts, there will still be cases where a layer will not be identified. To assess the impact on successful reconstruction, a three-layer atmosphere is developed where all layers have near equal turbulence strength. This atmosphere consists of layers 0 mm, 312 mm, and 1053 mm away from the telescope entrance pupil. It is assumed that the range to each layer is perfectly known for the purposes of reconstruction. To understand the effects of a missing layer, the reconstruction is performed once for a complete atmosphere and three times with one of the input layers missing. The layer reconstruction is shown along with the RMS wavefront error across the FOV and the percent improvement over classical adaptive optics measurements. Results assessing the performance across the field of view are plotted on the same scale for ease of comparison between the four cases.

To begin the analysis the atmosphere is reconstructed without any input errors. All three layers are present and are reconstructed at accurate ranges. The results are shown in Figure 4.15 where a faithful reproduction of all layers is seen and the RMS wavefront error is well below the

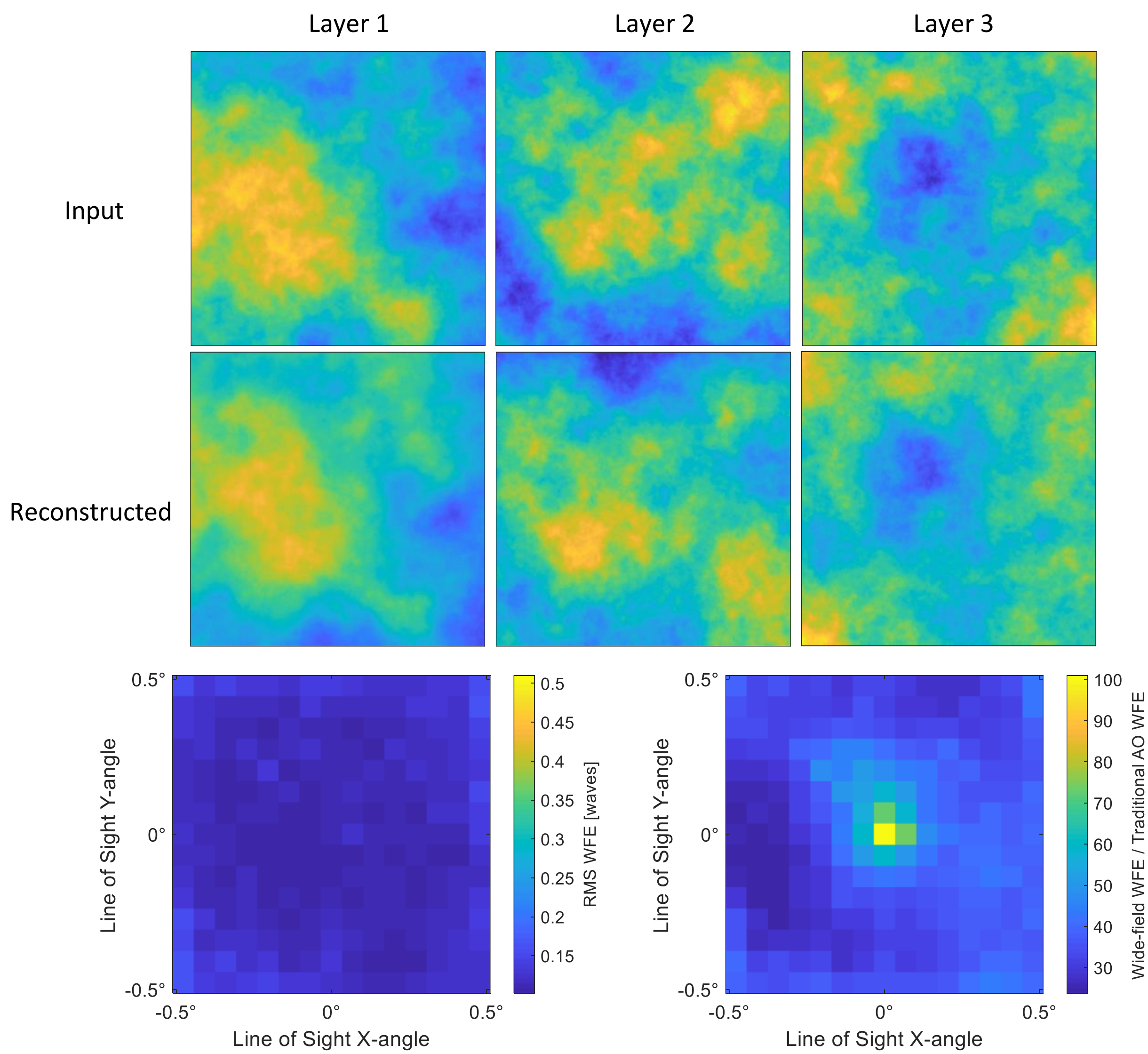

Figure 4.15: Input and reconstructed atmosphere with all layers present and perfect range knowledge.

diffraction limit across the full field of view. This serves as the baseline against which each of the three missing layer cases are to be compared. Some layer crosstalk is observed in the reconstructed layers, but all the quality metrics demonstrate acceptable performance.

The first layer removed is the isoplanatic layer as shown in Figure 4.16. The loss of the isoplanatic layer is well compensated by the two anisoplanatic layers as seen in the diffraction limited reconstruction across most of the field of view. There is an obvious attempt at compensation seen in the reconstruction of Layer 2. Comparing this reconstruction to classical AO

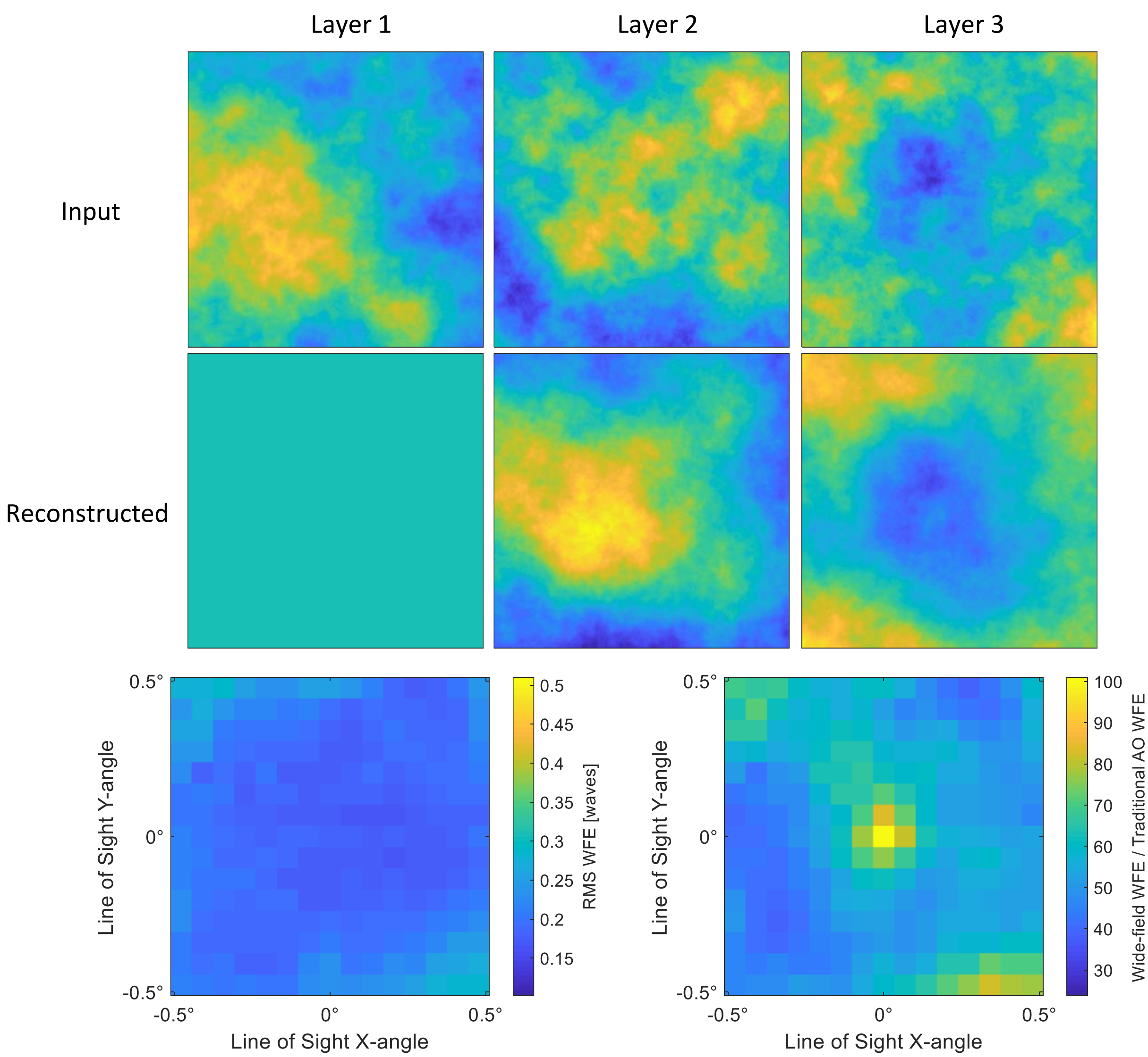

Figure 4.16: Input and reconstructed atmosphere along with quality metrics for a case where the isoplanatic layer was not detected.

still shows less than 40% of the wavefront error for some lines of sight and the RMS wavefront error is relatively flat across the field of view. While the reconstruction is relatively good in spite of the missing layer, this case is still roughly a factor of 2 times worse in terms of wavefront error than the nominal case. With additional aberrations introduced through things like ranging errors or noise in the slope vector computation, the reconstruction would go beyond the diffraction limit which may be unacceptable in some applications.

Looking at the removal of anisoplanatic layers yields slightly worse results than the previous case. Figure 4.17 shows the case where the anisoplanatic layer nearest the entrance pupil is not detector by the CLEAN algorithm. These results are on par with those shown in Figure 4.16 although the comparison to classical AO shows slightly worse results. Again, the two reconstructed layers do an admirable job compensating for the lost layer. More interesting is the case where the most distant layer is removed as shown in Figure 4.18. While removal of the first two layers yielded similar results to one another, the results from removal of the most distant layer are roughly 50% worse on average across the field of view. The two remaining layers are clearly attempting to compensate for the lost layer but cannot do as good of a job as the compensating layers in the previous two cases. This implies that more distant layers can compensate for missed turbulence closer to the entrance pupil, but that layer reconstructions nearer the telescope cannot compensate as well for distant layers. Even the comparison between the wide-field and central lines of sight shows relatively little improvement. With this knowledge, there may be a motivation to adjust the CLEAN algorithm further in future experiments to be more sensitive to distant layers.

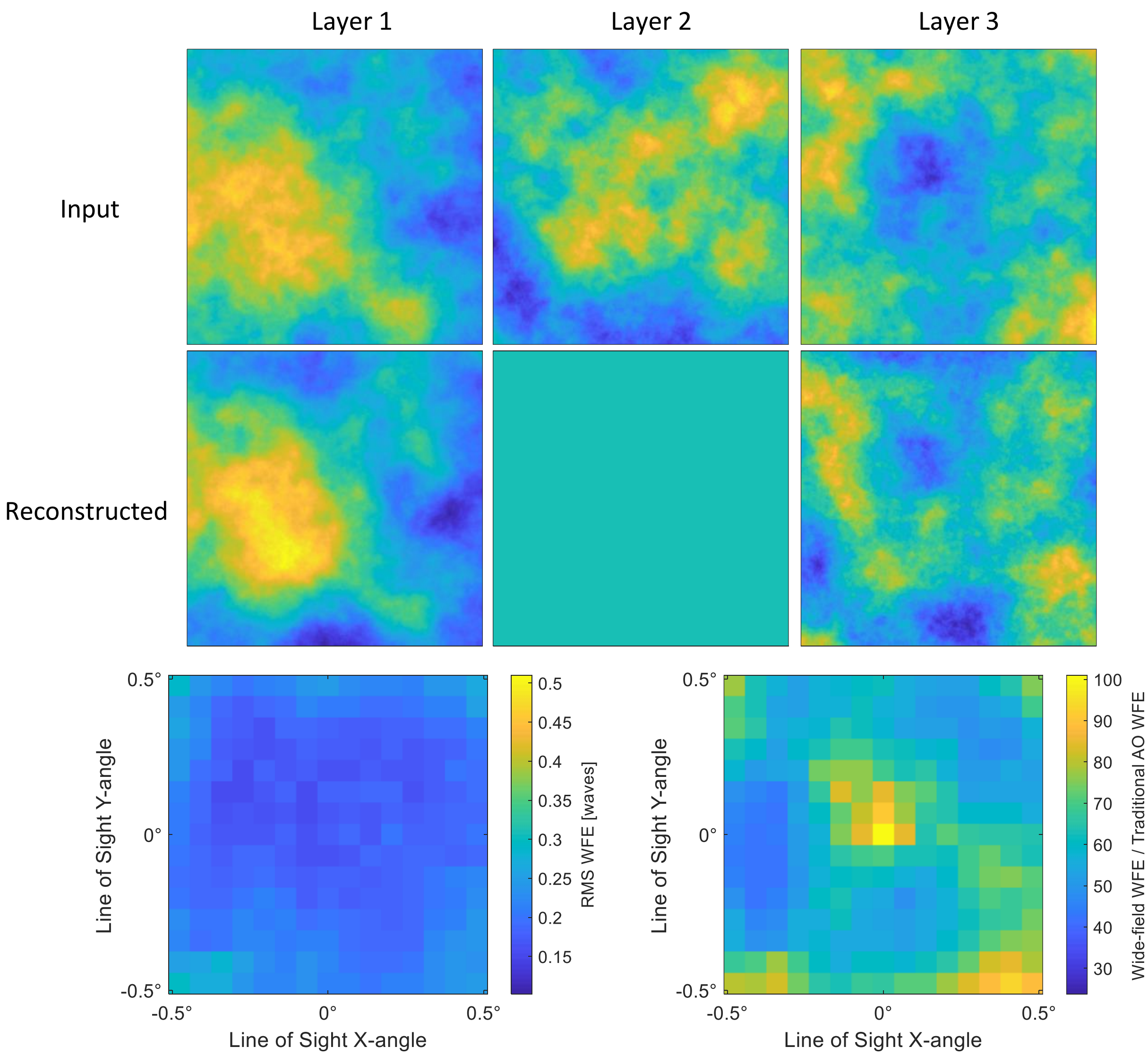

Figure 4.17: Input and reconstructed atmosphere along with quality metrics for a case where the anisoplanatic layer nearest the telescope was not detected.

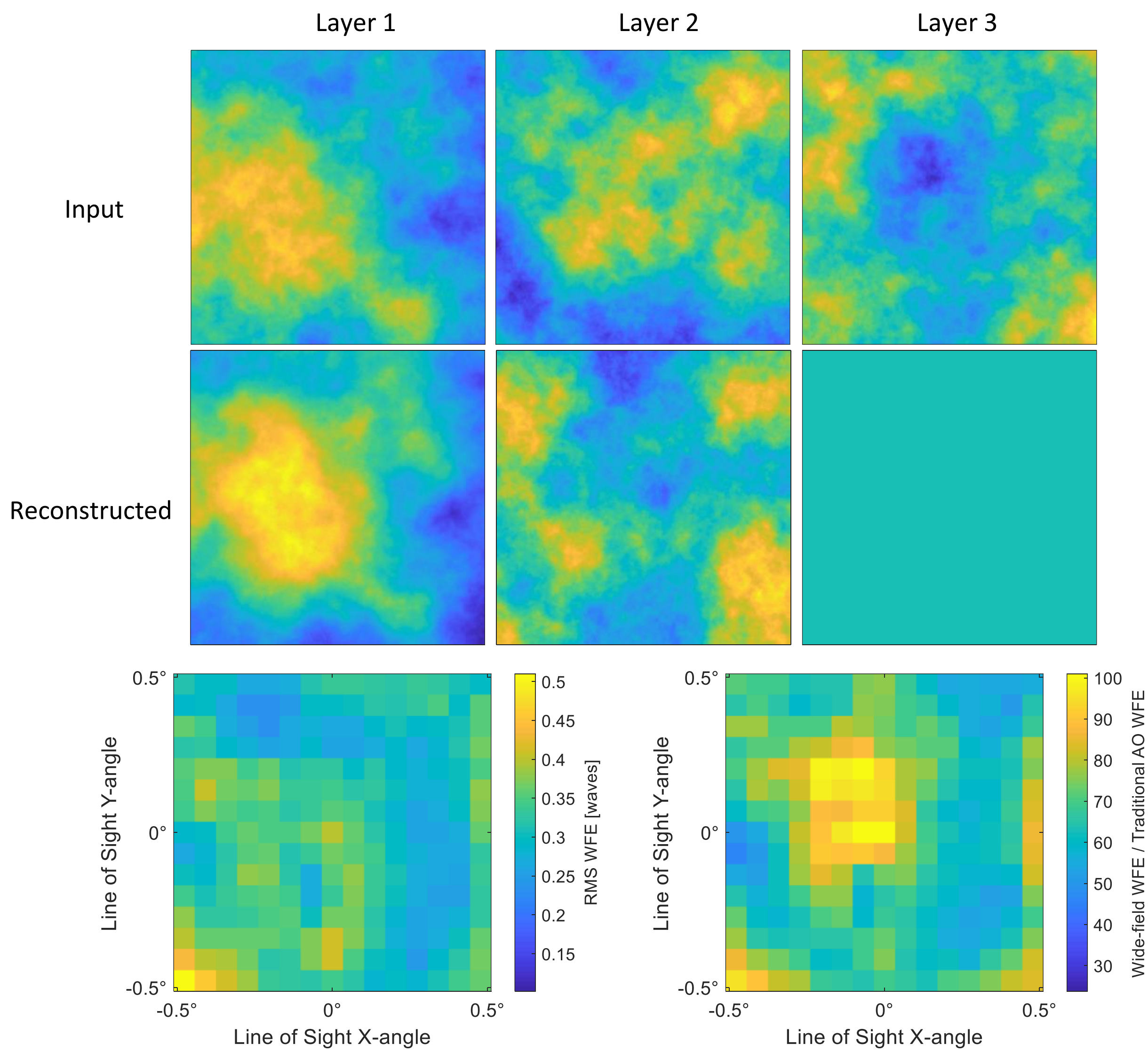

Figure 4.18: Input and reconstructed atmosphere along with quality metrics for a case where the furthest anisoplanatic layer was not detected.

Finally, the results of a missing anisoplanatic layer for a two-layer atmosphere is studied by virtue of examining Case #5. In this instance, a large spike in the correlation data set an inappropriate threshold on what can be identified as a turbulence layer and only an isoplanatic layer was identified. The single reconstructed screen is shown in Figure 4.7 and the wide field quality metrics are given in Figure 4.19. It is obvious from the left-hand image in Figure 4.19 that the reconstruction along any line of sight is never better than the diffraction limit. Since the layer is reconstructed at the telescope pupil, the comparison of wide-field reconstruction to a

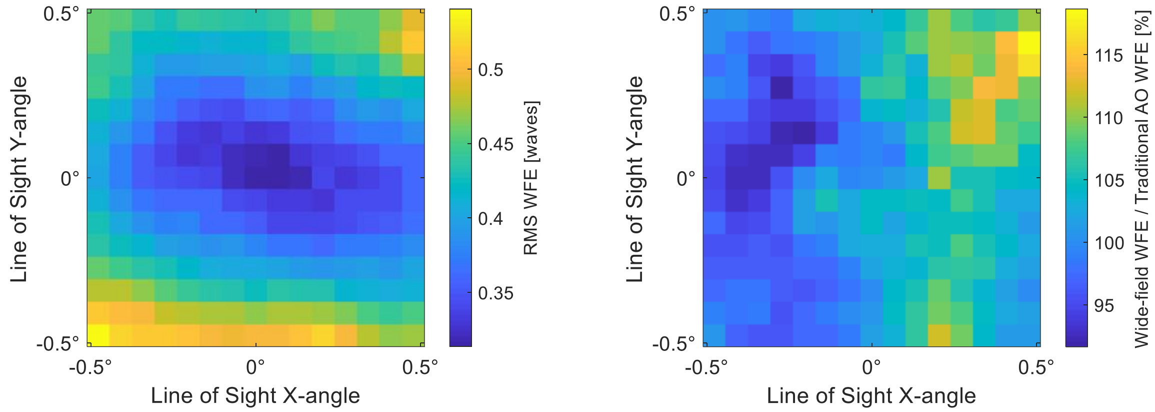

Figure 4.19: Residual wavefront error and wide-field correction improvement for Case #5.

reconstruction along the center line of sight shown in the right-hand image in Figure 4.19 shows no improvement. The wavefront error from the uncorrected atmosphere along each line of sight is shown in Figure 4.20 alongside the percent reduction in rms WFE that is achieved for each line of sight despite the missing layer in the atmospheric reconstruction. This reconstruction of the isoplanatic layer only is nearly identical to GLAO and the overall improvement is much more modest than other cases, but not insignificant. These results support the observations from the three-layered atmosphere that layers nearer the telescope have extreme difficulty in reproducing the effects induced by more distant layers.

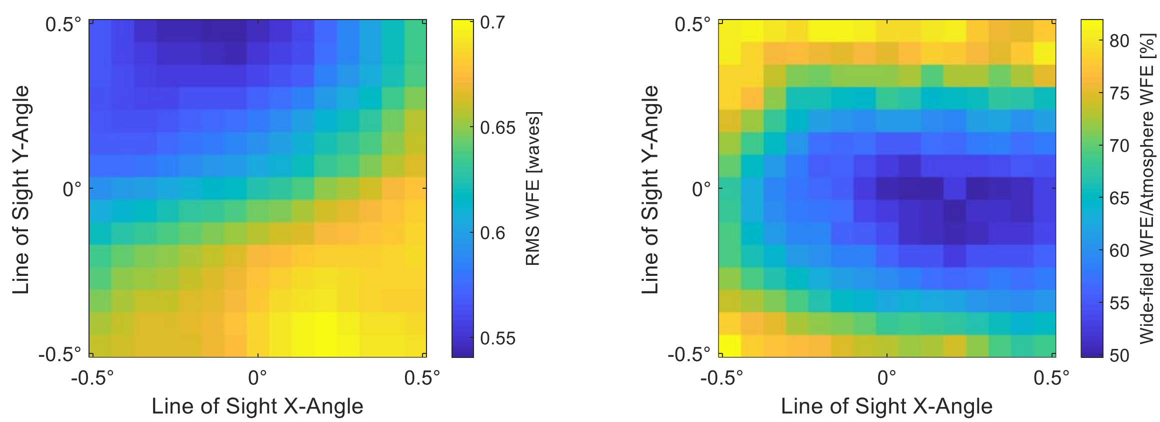

Figure 4.20: RMS wavefront error along all lines of sight for Simulated Atmosphere 1 (left) and the percentage reduction in RMS WFE over an uncorrected atmosphere (right).

4.5.2 Effects of Ranging Errors

One of the primary errors that can occur in atmospheric measurement and reconstruction is an error in layer ranging. The CLEAN algorithm typically provides estimates within 10% of the layer range, but things like unsampled ranges, adjacent layers, and large noise spikes can cause errors in the ranging results. To assess the impact of ranging error in reconstruction, a response matrix is generated for some range h. A fixed phase layer is then generated at a range of $h + \Delta h$ and the slope vector is computed. The response matrix is converted into a reconstruction matrix and the layer is reconstructed with a ranging error of Δh. The RMS wavefront error between the reconstructed layer at a range of h and the known input at a range of $h + \Delta h$ is analyzed along all lines of sight. The RMS wavefront error is averaged across the 225 lines of sight and this value is recorded as the ranging error, $\epsilon(\Delta h)$, as in the equation

$$\epsilon(\Delta h) = \frac{1}{N_{\theta_x,\theta_y}} \sum_{\theta_x,\theta_y} RMS\left(\phi_{reconstruced}(\theta_x, \theta_y, h) - \phi_{input}(\theta_x, \theta_y, h + \Delta h)\right). \qquad 4.3$$

Equation 4.3 is repeated for several values of Δh and a plot of change in wavefront error as a function of the error in reconstruction range is generated. Figure 4.21 shows this analysis for a single phase screen analyzed at input ranges of 152 mm, 312 mm, 627 mm, and 1053 mm. The results for the screen placed at 627 mm and 1053 mm are in reasonable agreement with one another and the layer at 312 mm is also in family with slightly lower wavefront error results. The results for the reconstruction at 152 mm show that there is some range dependence in the relative error with a reduction in impact closer to the telescope entrance pupil. For layers within 300 mm of the benchtop system, range errors of 10% produce less than a 20% increase in RMS wavefront error across the FOV.

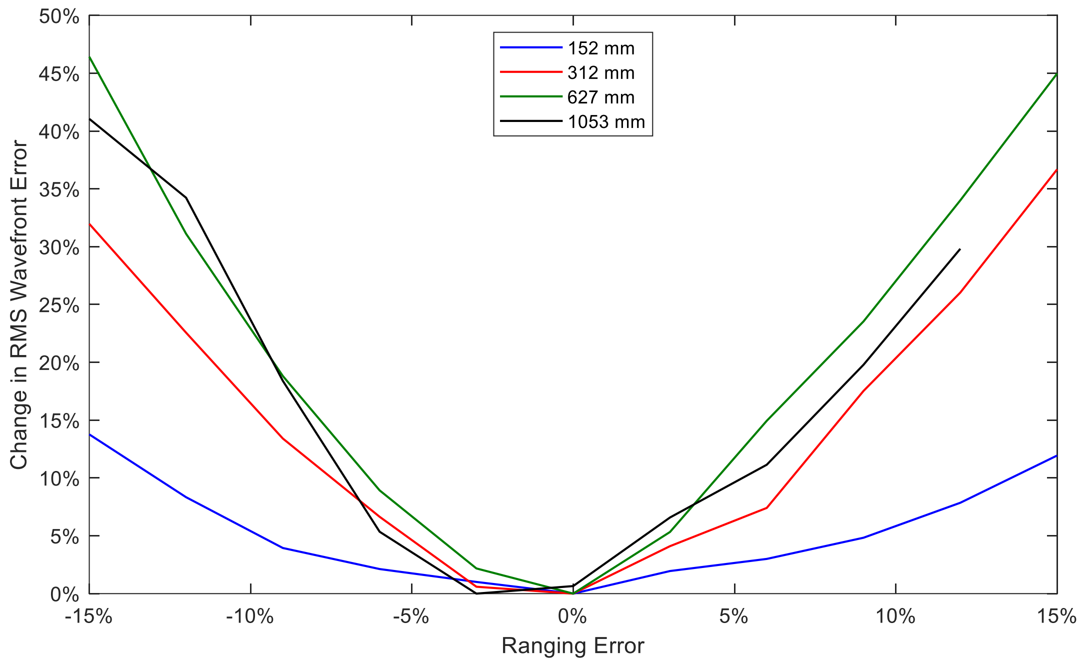

Figure 4.21: Change in mean RMS wavefront error as a function of layer ranging error seen at three different ranges. Each range uses the same phase screen for consistency.

In addition to the single-layer reconstruction, layer ranging errors were studied in a two-layer atmosphere. The 627 mm ranging case was repeated with a second layer inserted at the telescope entrance pupil to understand the effects of ranging errors when a second layer is present. The results are plotted in Figure 4.22 where the single layer is shown as a dashed line and the two-layer atmosphere is plotted as a solid line. All values are plotted as error relative to the single-layer case at a perfectly known range. The addition of a second layer increases the RMS wavefront error for the perfectly known case by approximately 1.5 or approximately $\sqrt{2}$. Despite this increase in the wavefront error the ranging error effects grow at approximately half the rate of the single-layer atmosphere. This reduction occurs because the same residual wavefront error from the isoplanatic screen is present in all measurements leading to a smaller increase for the same relative error in range for the distant layer. Examining the three-layered atmosphere from the missing layer

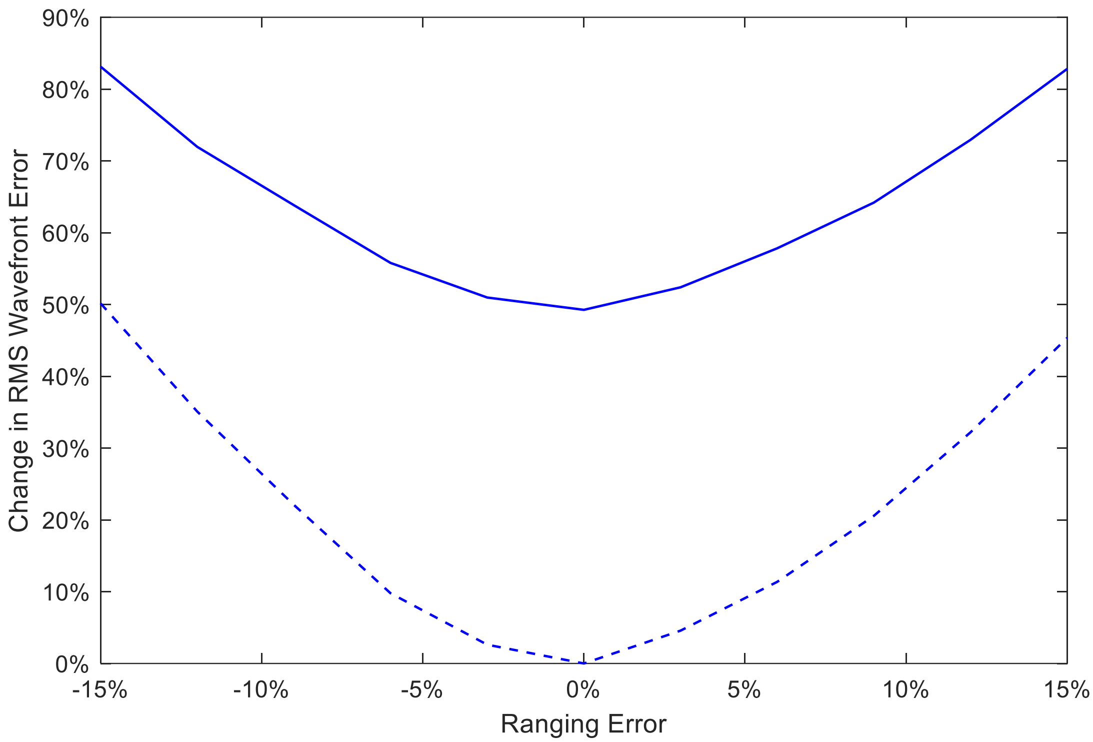

Figure 4.22: Change in mean RMS wavefront error as a function of layer ranging error for a two-layer atmosphere (solid line) and a single-layer atmosphere (dashed line). Both atmospheres contain an identical layer at 627 mm with an additional layer at the telescope entrance pupil in the two-layer atmosphere.

investigation shows an increase in the baseline wavefront error for the perfectly known case by a factor of 1.8 which is approximately $\sqrt{3}$. This implies that the errors from a many-layered atmosphere where layer strengths are evenly distributed will increase as the root-sum-squared (RSS) of the single layer case. This means that the overall WFE will increase as $\sqrt{N_{layers}}$, but the relative effects of ranging errors for a single given layer are expected to decrease by a factor of N.

4.5.3 Effects of Increased FOV

The final effect that was analyzed to understand the WFS operation and design is that of altering the FOV compared to the isoplanatic patch size. This change can either occur from an increase in the designed field of view or from a change in the turbulence strength of distant phase layers. The simulation was used to probe this effect using both a single distant layer and a two-layer atmosphere. In both cases the parameter θ_0 is decreased by increasing the amplitude of phase screens in the atmosphere and comparing wavefront error across the field of view.

To assess the theoretical performance of the system for the single-layer atmosphere at increased values of FOV/θ_0, the simulation is used to model a single phase screen 271.8 mm from the telescope entrance pupil. The phase screen used in this analysis was the anisoplanatic layer from the measured atmosphere. A warp map for this layer is generated along with a response and reconstruction matrix assuming perfect knowledge of the distance between the layer and the telescope entrance pupil. Wavefront error is measured along all lines of sight and then radially averaged around the central line of sight to produce a one-dimensional plot of RMS wavefront error as a function of angle from the instrument boresight. Figure 4.23 shows the resulting plot for several values of FOV/θ_0. Note that the single phase screen reconstructed much more accurately than the two-layered atmosphere and so has a lower wavefront error for an equivalent FOV/θ_0. For this simulated case, the diffraction limit is reached in the corners of the field of view at roughly FOV/θ_0 = 35.

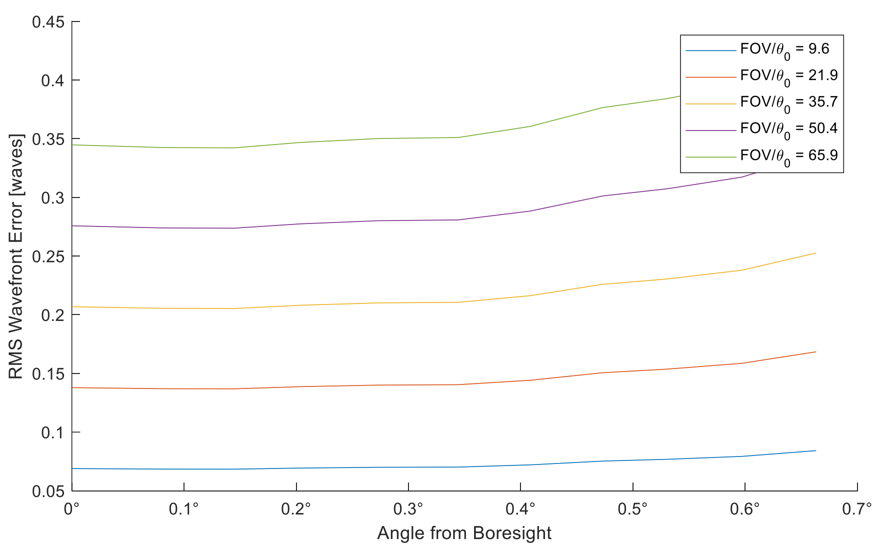

Figure 4.23: RMS wavefront error as a function of field of view for a single anisoplanatic phase screen. Layer 2 from the measured atmosphere was used to generate the data shown. The plot shows results for several values of FOV/θ_0.

Since the results of a single-layer atmosphere were significantly different than the two-layer atmospheres discussed in previous sections, the analysis is repeated using the measured phase plates inserted at 16.1 mm and 271.8 mm as in previous simulations. It is once more assumed that the simulation knows perfectly where these layers are for computation of a response and reconstruction matrix. Figure 4.24 shows the results for this second case. With the two-layer atmosphere, the baseline results show an increase in wavefront error of 60% for the same FOV/θ_0 and the diffraction limit is reached around FOV/θ_0 = 22.

The changes observed in Figure 4.23 and Figure 4.24 due to an increase in phase amplitude can also be explained through analytical methods. Equation 3.3 and Equation 3.4 show that when multiplying the phase screen by some scalar, A, the Fried parameter, and thus the isoplanatic patch, scale as $A^{-6/5}$ and the RMS wavefront error scales linearly as A. Thus, beginning with FOV/θ_0 = 9.6 and scaling the amplitude of the phase screen by a factor of 2, the wavefront error will double as seen with the blue and orange lines in Figure 4.23 and the blue and yellow lines in Figure 4.24. The FOV/θ_0 scales by $\frac{1}{2^{-6/5}} = 2.30$ so the FOV/θ_0 goes from 9.6 to 22 as also seen in Figure 4.23

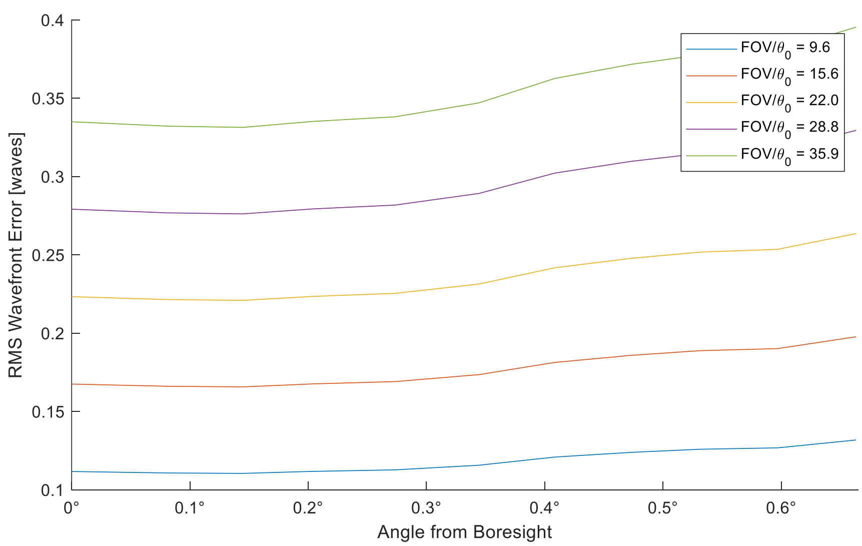

Figure 4.24: RMS wavefront error as a function of field of view for the atmosphere using measured phase screens. The plot shows results for several values of FOV/θ_0.

and Figure 4.24. With this information, one can predict the change in performance from a change in either the system FOV or the atmospheric isoplanatic patch, θ_0.

While the error is seen to get worse with the turbulence strength, the system was designed to accommodate a FOV/θ_0 of 15. Increasing the number of object points investigated through a stronger atmosphere will allow a better reconstruction of these more turbulent cases. Since the system is software based, the number of field points can be altered at any point in time in response to the changing atmosphere. This simply necessitates comparing larger patches of the scene for weaker turbulence and viewing warping on smaller portions of the scene for stronger turbulence. Such dynamic measurement and reconstruction is beyond the scope of this project, but is theoretically possible.

4.6 Scalability

All the analysis in this document relates to a simulation scaled to a benchtop demonstration, but real-world applications will occur on much larger scales. The results developed through this text remain applicable with some simple scaling of various parameters. As an example of this scaling process, a 50 cm telescope viewing an atmosphere analogous to the one developed using measured phase plates is examined with a scaling of the simulation into this new regime. Expanding the 11.25 mm simulated telescope aperture to a 50 cm diameter primary mirror requires a magnification of m = 44.4. The atmospheric parameters relative to the telescope are also assumed to remain constant with FOV/θ_0 = 9.5 and D/r_0 = 10.3. This means the atmospheric r_0 has a value of 4.9 cm at 633 nm which is in the bounds of what is typically considered poor seeing for modern telescopes. The FOV of the simulation is extremely ambitious for a wide-field AO system and was designed to pair well with the isoplanatic patch size, θ_0. A more realistic example would be to assume imaging over a full field of view of 1 arcminute which is on par with a typical MCAO system, but relatively small for MOAO systems. The isoplanatic angle then becomes 6 arcseconds which is slightly larger than what may observed in astronomical observations (Welsh & Gardner 1991, Neyman 2004). This implies that the turbulence is more biased towards the telescope pupil than often seen at astronomic observing sights. The scaled atmosphere includes an isoplanatic layer with the Fried parameter scaled to r_0 = 7.6 cm and an anisoplanatic layer with a scaled Fried parameter of r_0 = 7.1 cm. The range to the layers is scaled by the longitudinal magnification, $\bar{m}$, where $\bar{m} = m^2$ yielding layer ranges of 32 m and 537 m.

While this spacing is suitable for benchtop constructions, the anisoplanatic layer is nearer to the entrance pupil than would typically be achieved in a realistic application. Figure 4.24 shows that diffraction limited reconstruction can occur for a decrease in θ_0 to approximately 0.45 arc minutes which corresponds to an anisoplanatic layer range of 1.38 km for the same phase screen. Reduction in turbulence strength of the distant layer while increasing the layer range will maintain the same FOV/θ_0, but will reduce the overall D/r_0. As shown in the investigation of missing layers, ranges beyond 1000 mm can be faithfully reconstructed without any system level changes. A careful balancing of this tradeoff can bring the simulation into the realm of possible scenarios with layer ranges thousands of meters distant from the telescope pupil and the overall Fried parameter moving towards the realm of good seeing ($D/r_0 \approx 10 - 20$).

A final note on the scalability relates to the scalability of the atmosphere. Correcting the atmosphere by identifying and compensating for key layers of turbulence mimics the operation of an MCAO system. One of the limitations for MCAO is that the system needs to correct a number of layers equal to $\frac{1}{2}(FOV/\theta_0)$ for a continuous atmosphere (Beckers 1988). Because of this, larger fields of view or more turbulent atmospheres will require more computations to reconstruct and correct the observed atmosphere. More optimistic results were achieved in this simulation due to the input of a discretized atmosphere. One benefit of the WFS is that imaging an extended object allows for a large number of object points which enables tomographic reconstruction of a large number of turbulence layers.

4.7 Conclusions

The results of the various simulations performed have validated the proof of concept for the case of static turbulence. The atmosphere can be accurately measured and reconstructed by measurement along several lines of sight through a lenslet array. Metrics of performance are presented and show reconstruction of the simulated atmospheres within the diffraction limit. Performance is compared to a similar system that can only measure and reconstruct along a single line of sight with the wide-field reconstruction results demonstrating up to a factor of 3 improvement within the FOV. Viewing these results holistically demonstrates successful simulation of the wavefront sensor and validation of the proof of concept for a benchtop demonstration environment.

In addition to the successful demonstration of the WFS theory, common errors are investigated. Effects of turbulence layers that go unidentified are investigated and discussed with the finding that layers further from the telescope entrance pupil can accommodate unidentified turbulence closer to the pupil. Ranging errors are also investigated to demonstrate changes in performance for errors in peak identification when using the CLEAN algorithm. Finally, the effects from increasing the atmospheric turbulence strength are investigated to understand how the number of isoplanatic patches across the FOV alters the reconstruction for a fixed system design. The results can be equally applied to increasing the FOV through a fixed atmosphere.

The scalability of this demonstration to a larger system provided insight into where the simulation over-achieves and underachieves compared to a real-world atmosphere. While the atmospheres presented in this work may overestimate the atmospheric aberration, they also underestimate realistic ranges to distant layers. The atmospheric reconstructions demonstrated in this work still validate the proof of concept that the method can be used to measure and reconstruct a multi-layer atmosphere. There is nothing prohibiting the measurement and reconstruction of more distant layers so long as the system design is altered to accommodate the required ranges. Further updates to the system architecture can allow further improvement in measuring and reconstructing ranges more appropriate for a system with real world applications. In summary, this work has shown that the proposed wavefront sensor can examine a static atmosphere, understand the underlying discrete turbulence layers, and develop a reconstruction for an arbitrary number of layers presented at arbitrary ranges which fall within the capabilities of the system.

Chapter 5: Future Work and Applications

Adaptive optics has changed the way that ground-based telescopes view our universe. Up to this point, AO has mostly been used in astronomical applications, but as the technology continues to mature the application range will continue to widen. AO has already grown to include laser communications (Tyson 2002), solar imaging (Von der Lühe 1987), and ophthalmology (Liang & Williams 1997). The theory and methods developed in this work have unique applications that can open new possibilities in wide field imaging once the technology reaches sufficient maturity. The simulation presented in this work is developed as a proof that the methodology is sound, but this is simply the first step towards a working technology demonstrator.

This work has expounded on the current environment in the AO community and provided the context for this technology. The theory and methodology are laid out and the software implementation is fully explained. The results show successful wide-field reconstruction of an atmosphere comprised of discrete phase screens with varying layer ranges and layer numbers. Despite these accomplishments, there is still much to be done before the technology can be demonstrated in a physical system with real-time dynamic functionality. Section 5.1 discusses advancements in the simulation which are needed to demonstrate full end-to-end performance. Additional advancements related to the algorithms are proposed in Section 5.2. While a hardware system was developed in conjunction with the simulation, Section 5.3 addresses the benchtop improvements necessary to develop a complete benchtop demonstration unit. Finally, a variety of applications are proposed in Section 5.4.

5.1 Simulation Advancements

The current simulation allows demonstration of the theoretical performance of a WISH WFS in the static case up to the point that the atmosphere is reconstructed. While this provides proof that the methodology is sound, there are still several advancements that can be made to the software demonstration. These advancements include:

1. Modeling of an extended scene
2. Modeling of dynamic effects
3. Field-dependent PSF deconvolution

Each of these advancements will increase the accuracy of the simulation and bring the performance estimates one step closer to those of a realistic system. Additional improvements beyond these three items include addition of noise into the system, investigation of motion blur due to non-zero exposure times, and atmospheric modeling with more layers of varying strengths for a better representation of a continuous medium. These simulation upgrades prior to buildup of a demonstration unit would allow comparison of the actual performance with the theoretical performance and allow a method for system level pathfinding of errors and pitfalls.

5.1.1 Modeling of an Extended Scene

The current simulation measures the atmosphere by analyzing the gradient of the accumulated phase along a given line of sight. This is analogous to the WFS viewing a grid of infinitely distant point sources and measuring PSF displacements. As described in Chapter 2: and Chapter 3:, the system is designed around the concept of measuring local warping of objects viewed in an extended scene. Altering the simulation to generate extended scenes warped by atmospheric turbulence would enable further development of the slope measurement algorithms discussed in Section 2.2.2 with variety of input scenes. This could be used to understand optimum spatial frequency content and difficulties introduced through the image processing beyond what is explored in this work. The modeling of the extended scene will also be necessary to explore the deconvolution performance as discussed in Section 5.1.3.

5.1.2 Modeling of Dynamic Effects

The static demonstration yields extremely encouraging results for atmospheric measurement and reconstruction which will only be improved with the inclusion of dynamic effects. Motion of the atmosphere is easily achieved by creating an oversized representation of each layer. A wind velocity is then assigned to the layers and the phase screen is shifted according to this velocity between atmospheric measurements. This matches the assumptions in Taylor's frozen flow hypothesis as outlined in Section 1.1 and Section 2.3.2 (Taylor 1938). These dynamic effects in the atmosphere enable an alternate version of SLODAR which looks at correlations across different exposures to estimate the velocity of input layers. This analysis also provides a second estimate of the layer ranges which will improve range estimates and increase the likelihood that all input layers will be identified (Wang et. al. 2008).

The other simulation improvement possible through the inclusion of dynamic turbulence is the resolution increase possible through frozen flow modeling. This method, described in Section 2.3.3, uses past reconstructions of the phase screens along with the frozen flow hypothesis to interpolate the phase aberration on scales smaller than the WFS would typically allow. This has been modeled in prior experiments (Jefferies & Hart, 2011) and the modeling can be implemented with simulations of the WISH WFS to increase the quality of the reconstructed field dependent PSFs. Once the wind vectors are applied to the phase screens and multiple sequential frames of data are taken, the frozen flow modeling can be implemented to improve the simulation results.

5.1.3 Field-dependent PSF Deconvolution

Section 4.4.2 shows that the reconstructed aberration along a given line of sight matches the input phase screen with an RMS wavefront error less than 0.25 waves. Using this reconstructed line of sight phase aberration, a PSF is generated which can be deconvolved from the scene using a Wiener filter as described in Section 2.5.2. The use of a Wiener filter allows the deconvolution to take place over the portion of the scene which corresponds to the specific line of sight. Implementation of this deconvolution method will yield insight into how faithfully the scene can be reconstructed and what filter width values yield the best results. Implementation of this final step in the simulation, along with the addition of the scene modeling and dynamic turbulence, would truly allow an end-to-end model of the WFS from scene generation to scene correction.

5.2 Algorithm Development

In addition to simulation upgrades, there are algorithms that need to be developed and improved. The straightforward development efforts include the development of algorithms to support the simulation improvements mentioned in Section 5.1 including the algorithms to support dynamic measurements and PSF deconvolution. In addition to new functionality, there are improvements on the existing algorithms that can be developed and implemented to improve speed and performance. The two algorithms that can benefit the most from additional development are the CLEAN algorithm variation and the SLODAR data processing.

5.2.1 CLEAN Improvements

The CLEAN algorithm is one area that could use a deeper level of optimization and development. The current implementation suffices for the current needs, but improvements can be made to improve the ability to identify layers and reject spurious correlations. The thresholding is one such area where improvements in the algorithm will impact the ability to accurately reconstruct the atmosphere. Not only are there opportunities to improve the current thresholds but new thresholds can be invented to improve layer identification and noise rejection. A final proposed improvement relates to the determination of peak location. Increasing the accuracy of the layer ranging will increase the accuracy of layer reconstruction as discussed in Section 4.5.2.

Thresholding in the CLEAN algorithm is implemented to reduce the likelihood of spurious peaks in the SLODAR data being identified as input layers. The two thresholds set in the processing thus far are a limitation on peak height and a limitation on Lorentzian width. The peak height threshold is implemented to create a stopping point in the algorithm. Once there are no data points above some percentage of the maximum value, the algorithm can stop searching for additional peaks. With the current definition, layers with relatively small amplitudes in the SLODAR results may not be identified as is seen in Case #5. A more elegant mechanism would reduce the possibility of missing correlation peaks which correspond to input layers. This could be a comparison of the remaining peak values to one another, to a standard deviation, or to the previously identified peaks. Similarly, the width threshold was implemented to reduce spurious layers being identified as significant. Given the plethora of additional layers identified in Table 4.2, the current thresholds have significant room for improvement. This becomes challenging as the threshold needs to be loose enough to not reject any odd-shaped correlations that pertain to actual layers.

In addition to the current thresholds, other methods can be investigated and implemented to reduce the number of spurious layers. One such method may be to compare the profiles generated using small and large boxcar widths and identify the layers that have dropped out as spurious. A second method to identify spurious layers could be a check on the values of nearby datapoints to determine if the peak is generally smooth. The implementation of this second method may be limited to regions where there is a good sampling of the atmosphere as more distant layers may suffer from the hardware's ability to probe a continuous region. Additional thresholds beyond the two proposed here may become apparent with further development.

The final improvement to the algorithm lies in the range finding ability. The current implementation finds a peak and fits a curve to datapoints near that peak value. Because the profile is generally noisy, the maximum value of the dataset may not correspond to the peak of the Lorentzian fit. Because of this, an iterative fitting approach may provide better results where a second fit is performed with the dataset re-centered on the peak of the initial fit. Additionally, smoothing the profile near the peak with a low-pass filter prior to fitting may provide a better functional fit. Finally, the Lorentzian provides a good empirical fit near the peak of an input layer, but there may be a functional form that provides better results. A broader investigation of functional forms may be able to find a better fit to the data and provide a more robust method of peak determination.

5.2.2 SLODAR Improvements

The current implementation of the SLODAR algorithm compares each data point from the measured atmosphere with every other datapoint. This is very thorough, but ultimately very inefficient. The full two-dimensional cross-correlation is collected for each pair of field points, but the data is immediately reduced by taking a one-dimensional slice and collecting data only along the direction of the object separation as outlined in Section 3.5.3. This slice yields n_{lens} data points from an array containing $(2n_{lens} - 1)^2$ values. As an example, the 361 values represented in Figure 3.24 yield 10 datapoints that are input into the SLODAR profile. The inefficiency is the same for the cross-correlations computed for every pair of field points. This example case yields less than a 3% efficiency in the amount of data used versus the amount of data generated. Each of the discarded values in each cross-correlation represent numerous multiplication and addition operations that go to waste. Reduction in the data processing by reducing the full cross-correlation to operate along a single direction will save many computations and improve the algorithm efficiency. This will become more and more significant with increases in the field of view, in the atmospheric turbulence strength, and in the number of lenslets imaging the scene. Because the SLODAR algorithm can operate on every frame, this computational savings will be essential as the simulation and the hardware enter the realm of real-time processing.

5.3 Hardware Implementation

A hardware implementation was built in parallel with the simulation effort, but there are several advances that can be implemented for the final proof of concept system. One challenge was the optical thickness of the phase plates. Insertion of these thick plates caused an error in conjugation of the DM to the phase layers and a focus error at the focal planes. Accounting for these ranging errors during the system alignment is important in the successful implementation of the system.

The second major improvement would be to develop a more realistic atmosphere. The initial goal was to achieve an atmosphere with D/r_0 and FOV/θ_0 of approximately 10-15 and this is accomplished in the current design. Scaling this to a realistic atmosphere as outlined in Section 4.6 showed that the atmospheric seeing was generally poor, though not unrealistic. On the other hand, the isoplanatic patch was much larger than is typical in astronomical observations. Applications on more finite scales will have a broader distribution of turbulence at ranges closer to the entrance pupil, but realistically, a smaller isoplanatic patch would be expected. Depending on the focal plane used for imaging, this decrease in isoplanatic patch may need to be coupled with a decrease in the field of view. This will allow the system to maintain a similar FOV/θ_0 and a similar number of patches across the scene. This is important as there need to be enough pixels in each patch for meaningful cross-correlations to take place.

An additional improvement relates to the signal generated by the scene generator and recorded by the WFS. The hardware as initially designed allows enough throughput that the scene can be captured on the WFS and science cameras using exposure times of several seconds. Improving the system throughput will increase the contrast of the scene and enable faster data collects. This will become more important as the hardware is used to mimic real-time data collects in dynamic turbulence. Alternatively, a more radiant source could be used to generate the scene. The iPad Mini 2 was turned to the brightest settings, but the pixels radiate light in all directions and the light output is limited to what the screen can achieve. A transparency back illuminated by a laser or lamp would be able to achieve much higher light output and would result in better signal at the focal plane. Increasing the throughput and increasing the source radiance are both equally viable but either one will require a careful redesign of the benchtop system to optimize the optical path.

Finally, there is room for improvement in the size of the generated scene. The current design has a magnification of 2.54 as described in Section 3.1.1.3. With a 3.75 mm square detector area, the scene is only prescribed to be 9.5 mm square, or 122 pixels. This very much under-utilizes the 1536×2048 pixel screen of the iPad Mini 2. With no turbulence present, the WFS cameras were able to resolve the iPad pixels and resolution was thus limited by the generated scene. A solution with either finer pixel pitch or a larger magnification will allow smaller spatial frequencies to be represented in the scene and provide an overall better match between the generated scene and the rest of the system hardware.

5.4 Potential Applications

The WISH wavefront sensor has been developed to suit any application where an extended scene is imaged through a turbulent medium. As an example, the WISH WFS can be deployed on a high-altitude aircraft to remove warping of objects on the Earth's surface due to the aero-optic layer in addition to the various atmospheric layers. Terrestrial imaging can also include ground-to-ground imaging where a telescope is viewing a distant object and the turbulence is disturbed more evenly across the intermediate distance. Astronomic applications can also be benefitted in solar and lunar imaging along with observation of low-orbit satellites around the Earth. The primary benefits of the system are its ability to respond to a changing atmospheric composition and its low size, weight, and power consumption. The application space for this WFS is limited only by the ability to resolve high spatial frequency information across an extended scene.

The ability to maintain flexibility in the face of changes to layer ranges or changes in the number of significant layers of turbulence allows this type of a system to operate in environments that were previously inaccessible to wide field adaptive optics. Multi-conjugate adaptive optics measures and applies a correction only at predetermined ranges and these systems are not flexible to large changes in atmospheric composition. Multi-object adaptive optics traditionally requires a large number of wavefront sensors and one or more DMs to properly implement. Ground layer adaptive optics removes only the isoplanatic layer and doesn't provide full correction to any particular line of sight. Because the WISH WFS identifies and reconstructs the isotropic layer, a hybrid GLAO/WISH system may prove useful where the isoplanatic aberration is removed via hardware and anisoplanatic layers are corrected as described in this text. Alternatively, combination of the WISH reconstruction and an MOAO based correction using a single DM can provide correction around a specific object of interest in real-time with additional software corrections over the remainder of the field of view. Environments where the atmospheric composition may change more rapidly include mounting of the telescope on a mobile platform or placement in regions with large changes in the seasonal weather patterns. The WISH WFS allows the flexibility, SWaP, and high level of correction not offered by typical AO solutions operating in a highly variable atmosphere.

References

Andersen, D. R., Jackson, K. J., Blain, C., Bradley, C., Correia, C., Ito, M., Lardière, O., & Véran, J. P. (2012). Performance Modeling for the RAVEN Multi-Object Adaptive Optics Demonstrator. *Publications of the Astronomical Society of the Pacific, 124*(915), 469–484. https://doi.org/10.1086/665924

Assemat, F., Hammer, F., Gendron, E., Sayede, F., Laporte, P., Marteaud, M., Puech, M., Conan, J.-M., Fusco, T., Liotard, A., & Zamkotskian, F. (2004) FALCON: a new-generation spectrograph with adaptive optics for the ESO VLT. *Proc. SPIE 5237, Optics in Atmospheric Propagation and Adaptive Systems VI.*

Bates, R. H. T., & McDonnell, M. J. (1986). *Image restoration and reconstruction*. Oxford University Press.

Beckers, J. M. (1988) Increasing the size of the isoplanatic patch with multiconjugate adaptive optics. *Proc. ESO Conf. on Very Large Telescopes and their Instrumentation (M.-H. Ulrich, ed.), 30*, 693—703.

Berkefeld, T., Soltau, D., & von der Luhe, O. (2003). Multiconjugate adaptive optics at the Vacuum Tower Telescope, Tenerife. *Adaptive Optical System Technologies II*. https://doi.org/10.1117/12.459799

Butterley, T., Wilson, R. W., & Sarazin, M. (2006). Determination of the profile of atmospheric optical turbulence strength from SLODAR data. *Monthly Notices of the Royal Astronomical Society*, *369*(2), 835–845. https://doi.org/10.1111/j.1365-2966.2006.10337.x

Chun, M., Wilson, R., Avila, R., Butterley, T., Aviles, J.-L., Wier, D., & Benigni, S. (2009). Mauna Kea ground-layer characterization campaign. *Monthly Notices of the Royal Astronomical Society*, *394*(3), 1121–1130. https://doi.org/10.1111/j.1365-2966.2008.14346.x

Dicke, R. H. (1975). Phase-contrast detection of telescope seeing errors and their correction. *Astrophys. J.*, *198*, 605—615.

Gendron, E., & Léna, P. (1996). Single layer atmospheric turbulence demonstrated by adaptive optics observations. *Astrophysics and Space Science*, *239*(2), 221–228. https://doi.org/10.1007/bf00645776

Greivenkamp, J. E. (2004). *Field guide to geometrical optics*. SPIE Press.

Foy, R., & Labeyrie, A. (1985). Feasibility of adaptive optics telescope with laser probe. *Astron. Astrophys., 152*, L29.

Fried, D. L. (1965). Statistics of a geometrical representation of wave-front distortion. *J. Opt. Soc. Am.*, *55*, 1427.

Fried, D. L. (1966). Optical resolution through a randomly inhomogeneous medium for very long and very short exposures. *J. Opt. Soc. Am.*, *56*(10), 1372-1379. https://doi.org/10.1364/josa.56.001372

Fried, D. L. (1977) Adaptive optics for imaging within the atmosphere: Reference generation and field-of-view widening. *Tech. Rep. TR-273, The Optical Sciences Company*.

Fried, D. L. (1982) Anisoplanatism in adaptive optics. *J. Opt. Soc. Am.*, *72*, 52.

Fried, D. L. (1990) Time-delay-induced mean-square error in adaptive optics. *J. Opt. Soc. Am. A*, *7*, 1224.

Hammer, F., Sayède, F., Gendron, E., Fusco, T., Burgarella, D., Cayatte, V., Conan, J. M., Courbin, F., Flores, H., Guinouard, I., Jocou, L., Lançon, A., Monnet, G., Mouhcine, M., Rigaud, F., Rouan, D., Rousset, G., Buat, V., & Zamkotsian, F. (2002). The FALCON Concept: Multi-Object Spectroscopy

Combined with MCAO in Near-IR. *Scientific Drivers for ESO Future VLT/VLTI Instrumentation*, 139–148. https://doi.org/10.1007/978-3-662-43215-0_21

Högbom, J. (1974). Aperture synthesis with a non-regular distribution of interferometer baselines. *Astrophys. J. Suppi. Ser., 15*, 417-426.

Jefferies, S. M., & Hart M. (2011). Deconvolution from wave front sensing using the frozen flow hypothesis, *Opt. Express 19*, 1975-1984

Kellerer, A. (2012) Layer-oriented adaptive optics for solar telescopes. *Appl. Opt., 51*(23), 5743–5751.

Kolmogorov, A.N. (1941a). Dissipation of energy under locally isotropic turbulence. *Dokl. Akad. Nauk SSSR 32*, 16–18.

Kolmogorov, A. N. (1941b). The local structure of turbulence in incompressible viscous fluid for very large Reynolds number. *Dokl. Akad. Nauk SSSR, 30*, 9–13.

Kornilov, V., Tokovinin, A. A., Vozyakova, O., Zaitsev, A., Shatsky, N., Potanin, S. F., & Sarazin, M. S. (2003). MASS: a monitor of the vertical turbulence distribution. *Adaptive Optical System Technologies II*. https://doi.org/10.1117/12.457982

Lane, R. G., Glindemann, A., & Dainty, J. C. (1992). Simulation of a Kolmogorov phase screen. *Waves in Random Media*, *2*(3), 209–224. https://doi.org/10.1088/0959-7174/2/3/003

Liang, J., & D. R. Williams. (1997) Aberrations and retinal image quality of the normal human eye. *J. Opt. Soc. Am. A, 14*, 2873.

McKechnie, T. S. (1991). Light propagation through the atmosphere and the properties of images formed by large ground-based telescopes. *J. Opt. Soc. Am. A*, *8*, 346—365.

Moore, E.H. (1920) On the reciprocal of the general algebraic matrix. *Bulletin of American Mathematical Society, 26*, 394-395.

Mugnier, L. M., Robert, C., Conan, J.-M., Michau, V., & Salem, S. (2001) Myopic deconvolution from wave front sensing. *J. Opt. Soc. Am. A*, *18*(4), 862–872.

Neyman, C. (2004) Keck Adaptive Optics Note #303, https://www2.keck.hawaii.edu/optics/kpao/files/KAON/KAON303.pdf

Noll, R. J. (1976). Zernike polynomials and atmospheric turbulence. *J. Opt. Soc. Am., 66*, 207.

Osborn, J. (2010). Profiling the turbulent atmosphere and novel correction techniques for imaging and photometry in astronomy. *PhD Thesis, Durham University*.

Penrose, R. (1955). A generalized inverse for matrices. *Mathematical Proceedings of the Cambridge Philosophical Society*, *51*(3), 406–413. https://doi.org/10.1017/s0305004100030401

Poyneer, L., Van Dam, M., & Véran, J.-P. (2009). Experimental verification of the frozen flow atmospheric turbulence assumption with use of astronomical adaptive optics telemetry. *J. Opt. Soc. Am. A, 26*, 833-846.

Primot, J., Rousset, G., & Fontanella, J. C. (1990) Deconvolution from wave front sensing: a new technique for compensating turbulence-degraded images. *J. Opt. Soc. Am. A, 7*(9), 1598–1608.

Ragazzoni, R., Marchetti, E., & Rigaut, F. (1999). Modal tomography for adaptive optics. *Astron. Astrophys., 342*, L53–L56.

Rigaut, F., & Gendron, E. (1992). Laser guide star in adaptive optics: the tilt determination problem. *Astronomy and Astrophysics*, *261*, 677-684.

Rigaut, F. J., Ellerbroek, B. L., & Flicker, R. (2000). Principles, limitations, and performance of multiconjugate adaptive optics. *Adaptive optical systems technology*. https://doi.org/10.1117/12.390311

Rigaut F. (2002). Ground-Conjugate Wide Field Adaptive Optics for the ELTs. *ESO Conf. and Workshop Proc., Beyond Conventional Adaptive Optics*, *58*, 11.

Roddier, F. (1981). The effects of atmospheric turbulence in optical astronomy. *Progress in Optics*, 281–376. https://doi.org/10.1016/s0079-6638(08)70204-x

Roddier, F. (1999). *Adaptive Optics in Astronomy* (1st ed.). Cambridge University Press.

Schöck, M., & Spillar, E. J. (1998) Measuring wind speeds and turbulence with a wavefront sensor. *Opt. Lett., 23*, 150-152.

St-Jacques D., (1998). Atmospheric seeing in space and time: A study of atmospheric turbulence in Spain and England, 1994-98. *PhD thesis, Univ. Cambridge*.

Taylor, G. I. (1938). The Spectrum of Turbulence. *Proceedings of the Royal Society A: Mathematical, Physical and Engineering Sciences, 164*(919), 476–490. https://doi.org/10.1098/rspa.1938.0032

Tikhonov, A., & Glasko, V. (1965). Use of the regularization method in non-linear problems. *USSR Computational Mathematics and Mathematical Physics, 5*(3), 93–107. https://doi.org/10.1016/0041-5553(65)90150-3

Tokovinin, A. (2004). Seeing improvement with ground-layer adaptive optics. *Publications of the Astronomical Society of the Pacific*, *116*(824), 941

Tyson, R. K. (2002). Bit error rate for free space adaptive optics laser communications. *J. Opt. Soc. Am. A*, *19*, 753.

Tyson, R. K., and Frazier, B. W. (2012). *Field guide to adaptive optics*. SPIE Press.

Tyson, R. K. (2015). *Principles of adaptive optics* (3rd ed.). CRC press.

Vernin, J., & Roddier, F. (1973). Experimental determination of two-dimensional spatiotemporal power spectra of stellar light scintillation: Evidence for a multilayer structure of the air turbulence in the upper troposphere. *J. Opt. Soc. Am.*, *63*, 270-273.

Von der Lühe, O. (1987). A wavefront sensor for extended, incoherent targets. *LEST Technical Report 28, Proc. Workshop on Adaptive Optics in Solar Observations*, 155.

Wang, L., Schöck, M., & Chanan, G. (2008). Atmospheric turbulence profiling with slodar using multiple adaptive optics wavefront sensors. *Appl. Opt.*, *47*, 1880-1892.

Welsh, B. M., & Gardner, C. S. (1991). Effects of turbulence-induced anisoplanatism on the imaging performance of adaptive-astronomical telescopes using laser guide stars. *J. Opt. Soc. Am. A, 8*, 69—80.

Welsh, B. M., & Roggemann, M. C. (1995) Signal-to-noise comparison of deconvolution from wave-front sensing with traditional linear and speckle image reconstruction. *Appl. Opt.*, *34*(12), 2111–2119.

Wilson, R. W. (2002). SLODAR: measuring optical turbulence altitude with a Shack-Hartmann wavefront sensor. *Monthly Notices of the Royal Astronomical Society, 337*(1), 103–108. https://doi.org/10.1046/j.1365-8711.2002.05847.x

Yahel, R. Z. (1990). Turbulence effects on high energy laser beam propagation in the atmosphere. *Appl. Opt. 29*, 3088.